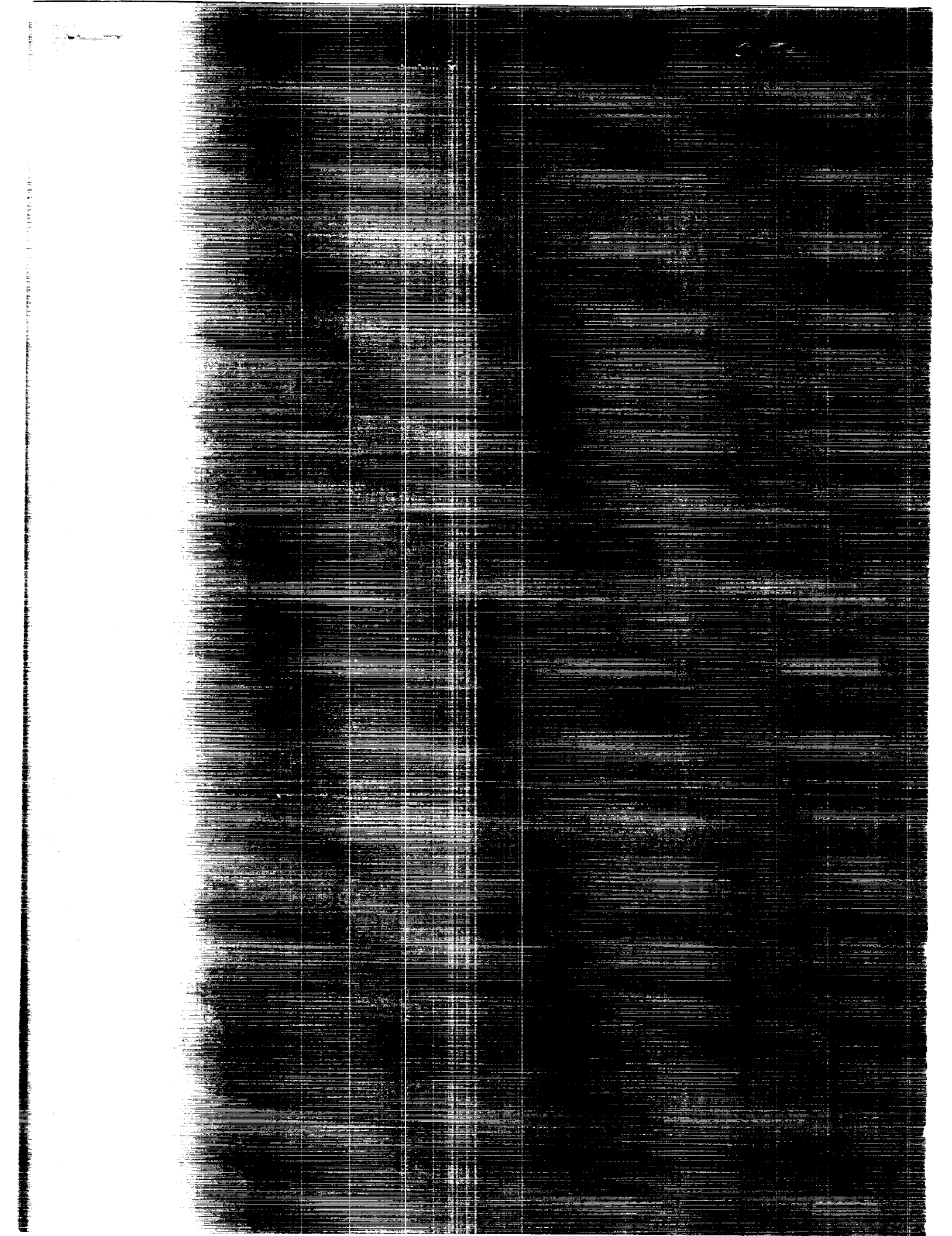


(NASA-CR-4280) SYNTHETIC APERTURE RADAR
IMAGERY OF AIRPORTS AND SURROUNDING AREAS:
PHILADELPHIA AIRPORT Final Report, 31 Aug.
1987 - 30 Nov. 1989 (ERIM) 108 p CSCL OIC

N70-10372

Unclas

H1/03 0204744



NASA Contractor Report 4280
DOT/FAA/DS-89/15

Synthetic Aperture Radar Imagery of Airports and Surrounding Areas

Philadelphia Airport

Robert G. Onstott and Denise J. Gineris
Environmental Research Institute of Michigan (ERIM)
Ann Arbor, Michigan

Prepared for
Langley Research Center
under Contract NAS1-18465

NASA

National Aeronautics and
Space Administration
Office of Management
Scientific and Technical
Information Division

1990



SYNTHETIC APERTURE RADAR IMAGERY
OF
AIRPORTS AND SURROUNDING AREAS
PHILADELPHIA AIRPORT

FOREWORD

This is the final report for Phase II for Contract NAS1-18465 Processed Synthetic Aperture Radar (SAR) Data, sponsored by NASA Langley Research Center (LaRC). This report is second in a series of statistical reports. The overall effort has as its thrust the description of the ground clutter at an airport and in the surrounding area. In Phase I of this activity, SAR data of airports which existed in the ERIM SAR data archive were examined for utility to this program. Eight digital scattering coefficient images at high resolution and coarse resolution were created. The coarse resolution images were provided to NASA LaRC for use in their Microburst/Clutter/Radar simulation program and the high resolution images underwent a statistical clutter analysis at ERIM. In this phase of the program, SAR data were collected on an opportunity basis at the Philadelphia Airport using a set of radar parameters which more closely matched those which are anticipated to be encountered by an aircraft on its approach to an airport. This report describes these data and the results of the clutter study. During Phase III, a dedicated SAR mission was flown of the Denver Stapleton Airport and surrounding area. A wide variety of geometries and scene contents were acquired. These data and study results are presented in the third report.

The work reported here was performed by members of the Radar Science Laboratory, Advanced Concepts Division, Environmental Research Institute, under the direction of Dr. S.R. Robinson. The principal investigator for this project was Dr. R.G. Onstott. The contract was monitored by E.M. Bracalente, NASA Langley Research Center, Hampton, Virginia.

The authors gratefully acknowledge the support of the Radar Science Laboratory Staff during the project, in particular, Mr. Christopher Wackerman, Mr. Steven Lerman, Ms. Rita Woods, Ms. Janice Anquetil, Ms. Marsha Allen, and Mr. James Schipp.

TABLE OF CONTENTS

FOREWORD.....	iii
LIST OF TABLES.....	vi
LIST OF FIGURES.....	vii
I. INTRODUCTION.....	1
II. DATA COLLECTION.....	5
III. IMAGE DESCRIPTION.....	9
IV. PROCESSING AND CALIBRATION.....	11
V. CLUTTER ANALYSIS PROCEDURES.....	13
VI. CLUTTER ANALYSIS RESULTS.....	15
VII. CONCLUSION.....	23
References.....	81
Appendix A.....	A-1
Appendix B.....	B-1
Appendix C.....	C-1
Appendix D.....	D-1

LIST OF TABLES

1. Comparison of Preferred and Actual Radar and Geometry Parameters.....24
2. Image Composition Areal Analysis.....25
3. Statistical Summary of Backscatter Cross-Sections.....26
4. Hard Targets Represented as Sigma Values.....27

LIST OF FIGURES

1. SAR Imaging Geometry.....	28
2. SAR Imaging Geometry.....	29
3. P-3 SAR Swath Modes.....	30
4. SAR Data Collected of Philadelphia Airport and Surrounding Area on 7 October 1988.....	31
5. Bar Chart Presentation of Scattering Coefficients Values in the Philadelphia Airport Image.....	32
6. Histogram of Radar Scattering Coefficients for the Philadelphia Image.....	33
7. -30 dB Threshold.....	34
8. -20 dB Threshold.....	35
9. -10 dB Threshold.....	36
10. 0 dB Threshold.....	37
11. 10 dB Threshold.....	38
12. Distribution of Radar Scattering Cross Section for the Whole Airport Image.....	39
13. Residential Clutter Distribution (40° to 49° incidence angle)...	40
14. Residential Clutter Distribution (50° to 59° incidence angle)...	41
15. Residential Clutter Distribution (60° to 64° incidence angle)...	42
16. Residential Clutter Distribution (65° to 69° incidence angle)...	43
17. Residential Clutter Distribution (70° to 74° incidence angle)...	44
18. Forest Clutter Distribution (40° to 49° incidence angle).....	45
19. Forest Clutter Distribution (50° to 59° incidence angle).....	46
20. Forest Clutter Distribution (60° to 64° incidence angle).....	47
21. Forest Clutter Distribution (65° to 69° incidence angle).....	48
22. Forest Clutter Distribution (70° to 74° incidence angle).....	49

LIST OF FIGURES (cont.)

23. Forest Clutter Distribution (75° to 79° incidence angle).....	50
24. Grass Clutter distribution (40° to 49° incidence angle).....	51
25. Grass Clutter Distribution (50° to 59° incidence angle).....	52
26. Grass Clutter Distribution (60° to 64° incidence angle).....	53
27. Grass Clutter Distribution (65° to 69° incidence angle).....	54
28. Grass Clutter Distribution (70° to 74° incidence angle).....	55
29. Grass Clutter Distribution (75° to 79° incidence angle).....	56
30. Grass Clutter Distribution (80° to 84° incidence angle).....	57
31. Grass Clutter Distribution Including Values at Image Minimum (75° to 79° incidence angle).....	58
32. Grass Clutter Distribution Including Values at Image Minimum (80° to 84° incidence angle).....	59
33. Water Clutter Distribution (40° to 49° incidence angle).....	60
34. Water Clutter Distribution (50° to 59° incidence angle).....	61
35. Water Clutter Distribution (65° to 69° incidence angle).....	62
36. Water Clutter Distribution (70° to 74° incidence angle).....	63
37. Water Clutter Distribution (75° to 79° incidence angle).....	64
38. Water Clutter Distribution (80° to 84° incidence angle).....	65
39. Incidence Angle vs. Scattering Coefficient Plot for Forest Clutter.....	66
40. Incidence Angle vs. Scattering Coefficient Plot for Residential Clutter.....	67
41. Incidence Angle vs. Scattering Coefficient Plot for Grass Clutter.....	68
42. Incidence Angle vs. Scattering Coefficient Plot for Water Clutter.....	69
43. Polynomial Fit to Forest Data.....	70

LIST OF FIGURES (cont.)

44. Polynomial Fit to Residential Data.....	71
45. Polynomial Fit to Grass Data.....	72
46. Distribution Plot for the Airport Terminals.....	73
47. Distribution Plot for Building Clutter.....	74
48. Distribution Plot for Refinery Tank Clutter.....	75
49. Distribution Plot for Dock.....	76
50. Distribution Plot for Bridge Clutter.....	77
51. Distribution Plot for Plane Clutter.....	78
52. Distribution Plot for Barge Clutter.....	79
53. Distribution Plot for Parking Lot Clutter.....	80

I. INTRODUCTION

Low altitude microburst windshear represents a significant hazard to aircraft, particularly during take-off and landing; the intense down drafts and the resultant divergent outflow, can have a significant effect on the characteristics of the endangered aircraft. When encountered at low altitude, the pilot has little time to react correctly to maintain safe flight. The Federal Aviation Administration (FAA), jointly with the National Aeronautics and Space Administration (NASA), has sponsored an investigation into the development of airborne sensors to detect microburst windshear. One sensor of interest is the microwave Doppler radar operating at X-band or higher frequencies. Critical to the analysis of the capability of such a sensor to perform this detection is the microwave backscatter description of both the microburst event and the clutter background, especially during the approach and departure from an airport. The Environmental Research Institute of Michigan (ERIM) has provided NASA Langley Research Center (LaRC) with calibrated high-resolution synthetic aperture radar (SAR) images of selected airport scenes from the ERIM SAR data archive for use in their Microburst/Clutter/Radar simulation program and to statistically characterize the ground clutter surrounding these airports. In addition, statistical analyses of these airport environments have been performed by ERIM to describe the range of scattering conditions encountered.

NASA LaRC has developed this Microburst/Clutter/Radar simulation program to assess the performance of Doppler radars for this application and to test potential signal processing techniques. The simulation program models the output of an airborne Doppler radar as it views a low-level microburst along the approach to an airport. Inputs to this simulation include airport ground clutter data base, a simulated microburst data base, the operating parameters of the proposed weather radar, and candidate signal processing software for use in detection. In the operation of the simulator the received signal amplitude level for each range bin is calculated. Each range bin include contributions

from both the microburst and the ground clutter.

Many questions arose during this study. What is the general description of the airport clutter environment? How does this environment change from airport to airport? How complex does an airport scene have to become before it degrades detection? In general, the limits of detectability of microburst events must be established for an airborne Doppler radar to be an effective tool in the prevention of aircraft windshear catastrophes. ERIM has performed a clutter analysis of the Philadelphia Airport to extend the work done in Phase I to provide significant information for establishing limits of detectability. Clutter types, mean backscatter intensities, probability distributions, and areal extent of the clutter types in the image have been determined. With the analysis of the statistical characteristics of clutter in the scene, the effects of scene composition were studied. These results may then be extrapolated to describe the clutter at candidate airports.

The analysis of the eight images from ERIM's archives in Phase I of this three phase program has provided important information concerning clutter returns from airport scenes. Clutter backscatter responses for the same clutter type were found very similar. Differences in their means were attributable to differences in incidence angle. Probability density functions which describe the scattering of a particular clutter type were nearly identical from image to image. This is an important result because it indicates a high degree of stability in the returns which would be expected from clutter around an airport. A Doppler radar designed to detect Microburst windshear at one particular airport may not have to compensate radically for different clutter scenes as the plane travels from airport to airport. Through the analysis of these eight images we gained information about the types and characteristics of radar clutter surrounding airports. However, further analysis of strongly backscattering clutter regions was needed. The data analyzed in Phase I indicated that although only a fraction of the clutter surrounding the airport is of an intensity to be of concern, almost all of it is located on the airport grounds. It was concluded that detailed

analysis of the clutter from specific types of buildings, planes, and other airport vehicles should be performed, and that the motion of vehicles and planes needs to be examined.

As anticipated, the data in the SAR archive, by itself, did not have the breadth to fully describe the range of airport clutter scenes possible. This, of course, was the impetus behind Phases II and III, which was to collect additional clutter data on a not-to-interfere basis during the calibration flights of a new SAR sensor, and to conduct a dedicated SAR data collection. The SAR archive allowed us to begin a statistical survey of the clutter environment at a few selected airports. This information was enriched in Phase II by gathering data at smaller depression angles. It was also determined by NASA LaRC personnel that an airport scene of 13 km x 13 km was optimum. In Phase I images were limited to sizes of about 6 km x 13 km. These scenes were then filled in by a variety of techniques employed by NASA LaRC personnel. During the Philadelphia collection usable data over a 13 km x 13 km region were acquired.

During this phase the goal was to make use of the opportunity to acquire airport clutter during the test and evaluation flights of a new radar, commonly referred as the NADC/ERIM P-3 SAR, designed for remote sensing applications. The goal was to collect data on a not-to-interfere basis using the geometry and radar parameters specific to the Wind Shear Detection clutter problem. A number of opportunities presented themselves, but did not result in the desired collection of data (i.e., because of weather, system problems, and tight schedules). Data were collected of the Key West Naval Air Station (15 January 1988), Willow Run Airport (17 May 1988), and Whidbey Island Naval Air Station (16 July 1988). The maximum incidence angle for these images was 74° and the clutter was not extensively urban so these data were not exploited. On 7 October 1988, SAR data of the Philadelphia Airport which is located in a densely populated area were collected using the geometry and primary radar parameters that were judged the most optimum. The analysis of these data is the object of the discussion of this report.

II. DATA COLLECTION

The radar used during this data collection operates at frequencies of 1.25, 5.26, and 9.375 GHz. It is fully polarimetric, able to record 4 complex images, operates in the strip map mode, and is capable of producing 1.6 meter range by 2.2 meter azimuth resolution images. Four high density recording channels are available, each capable of recording 4096 range elements. The operator is able to select wavelength, transmit polarization, receive polarization, fine or coarse (1.6 to 3.2 m), range resolution and slant range for each channel. It is possible to operate in a wide swath mode so that a 32 km strip map is made at one wavelength and one polarization or the four channels can be used to record at one frequency, all four linear polarizations, and fine resolution over a 6 km range interval.

A more detailed description of the SAR is provided in Appendix A. A data collection plan was developed to provide SAR data which closely matches the geometry of an aircraft on its landing approach. The various radar parameters and geometries are addressed individually below. The preferred and actual SAR configurations are detailed in Table 1. The planned SAR imaging geometry is provided in Figures 1 and 2.

Frequency

The P-3 SAR operates at 1.25, 5.25, and 9.375 GHz. The frequency of 9.375 GHz (X-band) was selected because it corresponds with existing X-band weather radars which have proven useful in detecting weather related features.

Polarization

The P-3 SAR Facility is fully polarimetric. This means that up to four complex images at VV, VH, HV, and HH polarizations may be recorded at the selected frequency of operation. The first letter indicates the transmit polarization and the second the received polarization. The

letter V is for vertical and H is for horizontal. With the recording of these four complex images additional images at arbitrary transmit and receive polarizations can be synthesized (i.e., circular polarization). Recording the four complex images also allows for the complete description of the scattering properties (i.e., by providing the cross-correlation information between the scattering coefficients) of the various elements within the clutter scene. Such information is critical to the understanding of the scattering mechanisms at play, and potentially to the determination as to whether troublesome scattering scenes may be suppressed. During this data collection, priority was given to recording four complex, 12 km x 12 km images (VV, VH, HV, and HH). These were produced in one pass using coarse resolution.

Depression Angle

An aircraft during its final approach is typically flying on a 3 degree glide slope. To simulate this glide slope during the SAR data collection, it was considered optimum if images were centered about a 3 degree depression angle. Depression angle is defined as the angle off the horizon and is equal to 90° -incidence angle.

Resolution

For any swath modes recorded, the P-3 SAR can operate either in high resolution, with an azimuth resolution of 2.8 m, and a range resolution of 1.6 m, or in low resolution, with an azimuth resolution of 2.8 m and a range resolution of 3.0 m. Using low resolution, the range coverage of each channel is 9830 m, and using high resolution, the range coverage of each channel is 4915 m. Since the goal here was to produce a 13 km x 13 km image about the airport, coarse resolution was chosen so that four complex 12 km x 12 km images (VV, VH, HV, and HH) may be produced in one pass. Operation in this mode was selected since the final images would be digitally processed to a resolution of 20 m.

Image Size

An image about 13 km x 13 km with the airport touchdown point near the center of the image was considered optimum by NASA LaRC personnel. The system may be operated in three different swath modes. The configuration of these swath modes is illustrated in Figure 3. In single-swath mode (Figure 3a), the radar collects the same range coverage in each channel using four different frequency and polarization combinations. In double-swath mode (Figure 3b), twice the range coverage of single-swath mode is recorded but only two frequency and polarization combinations can be used. In quad-swath mode (Figure 3c), four times the range coverage of single swath mode is recorded but only one frequency and polarization combination can be used. In double- and quad-swath mode there is no range overlap between channels that are contiguous in range. Images of 12 km x 12 km may be formed in 1 pass using the double swath-mode and was selected.

Airport/SAR Orientation

To simulate the geometry of what a doppler radar will see on final approach, the SAR needed to be oriented such that the path of the aircraft was perpendicular to the main runways of the airport. If additional passes were possible then alignment with secondary runways was proposed to provide complementary views of the airport from which aspect angle dependence would be studied and the composition (i.e., grass, forest, urban, etc.) of the airport scene may be supplemented.

Airport Selection

The P-3 SAR flights made during this period were strongly driven by the desire to fully document sensor performance. It was anticipated that there would be numerous opportunities to gather these data on an opportunity basis. It was originally planned to establish calibration arrays at Willow Run Airport which were to serve as the primary test

site for the SAR calibration program. During the planning stage of this phase it was not known that opportunities at other airports would be possible. The need to examine a variety of airports with their unique clutter environments was recognized.

III. IMAGE DESCRIPTION

The SAR data shown in Figure 4 were collected of the Philadelphia International Airport on 7 October 1988. Using a frequency of 9.35 GHz and a horizontal transmit and receive polarization. The radar was flown at an altitude of 5287 feet and grazing angles subtended by the image ranged from 7.8° to 52.2° . The radar was flown with a heading of 180 degrees and a look direction of 270 degrees. North is at the left of the image.

The Philadelphia International Airport is located near the center in the far range of the image. The main terminal and concourses can be seen in some detail, and some of the runways are visible. To the south of the airport is the Delaware River. Ships were observed in transit and at the far east (top) portion of the image a ship wake is observed. South of the river is rural southern New Jersey. Most of this area appears to be parks, open fields, or residential areas. On the far south eastern shore of the Delaware River is an oil refinery. One of the arrays of bright returns is the refinery whereas the other arises from a field of storage tanks. The strong returns which extend into the river near the refinery are the shipping terminals.

Just north of the airport is Interstate 95. Following the interstate east from the airport is Fort Mifflin U.S. Army Base, which lies at the junction of the Delaware and Schuylkill Rivers. The very bright area and the apparently grassy area east of the Schuylkill River and south of Interstate 95 are both part of the Philadelphia Naval Shipyard.

Directly north of the interstate and the shipyard are some interesting urban features. The golf courses and lakes of F. D. Roosevelt Park appear as darker areas just north of the bright part of the shipyard. To the east of the park is a sports complex which consists of Veteran's Stadium, J. F. Kennedy Stadium, and Spectrum Sports Arena. Parking areas surround these facilities. Lightpoles within these lots can be seen. To the north of the sports complex and extending to the north is downtown Philadelphia.

THIS PAGE INTENTIONALLY
LEFT BLANK

IV. PROCESSING AND CALIBRATION

Processing and calibration of the image proceeded in much the same manner as the images processed from the SAR archive, the object of the work done during Phase I. Refer to Volume I of this series of reports (Onstott and Gineris, 1988) and to Appendix B for a description of this calibration procedure. The procedure deviated slightly due to recent modifications in the processor which enabled us to produce an image with the full ground coverage desired, instead of an image produced from the mosaicking of multiple images. The resultant phase history tape used for the Philadelphia image represents a 8192 element by 4096 element file. With a pixel spacing of 1.62 m in azimuth and 2.4 m in range, the Philadelphia image is produced from a reflectivity map of a 13,271 m by 9830 m area.

As with the archival images, the phase history of the Philadelphia image was focused in azimuth and range. This was achieved by convolving the data with a match filter of the transmitted radar chirp in azimuth and range. The data were processed to remove the effects of system noise and were then radiometrically corrected to compensate for the effects of range fall-off, the antenna gain pattern, and resolution cell power. The radiometrically corrected image was then converted to normalized radar cross-sections (NRCS) by normalizing the magnitude of the scattering cross-sections by the resolution area. The terms scattering coefficients and NRCS will be used interchangeably.

The absolute calibration of the Philadelphia Airport image was performed based on data collected at the Patuxent Naval Air Test Center, Maryland, two weeks prior to the Philadelphia collection. For a radar operating in its linear region, a linear relationship will exist between the measured intensity of a point target in an image and the expected value of the backscattering cross-section of the target. The slope of the function is unity and the y-intercept of the function is a measure of the system gain function. The system gain function determined from the Patuxent data was then applied to the Philadelphia collection by accounting for short term variations in receiver gain and transmitted

THIS PAGE INTENTIONALLY
LEFT BLANK

V. CLUTTER ANALYSIS PROCEDURES

In establishing the criteria for which microburst events can be detected, a careful statistical characterization of airport clutter is required. The questions that arose immediately were: what are the types of clutter which commonly occur at an airport, how does the clutter environment change with incidence angle and polarization, and what is the density and location of strong returns at an airport? The Philadelphia data were examined to address these questions. This analysis was performed on 4096 element x 4096 element, slant range σ^0 image with the finest resolution possible to allow precise sampling of both distributed and point targets. This image has one independent sample per resolution cell.

The first step in our analysis was to characterize the area surrounding the Philadelphia International Airport. This area is a mixture of industrial, suburban, and rural communities. Two analyses were performed to quantify the amount and characteristic clutter return of each type of community in the image. The first analysis performed was the differentiation of the image into its various constituent communities. The results of this areal analysis were tabulated and the percentage of each community within the image calculated. A second analysis was performed in which the image was divided into σ^0 clutter groups at intervals of 5 dB. This enabled us to locate and quantify sources of similar backscatter intensity.

Using standard statistical techniques, we performed an analysis of each major clutter type as well as the unique clutter areas. Regions of critical clutter types were located and the means, standard deviations, and coefficients of variation were calculated using the techniques described in Appendix C. Coefficients of variation were determined to examine the uniformity of these subregions. Most distributed targets have low coefficients of variation indicating the backscatter intensity does not vary widely from the mean value. Man-made targets typically have high coefficients of variation. The few pixels of very high returns are often times embedded in a background of low returns. The

VI. CLUTTER ANALYSIS RESULTS

The image composition areal analysis of the Philadelphia International Airport and surrounding area is presented in Table 2. About 33% of the image is composed of water, i.e., the Delaware and Schuylkill Rivers. Another 18% of the image is comprised of fields, forests, and croplands. The majority of these areas lie to the south of the Delaware River in New Jersey, although some of the 'field' areas considered in the analysis are part of the park/army base/naval shipyard complex directly to the east of the airport. Industrial complexes (east of the airport) make up approximately 14% of the image content and the airport grounds itself occupy about 6%. About 16% of the far range image has scattering coefficients which are less than about -35 dB. The industrial areas to the east of the airport will be shown to represent the greatest clutter hazard, especially since it lies almost directly in the path of the major runways at the airport.

Table 3 and Figure 5 present the mean, minimum value, maximum value and standard deviation for the scattering coefficients of each of the major clutter types in the SAR image. The location and statistics of individual clutter areas are given in Appendix D. From the bar chart provided in Figure 5 we see that, with the exception of the parking lot, every man-made hard target clutter group has a NRCS of -8 dB or greater. This correlates well to the results seen previously in the archival data. Distributed targets NRCS values are -20 dB and below. The parking lot filled with cars has a mean of -15 dB and does not fit into either of these two categories. This may be due to the composite nature of the parking lot. The coefficient of variation for the parking lot clutter area has a value of 15, one of the largest coefficients of variation in all of the data sets. A mixture of very large NRCS values, as would be expected from vehicles, and very low, as would be expected from a concrete or asphalt surface, would produce a mean NRCS value somewhere between the two extremes and a large coefficient of variation. For this image the mean NRCS was about -15 dB, with the largest NRCS measured of about 34 dB. The coefficient of variation has a value of

66.0, indicative of the very diverse nature of this image.

Given that the scattering coefficients of the image tended to separate into either man-made or natural distributed-target the thresholding of the image allowed us to further determine the location and percentage of specific types of clutter. A histogram of radar scattering coefficients for the entire image and for 5 dB bins is provided in Figure 6. The images shown in Figures 7 through 11 were produced by setting individual pixels whose values are below the stated threshold to zero (black areas in the images) while pixel values equal to or greater than the threshold are set to 255 (white areas in the images). It should be noted that this operation has been performed on the compressed (≈ 19 m resolution) version of the calibrated image. Because image compression involves averaging the distribution of coefficients, the resulting range of values is smaller, as expected, and the lowest and highest resulting coefficients will differ from those presented elsewhere.

Based upon the bar chart shown in Figure 6, we see that fifty-four percent of the image has a value of -28 dB or less. Figure 7 reveals that these low return areas arise primarily due to the water and unclassified areas of the image. Low returns also exist in the residential and parking lot areas. Thirty-four percent of the image has NRCS values between -18 dB and -28 dB. These areas include almost all of the distributed targets. Figure 8 shows all returns which are greater than -20 dB. The natural targets which produce NRCS values greater than -20 dB are shorelines, treelines, and certain tree returns. All other returns appear to be manmade in origin. This behavior was also suggested in the bar chart shown in Figure 5. The -15 dB to -20 dB NRCS value range appears to demarcate natural distributed returns from hard-target returns. At the -10 dB threshold, Figure 9, most of the returns which are visible come from hard-target sources. Most prominent are the returns from the naval shipyard, the airport terminal, the oil refineries, boats, and docks. A very small percentage of the returns with values above -10 dB come from the 'residential' areas in New Jersey south of the naval shipyard. These returns may actually be coming from

homes and other buildings dispersed throughout this area. Only 1.2% of the image has values of 0 dB or above and the majority of these returns are localized at the naval shipyard, the airport, and a few developed locations along the river and south of the airport as shown in Figure 10. These clutter scenes produced the strongest returns in this entire image and are directly in the line of approach of the major airport runways. This is further illustrated in Figure 11 where the image thresholded at the +10 dB level.

Histograms of radar scattering coefficients were calculated for the various clutter scenes as well as for the image as a whole and are presented in Figures 12 through 38. In Figure 12, the distribution of the NRCS values for the entire image is presented. The values in the image are range from +34 to -36 and have a mean of -15 dB and illustrates the diverse of the clutter groups contained within a typical airport clutter scene. The histograms shown in Figures 13 through 38 are plotted as a function of incidence angle, as listed in each figure in parenthesis along side the clutter type. In the incidence angle range where scattering coefficients are stable, (40° to 60°) 10° incidence angle bins were used. In that range where sharp changes in scattering coefficient value are expected, (0°) 5° bins were used. The incidence angle is equal to 90-depression angle.

Figures 13 through 17 present the percent of occurrence of NRCS values of residential clutter for five incidence angles (90-depression angle) ranges. The mean NRCS value changes slowly with the incidence angle in the range from 40° to 75° and fall within a 2.5 dB interval. There is also very little change in the shape of the distribution. In all cases, the shape of the distribution at the high end is nearly identical, while the weak returns are much more sensitive to changes with incidence angle. The insensitivity of the strong returns may be attributed to man-made targets. The modulation of the weak return may come from changing tree/ground interactions. The width of the distributions also varies with incidence angle, but the change was not systematic. The results for 'forest' clutter are presented in Figures 18 through 23. In general, their cross-sections are 2 to 3 dB lower

than those from the residential areas and decreased approximately 4 dB with increasing incidence angle (decreasing depression angle). The forest clutter distributions are more symmetrical than those of the residential clutter, do not change shape with incidence angle, and are similar to the distributions obtained using the SAR archival data discussed in Report I.

Unlike the data acquired from the SAR archive, the residential and forest areas surrounding the Philadelphia Airport were not similar. The distributions of the residential clutter are broader and shorter than those of the forest clutter areas and the mean of the residential clutter is consistently higher than those of the forest clutter for all incidence angle groups. The coefficient of variation of the residential areas are generally a factor of ten greater than those of the forested areas. This may be due to the diversified nature of the residential area. The residential areas not only have trees; they also include bright hard targets such as houses and cars, and very low return areas such as lawns and streets.

Figures 24 through 30 present histograms of the scattering coefficients of grass for various incidence angle ranges. The mean NRCS was almost constant at -24 dB for incidence angles from 40° to 75°. A 3 dB reduction occurred when angles increased from 75° to 85° region. This tendency was typical for distributed targets. Interestingly, grass scattering cross-section were only 2 to 3 dB lower than those for forest, a difference which is significantly smaller than predicted by published data. There is always an uncertainty in the clutter characterization when based on topographical and use planning data. This, of course, could be corrected with ground truth. Areas which were classified as grass may include vegetation which produces much larger backscattering cross sections than those typically associated with grasslands. Forested areas may also not have been heavily canopied, hence would produce a weaker backscatter. The areal coverage of forest in the Philadelphia Image was not as extensive as that seen in archival imagery, and the character of this forest clutter is probably different.

The coefficient of variation for the grass clutter groups is stable and the shape of the distribution of values changes very little in the 40° to 75° incidence angle range. In the 75° to 85° range the shape of the distribution is similar to that of the other clutter groups, however, these were provided with a much smaller number of pixels, because the majority of the pixels had values too close to the minimum measurable NRCS (Figures 31 and 32).

The results of the analysis of the backscatter from water are presented in Figures 33 through 38. The source of the water is the Delaware River. Inland bodies of water are small and are typically sheltered, reducing the surfacing roughening effect possible because of winds. Water returns were expected to be low and in a range from -30 dB to -45 dB. The minimum measurable NRCS in the image is -36.17 dB. Of the six incidence angle ranges examined, 97% to 99% of the water data were at or below the minimum value.

The runway areas of the image produced much the same results as the water areas. Experimental backscatter coefficients for asphalt and concrete surfaces at 75° to 85° (the location of the Philadelphia Airport in the scene) range from -35 dB to -40 dB. Analysis results show that all pixels had values of -36.17 dB or less.

The variation of the magnitude of the scattering coefficients with incidence angle are presented in Figures 39 through 42 for each of the distributed clutter groups examined in this image. For the three major clutter groups observed in this SAR image we would expect to find that the backscatter response exhibits a plateau in the middle angle region which is then followed by a reduction in backscatter intensity with increasing angle. The forest and residential backscatter was essentially insensitive to increasing incidence angle in the region from 45° to 75° while grass started to decrease ground 70°.

The water backscatter response is constant at -36 dB from 45° to 78° because it is at or below the noise floor of the measurement system. The sharp rise at 80° incidence angle may be due to system noise effects. Most system noise was removed from the image, but it was statistically not possible to remove all of the system noise without

seriously degrading the image. Any system noise that remained, especially at far range, was boosted by the radiometric correction and in this case, may have produced scattering coefficients with large errors.

A fourth order polynomial was used to describe the backscatter response of forest, residential, and grass with angle. These fits are shown in Figures 43 through 45. The polynomial provides a good fit to the forest and grass clutter, but a less satisfactory for the residential data. At the middle incidence angles (48° to 65° incidence angle), the polynomial fits the residential data well, but falls too quickly at the larger angles (68° to 78°). An updated antenna pattern was used in the radiometric correction of the incidence angle data used in these fits.

A number of man-made targets were analyzed which were located in the vicinity of the airport. A chart of these targets and their corresponding radar cross-section value is presented in Table 4. The RCS (σ), in square meters of the target was determined by:

$$\sigma = r_a r_y \cdot \sum_{i=1}^N \sigma_i^o \quad (\text{Eq. 1})$$

where σ_i^o = backscattering coefficient for an individual pixel
 N = number of pixels in extended by a target
 r_a = azimuth pixel spacing
 r_y = range pixel spacing

Most of the hard targets analyzed around the Philadelphia Airport have RCS values of 20 dBsm or greater with the exceptions of parked automobiles which have values from 5 dBsm to 15 dBsm. It is noted that even at very large incidence angles (75° and above) many large hard targets have RCS values above 35 dBsm. The RCS of docks, increased with increasing incidence angle and correlates with the response of a dihedral formed between the smooth water and a vertical concrete structure. Among the other hard targets no clear trends exist because of differences in effective areas and aspect angles of the targets.

Distributions of man-made clutter are presented in Figures 46 through 53. These distributions are of normalized radar cross-section values (NRCS), which are calculated by dividing the radar cross-section values discussed above by the effective area of the target. Figures 46 through 50 present the distributions of non-vehicular hard targets. The airport terminal building and refinery tank distributions seem to have some common shape characteristics. All have steeply increasing trends on the low cross-section side of the distribution and a more gradually decreasing trends with large cross-section. The building distribution, Figure 47, show an additional flatter trend at small NRCS values which the other distributions do not have. Similar trends in their distributions may be caused by similar geometries. The buildings, terminals, and refinery tanks can probably be represented by a dihedral formed with a conducting vertical side and dielectric horizontal side. All three of these objects probably have some top hat like structures on their roofs as well. The distribution plot for the docks, Figure 49, in the image has a different shape than the three previous hard-targets. The docks produced distributions which are symmetric. The docks represent a unique hard-target geometry. They are a flat conductive plane sitting up above a conductive surface separated by several conductive or dielectric poles. This structure is complicated and not well-modeled by a simple dihedral. The distribution for bridge clutter, Figure 50, shows characteristics of both types of hard targets. The histogram for the bridge clutter appears to be more symmetrical than that of the buildings, terminals, and refinery tanks, but the sides of the distribution are much steeper than that of the docks.

The histograms for the vehicular hard targets are presented in Figure 51 through 53. The serrated appearance of the plane and barge plots is due to the small number of pixels used in the distributions. All three cases seem to separate themselves into a group of values at the image minimum (in the system noise) and a group of values at a larger scattering coefficients. The pixels at the image minimum are pixels containing background clutter and weak vehicle scatter. Pixels at larger RCS values are those from the dominant vehicle scatters The

distribution for the parking lot has three main lobes, one at the image minimum, one around -27 dB and one around -4 dB. The sources of the two higher lobes in the distribution may be automobiles at different aspect angles or a combination of automobiles with other parking lot features such as lightpoles.

VII. CONCLUSION

The target-of-opportunity image of the Philadelphia International Airport was the first image in the NASA windshear program to be collected at small depression angles (7.8°). As such, this image represented a unique opportunity to expand the knowledge of the backscatter characteristics of clutter to a small depression angles.

Probably the most distinguishing feature of this SAR image is the large areal extent of clutter in which the backscatter was so weak that it is probably of no consequence to the ability to detect microburst windshear in a ground clutter environment and that the backscatter was so weak as to not be measurable (i.e., scattering coefficients were smaller than -36 dB) At depression angles smaller than about 13° (which represent an area equal to about one half width of the image) virtually all distributed targets were buried in system noise. Even at the largest depression angles the distributed targets such as forests, fields, water, and residential rarely had mean scattering coefficients greater than -10 dB. This is consistent with trends observed in the archival SAR data which was reported in the Phase I report.

As found in the Phase I statistical analysis, forest and residential clutter are very similar. Residential areas produces backscatter which is approximately 2 dB greater than for forest clutter. Both show an insensitivity to incidence angle in the range from 45° to 82° and, in both cases, the backscatter is moderately weak with scattering coefficients of about -20 dB. Overall, only a very small percentage of the image is composed of high returns, about 3% of the returns were greater than -5 dB. Sources which produced the largest cross-sections were largely confined to the airport grounds and areas highly industrialized. Unlike the original archival data, where more of the high backscatter returns are from areas outside of the airport grounds, this scene more closely emulates an airport in an urban setting and a more complicated clutter environment, which is a good case to be exercised in the NASA Radar Simulation Program.

**TABLE 1. COMPARISON OF PREFERRED
AND ACTUAL RADAR AND
GEOMETRY PARAMETERS**

<u>Parameter</u>	<u>NASA Ideal Scenario</u>	<u>Philadelphia Data</u>
Depression Angle Range	3°	7.6° to 52.2°
Swath		
Along - Track	8.48 km	13.3 km
Across - Track	10.44 km	9.8 km
Altitude	1565 m (5133')	1612 m (5287')
Airport Position	4 km from far range edge	2 km from far range edge
Polarization	HH	VV, VH, HV, HH
Resolution	<20 m x 20 m	2.4 m x 3.24 m

TABLE 2. IMAGE COMPOSITION AREAL ANALYSIS

<u>Clutter Scene</u>	<u>Percent of Total Image Area</u>
Airport Grounds and Terminal	5.9
Industrial	13.7
Residential	13.5
Fields and Croplands	10.2
Forest	8.2
Water	32.9
Areas Unclassified	15.6

TABLE 3. STATISTICAL SUMMARY OF BACKSCATTER CROSS-SECTIONS FOR VARIOUS CLUTTER TYPES NEAR THE PHILADELPHIA INTERNATIONAL AIRPORT

	<u>Mean (dB)</u>	<u>MIN (dB)</u>	<u>Max (dB)</u>	<u>SDev (Mag)</u>	<u>(Mean + SDev) / Mean</u> (dB)
Forest (50-59)	-22.56	-36.17	-8.72	0.7227 x 10 ⁻²	3.62
Grass (50-59)	-24.40	-36.17	-6.96	0.5175 x 10 ⁻²	3.85
Residential (50-59)	-20.95	-36.17	14.01	0.1449 x 10 ⁰	12.80
Water (50-59)	-36.12	-36.17	-26.94	0.4154 x 10 ⁻⁴	0.68
Runway	-36.17	-36.17	-36.17	0.1896 x 10 ⁻⁷	0.00
Terminal	3.99	-36.17	27.03	0.1781 x 10 ⁻²	9.09
Industrial	-7.35	-36.17	29.68	0.3497 x 10 ⁻¹	13.01
Parking Lot	-14.75	-36.17	20.31	0.9879 x 10 ⁰	14.84
Planes	-1.76	-36.17	9.03	0.1380 x 10 ⁻¹	4.87
Barges	3.05	-36.17	17.14	0.5294 x 10 ⁻¹	5.59
Buildings	0.48	-36.17	27.93	0.1073 x 10 ⁻²	10.26
Docks	-1.36	-36.17	23.93	0.4371 x 10 ⁻¹	8.44
Bridges	4.37	-36.17	19.77	0.8707 x 10 ⁻¹	6.22
Refinery Tanks	-4.98	-36.17	18.73	0.2894 x 10 ⁻¹	10.05

Table 4. Hard Targets Represented as σ

Identifier	Region	Θ	σ (dBsm)	Effective Area (m ²)
H1	Dock	60.37	33.84	7573.82
H2	Dock	63.49	35.14	7589.38
H3	Dock	65.20	36.15	7690.46
H4	Dock	72.26	38.74	7612.70
H5	Dock	72.88	38.39	7636.03
H6	Dock	73.55	34.35	7394.98
H7	Dock	74.25	41.08	7737.12
H8	Bridge	76.42	27.28	777.60
H9	Bridge	76.72	33.30	777.60
H10	Bridge	76.87	37.15	777.60
H11	Bridge	77.10	32.77	777.60
H12	Football Stands	71.05	26.19	4611.17
H13	Arena	70.19	38.89	42698.02
H14	Bridge	75.73	33.71	777.60
H15	Bridge	78.79	20.06	373.25
H16	Bridge	78.92	24.85	334.37
H17	Terminal	81.40	37.80	1407.46
H18	Terminal	81.75	43.59	2099.52
H19	Plane	81.17	24.84	178.85
H20	Plane	81.84	22.08	124.42
H21	Warehouse	80.04	34.70	5116.61
H22	Barge	78.17	25.32	326.59
H23	Barge	78.75	31.15	2122.85
H24	Refinery Tank	53.63	29.08	6772.90
H25	Refinery Tank	55.56	33.08	4712.26
H26	Refinery Tank	56.88	32.99	4758.91
H27	Refinery Tank	58.03	32.85	4813.34
H28	Hangar	80.28	36.44	816.48
H29	Hangar	80.91	39.17	2177.28
H30	Ship	80.91	37.83	1458.22
H31	Building	69.46	30.92	11749.54
H32	Building	78.84	42.32	19813.25
H33	Building	82.44	42.49	4922.21
H34	Barge	82.25	31.56	373.25
H35	Barge	82.32	36.30	349.92
H36	Building	81.34	47.24	3654.72
H37	Parked Auto	68.14	8.19	23.33
H38	Parked Auto	68.25	5.62	23.33
H39	Parked Auto	68.34	-17.17	7.78
H40	Parked Auto	68.43	9.62	23.33
H42	Parked Auto	68.47	14.65	23.33

Parameter	Value
Altitude	1524 m
Depression Angle	8°
Distance to Touchdown Point	10844 m
Resolution	2.7 m * 3.0 m
Pixel Spacing	1.62 m * 2.4 m
Image Size	12 km * 9.8 m
Polarizations	VV, VH, HH, HV
Frequency	X-Band

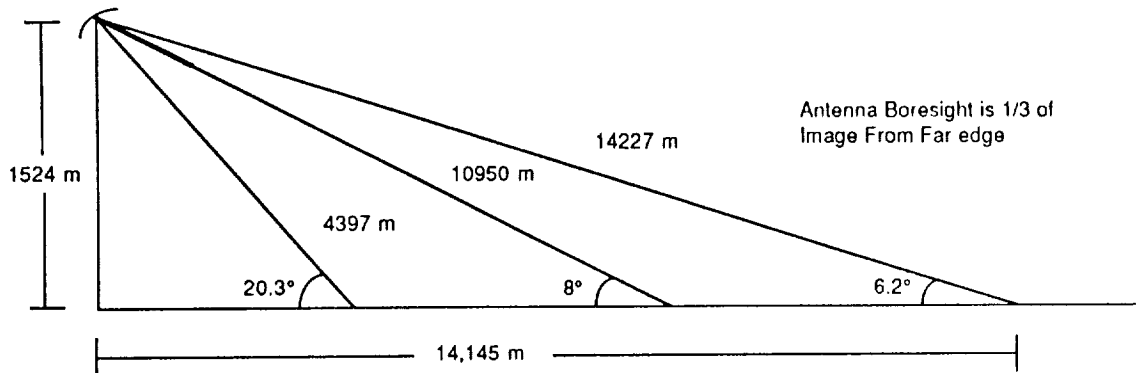


Figure 1. SAR Imaging Parameter

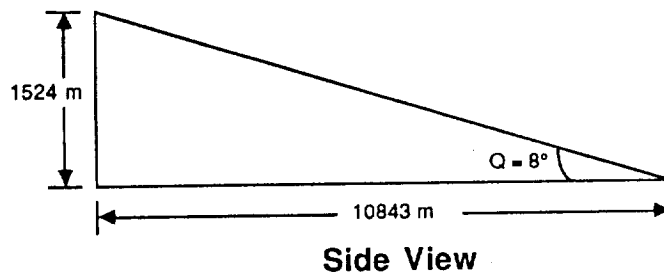
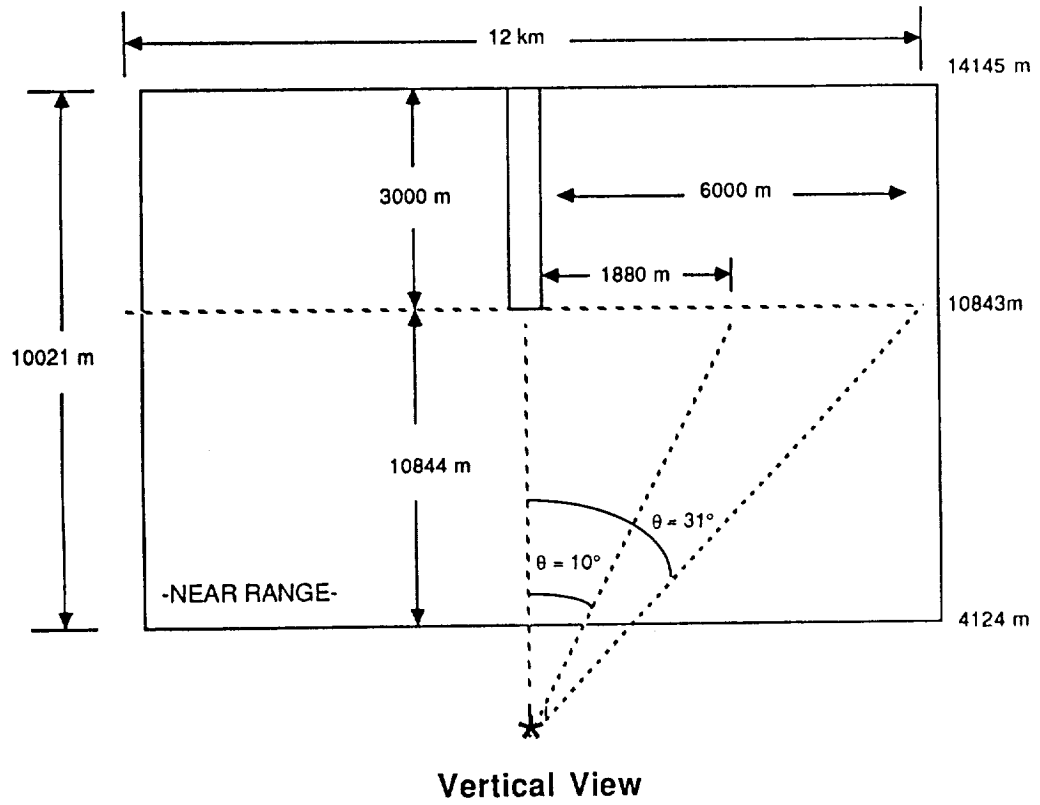


Figure 2. SAR Imaging Geometry

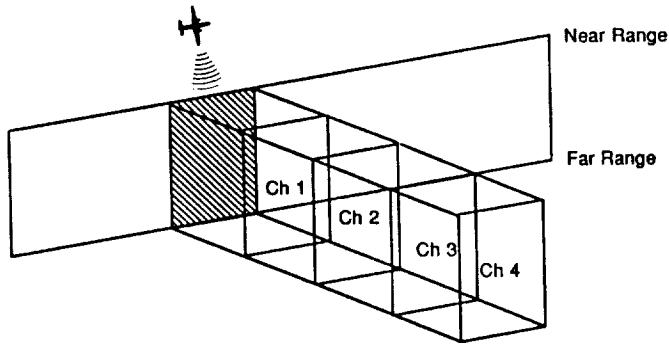


Figure 3a. Single-Swath Mode

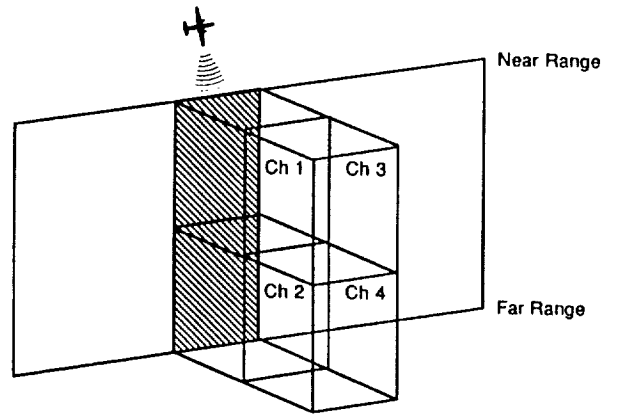


Figure 3b. Double-Swath

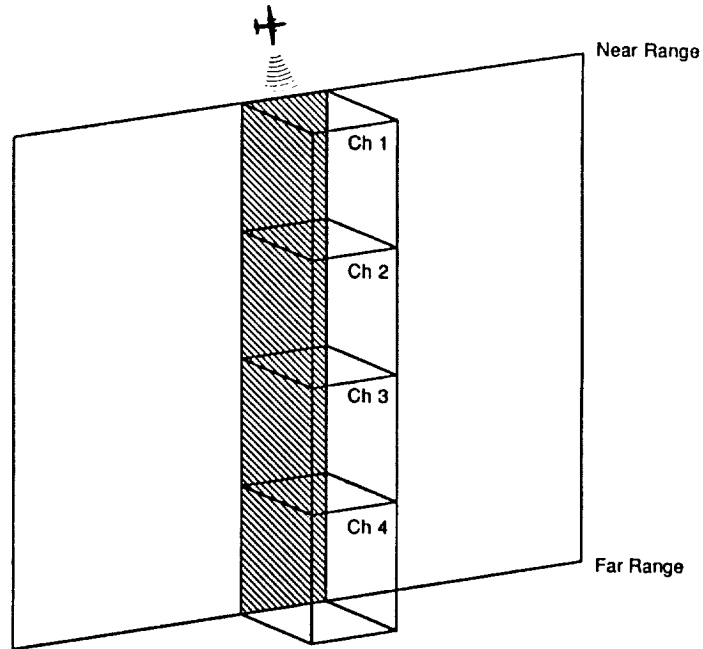


Figure 3c. Quad-Swath Mode

Figure 3. P-3 SAR Swath Modes

ORIGINAL PAGE
BLACK AND WHITE PHOTOGRAPH

ORIGINAL PAGE IS
OF POOR QUALITY

89-11846

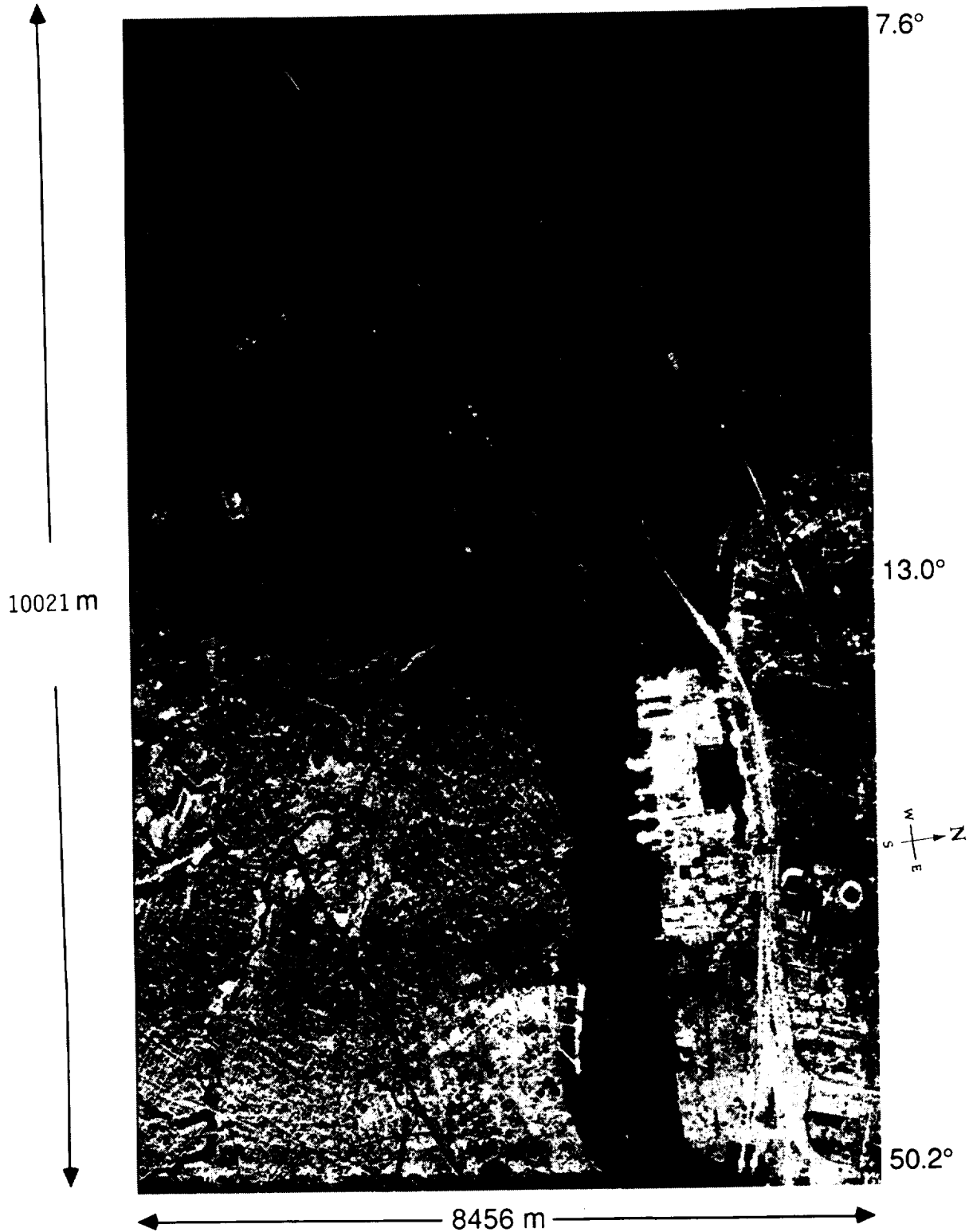


Figure 4. SAR Data Collected of Philadelphia Airport and Surrounding Area on 7 October 1988

Bar Chart Presentation of Means and Standard Deviations

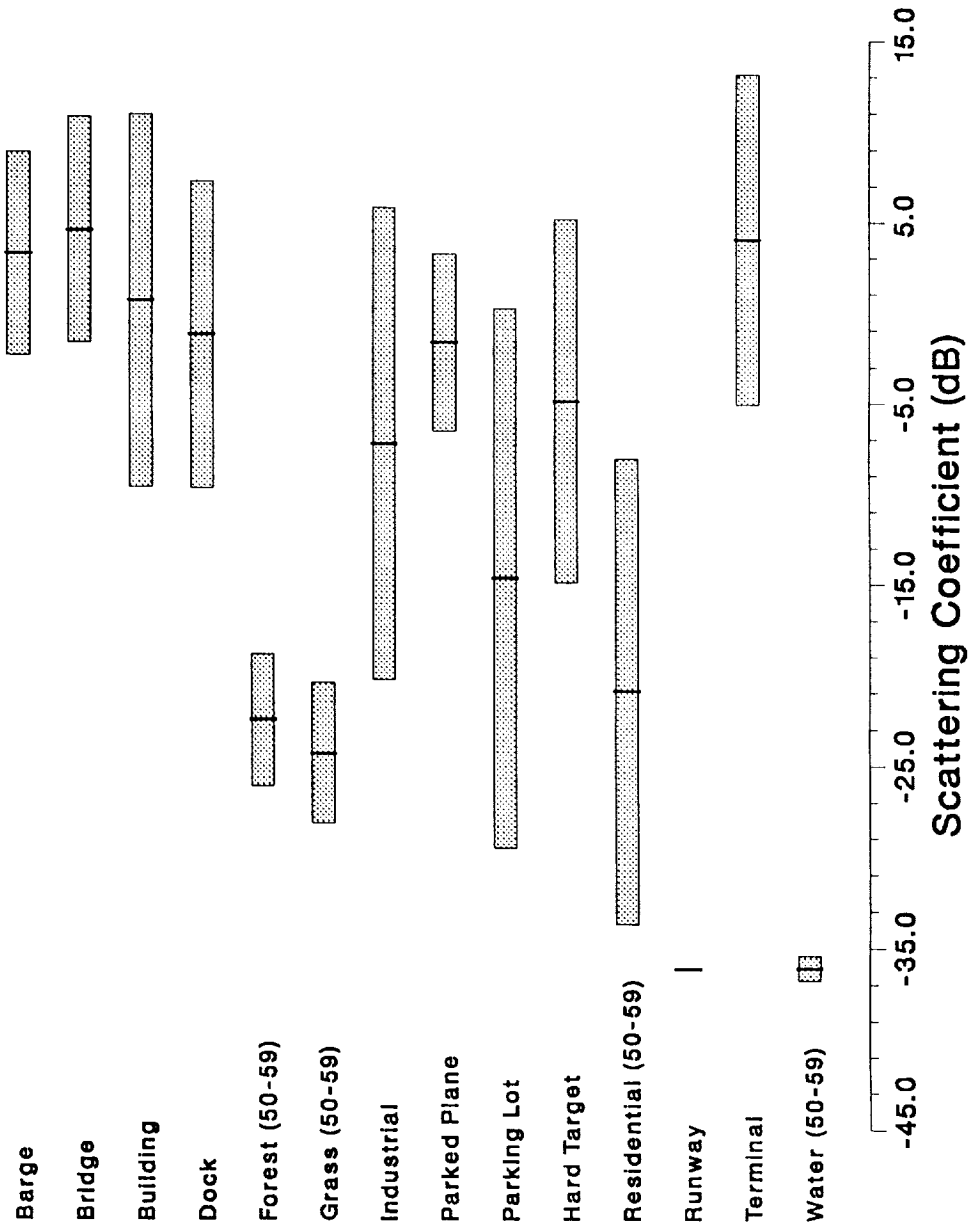


Figure 5. Bar Chart Presentation of Scattering Coefficients for a Variety of Clutter Types Near the Philadelphia Airport

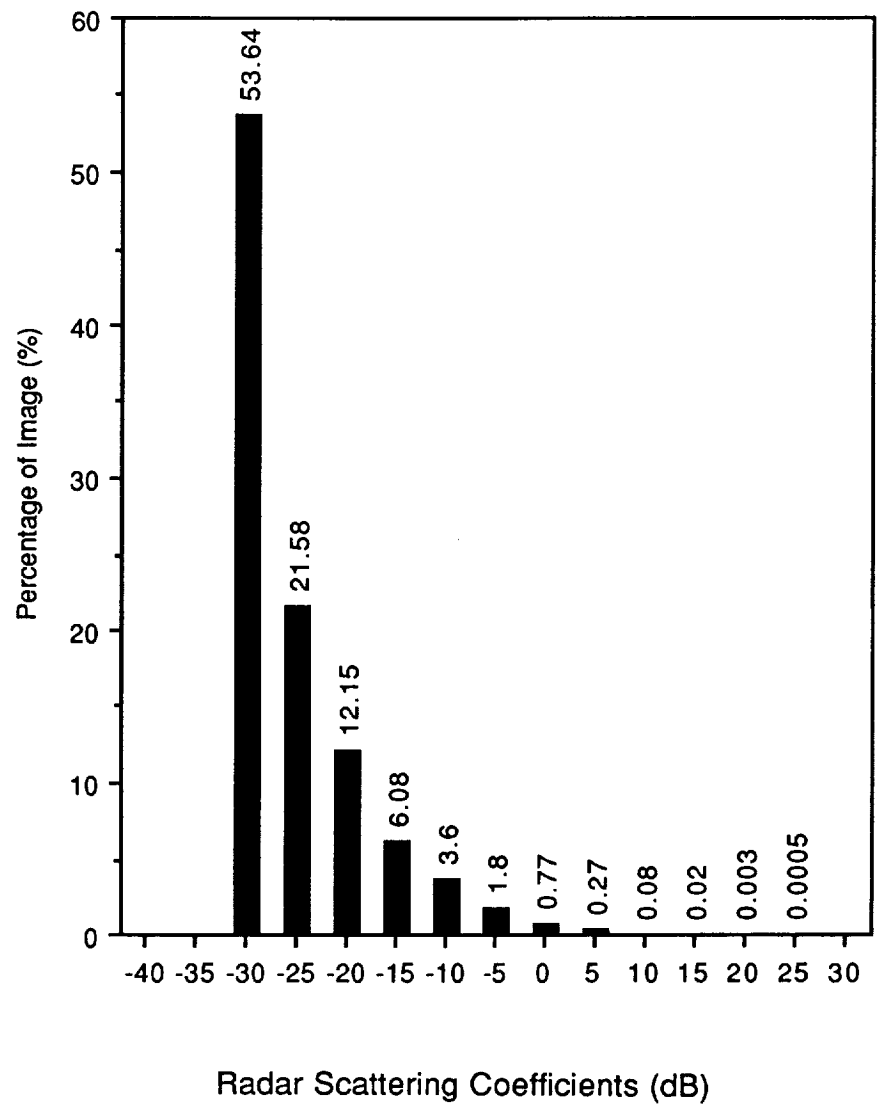


Figure 6. Histogram of Radar Scattering Coefficients for the Philadelphia Image



Figure 7. Philadelphia SAR Image Thresholded at -30 dB



Figure 8. Philadelphia SAR Image Thresholded at -20 dB

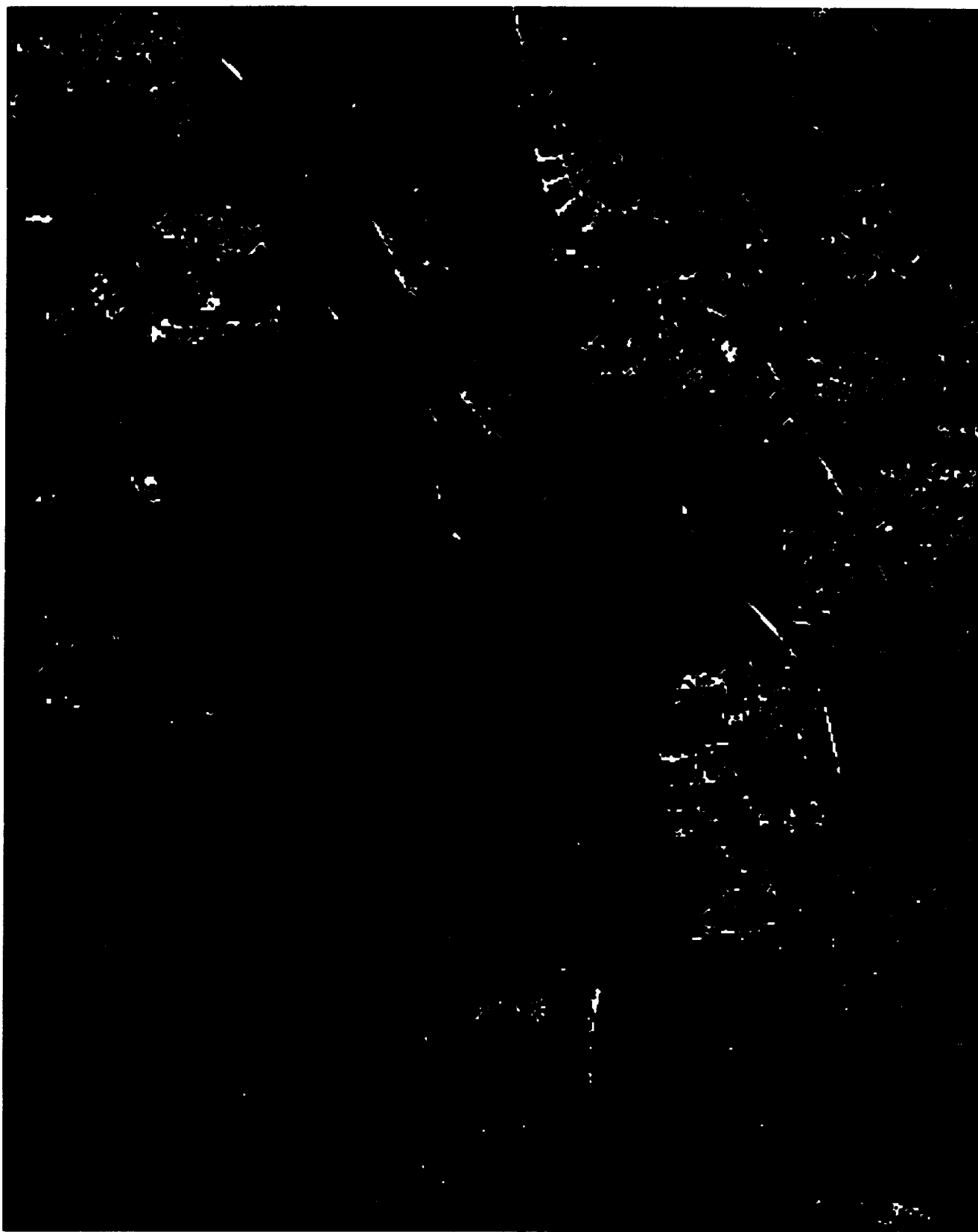


Figure 9. Philadelphia SAR Image Thresholded at -10 dB

ORIGINAL PAGE
BLACK AND WHITE PHOTOGRAPH

ORIGINAL PAGE IS
OF POOR QUALITY



Figure 10. Philadelphia SAR Image Thresholded at 0 dB

ORIGINAL PAGE
BLACK AND WHITE PHOTOGRAPH

ORIGINAL PAGE IS
OF POOR QUALITY

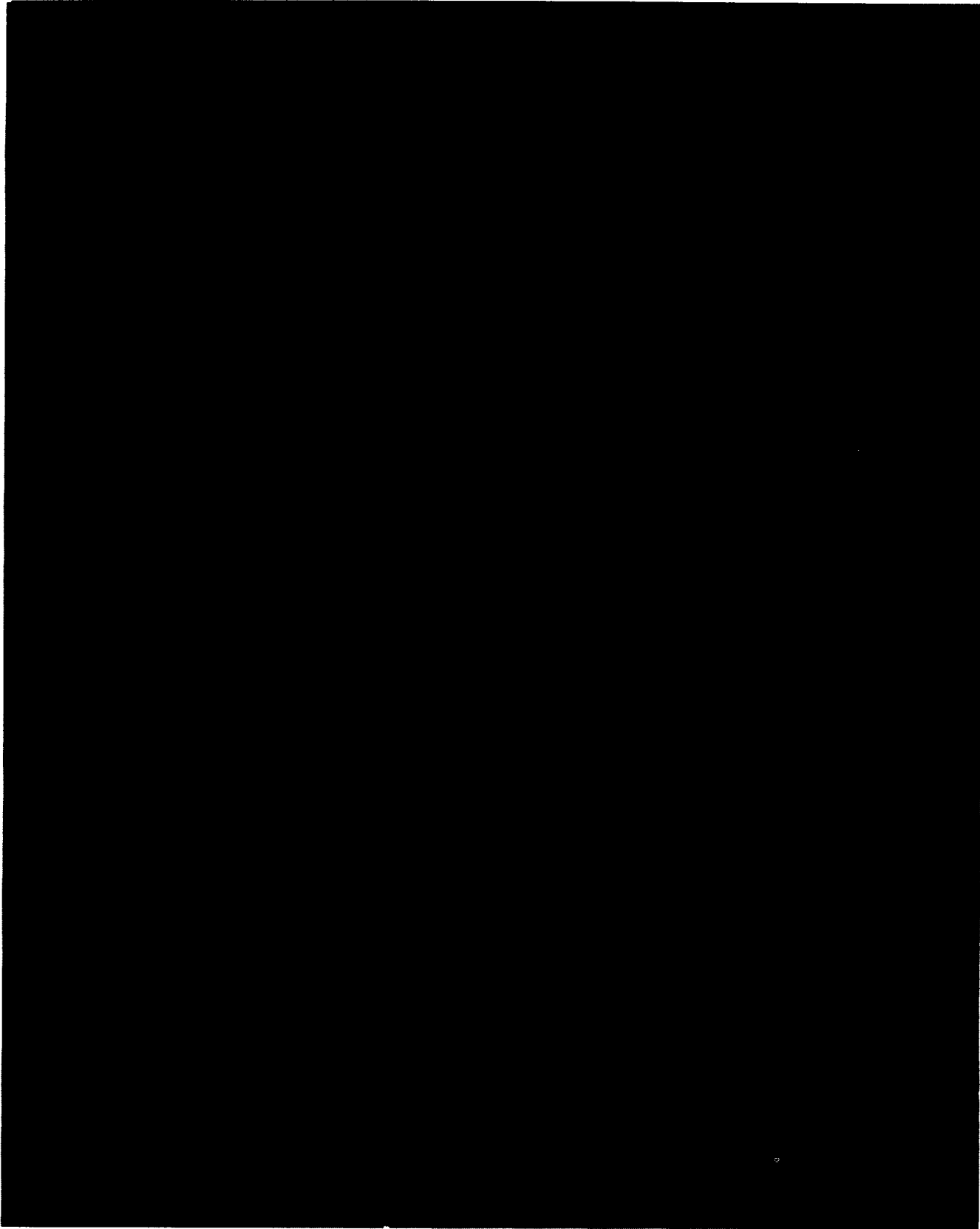
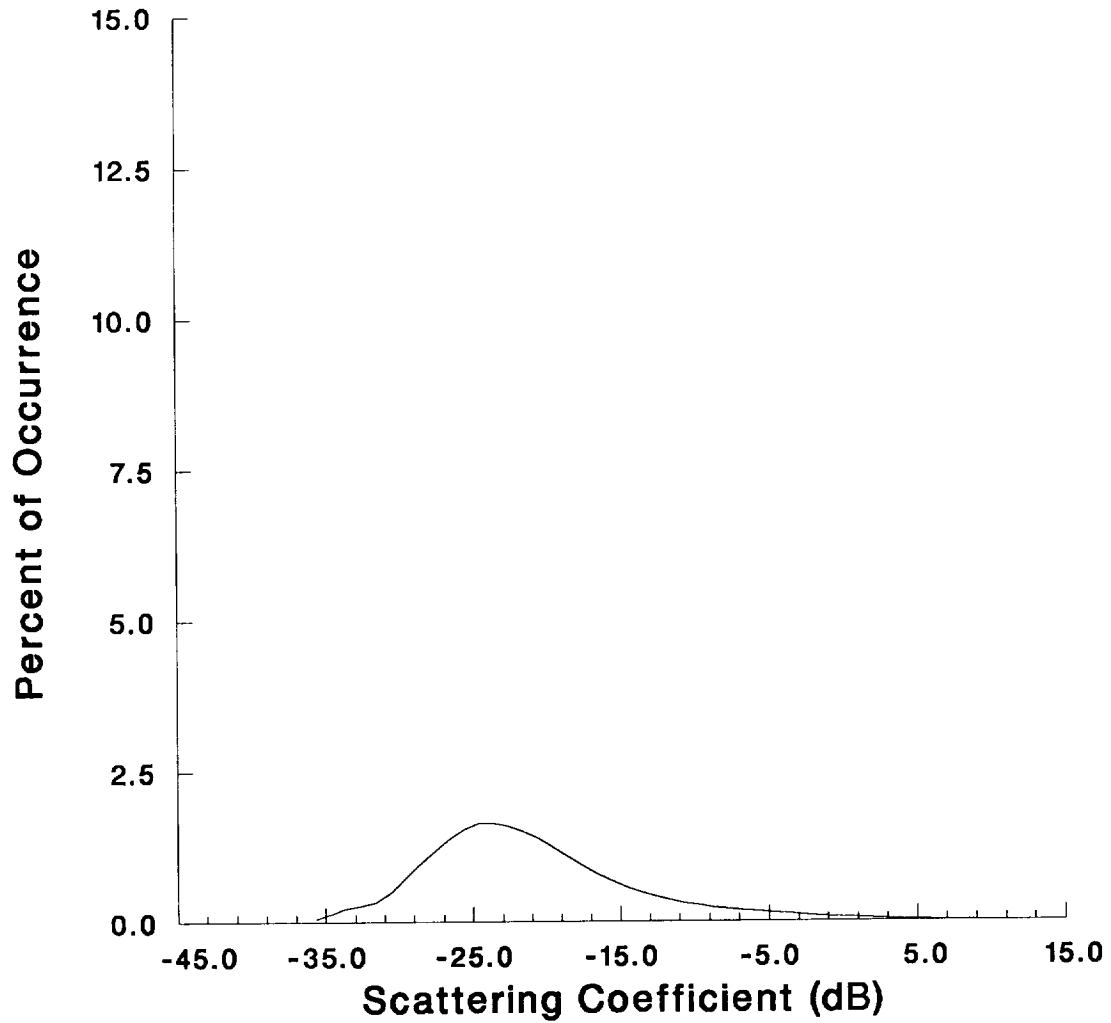


Figure 11. Philadelphia SAR Image Thresholded at 10 dB

P3T586



Minimum: -36.17
Maximum: 33.93
Mean: -15.03
Bin Width: 1.00
Number of Bins: 71

Figure 12. Distribution of Radar Scattering Cross Sections in the Philadelphia SAR Image

Residential (40 - 49 degrees)

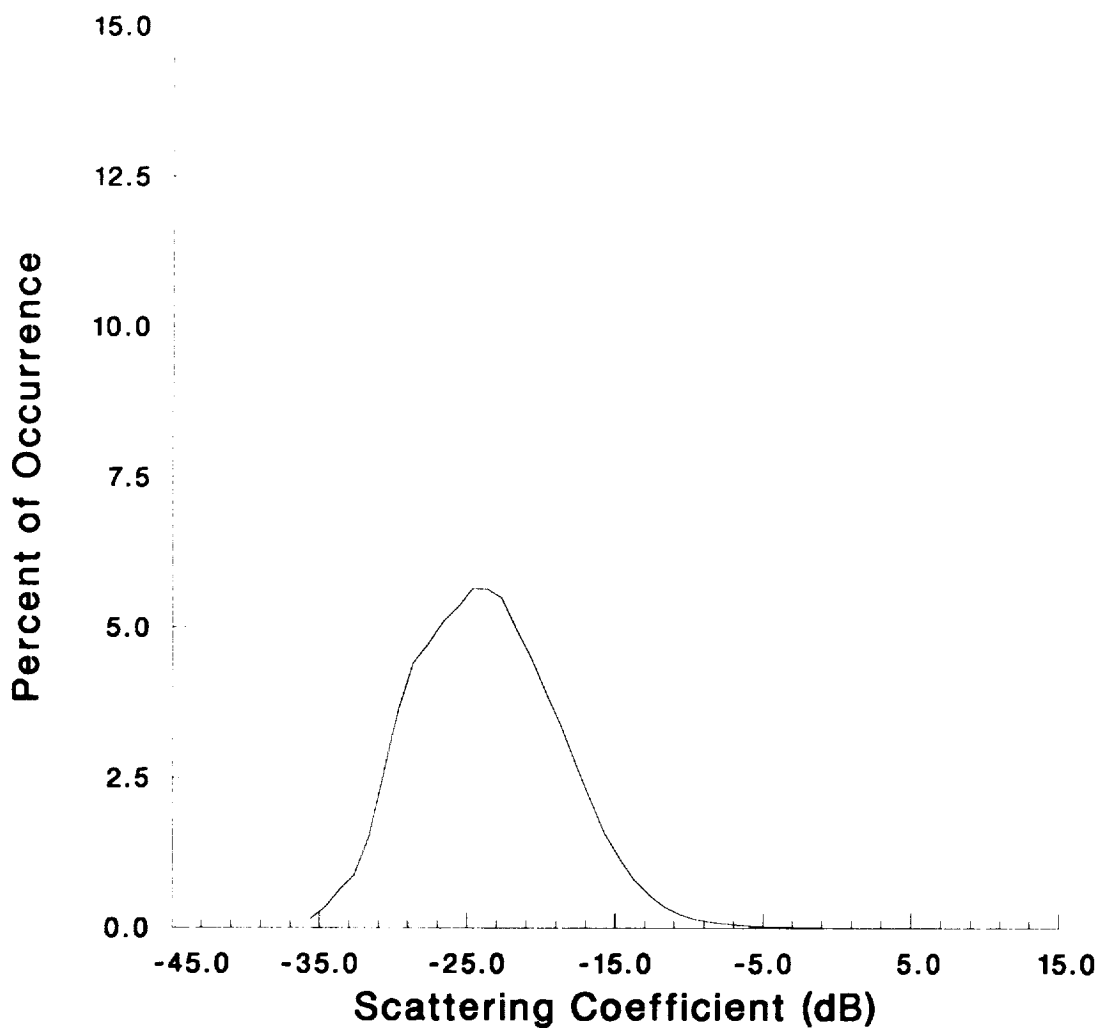


Figure 13.

Minimum: -36.17
Maximum: 12.61
Mean: -21.23
Bin Width: 1.00
Number of Bins: 50

Residential (50 - 59 degrees)

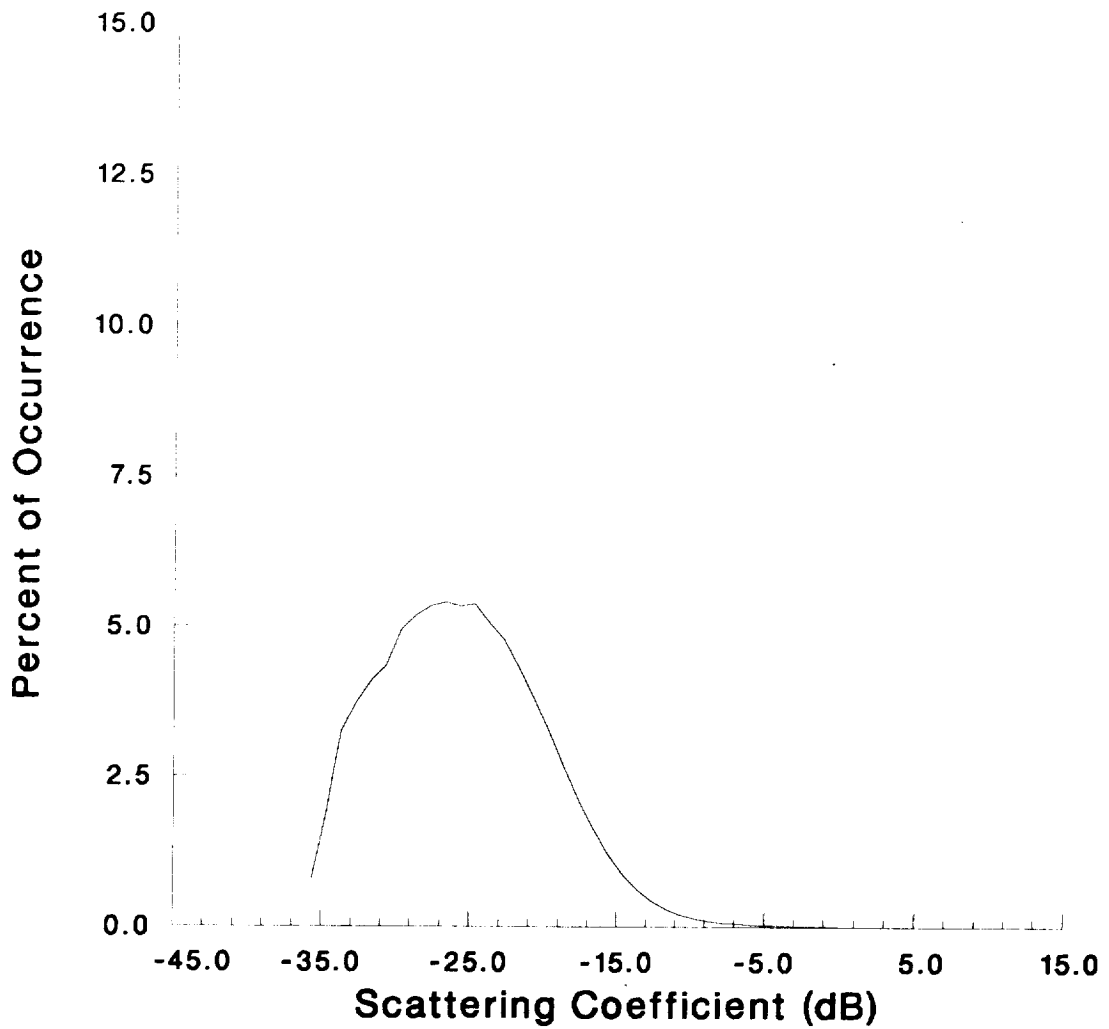


Figure 14.

Minimum: -36.17
Maximum: 14.01
Mean: -20.95
Bin Width: 1.00
Number of Bins: 51

Residential (60 - 64 degrees)

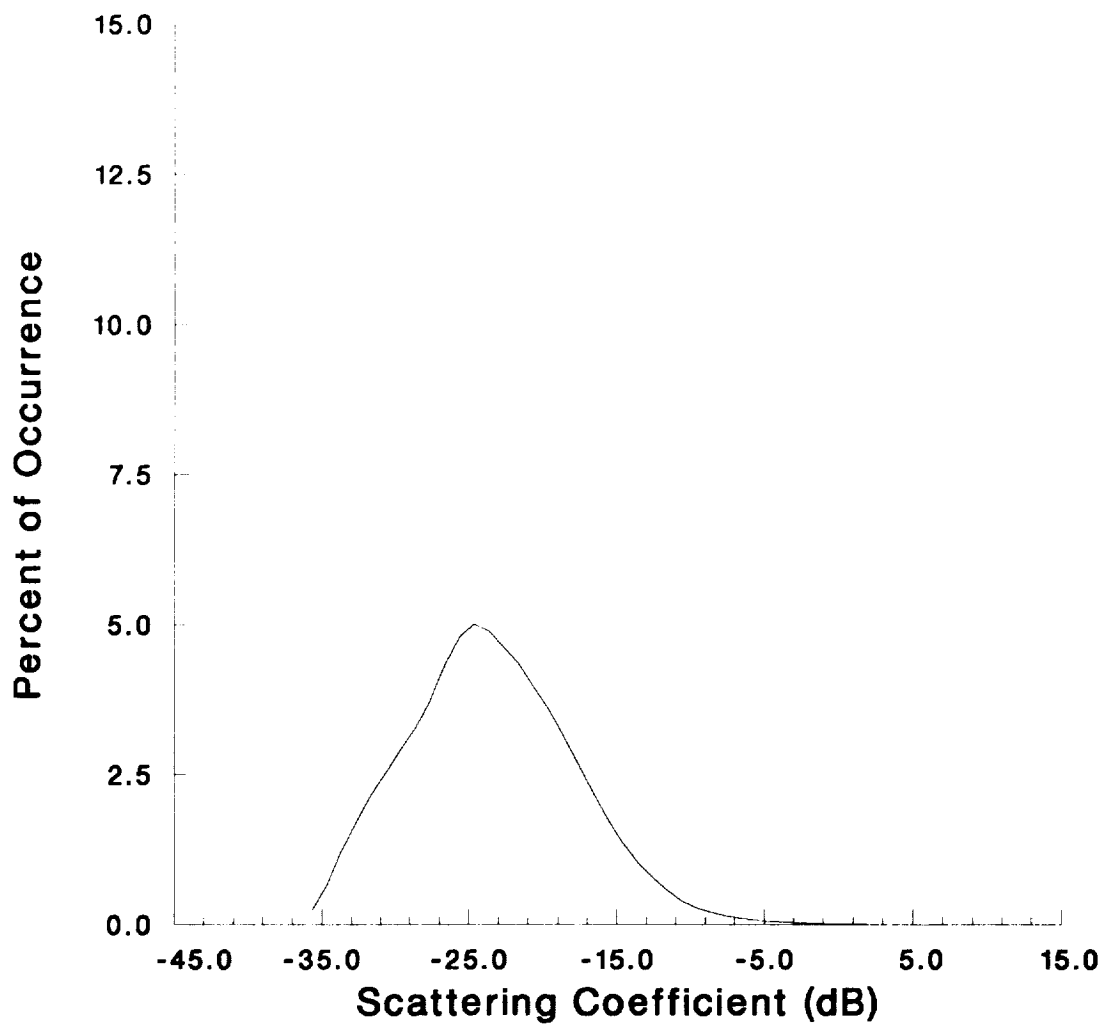


Figure 15.

Minimum: -36.17
Maximum: 15.82
Mean: -19.81
Bin Width: 1.00
Number of Bins: 53

Residential (65 - 69 degrees)

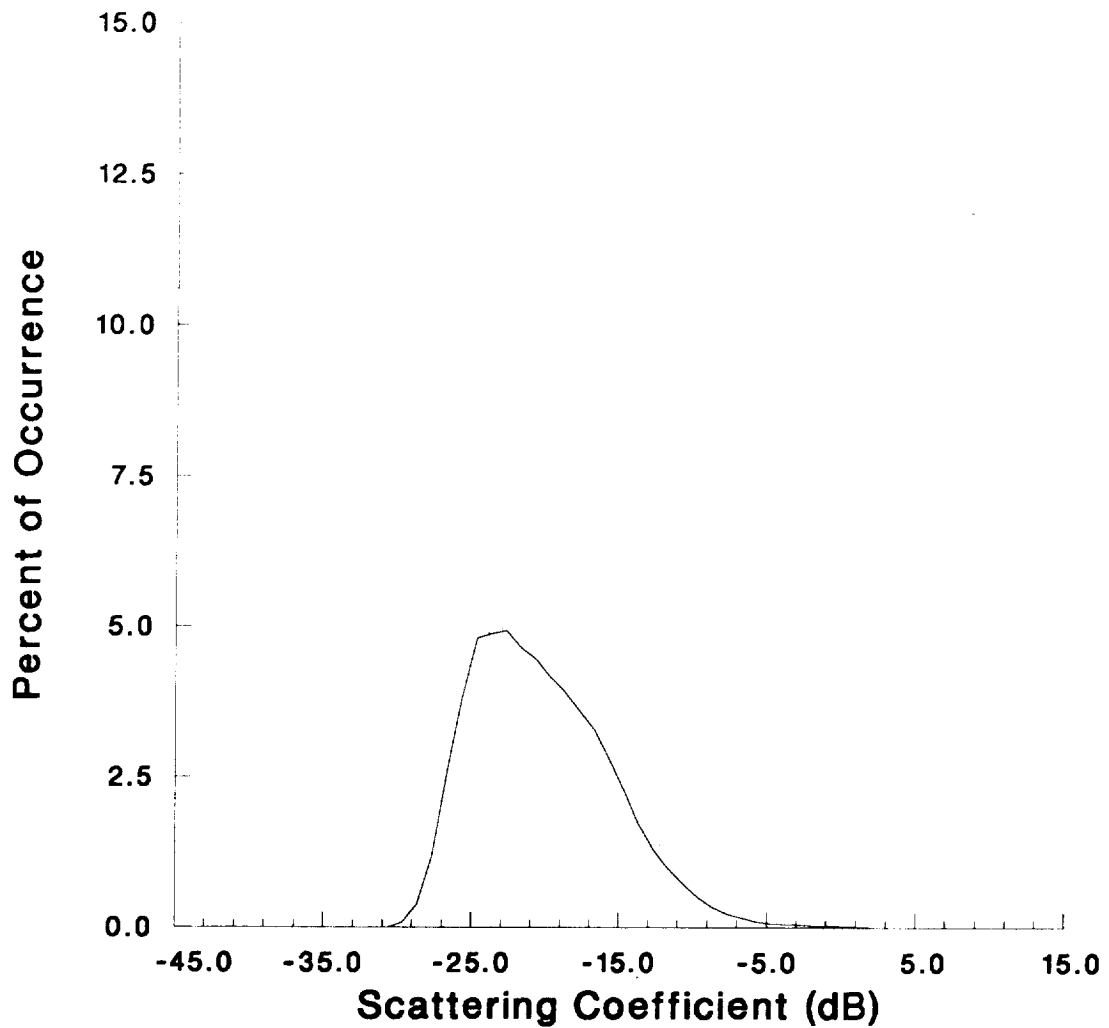


Figure 16.

Minimum: -36.17
Maximum: 7.18
Mean: -18.85
Bin Width: 1.00
Number of Bins: 44

Residential (70 - 74 degrees)

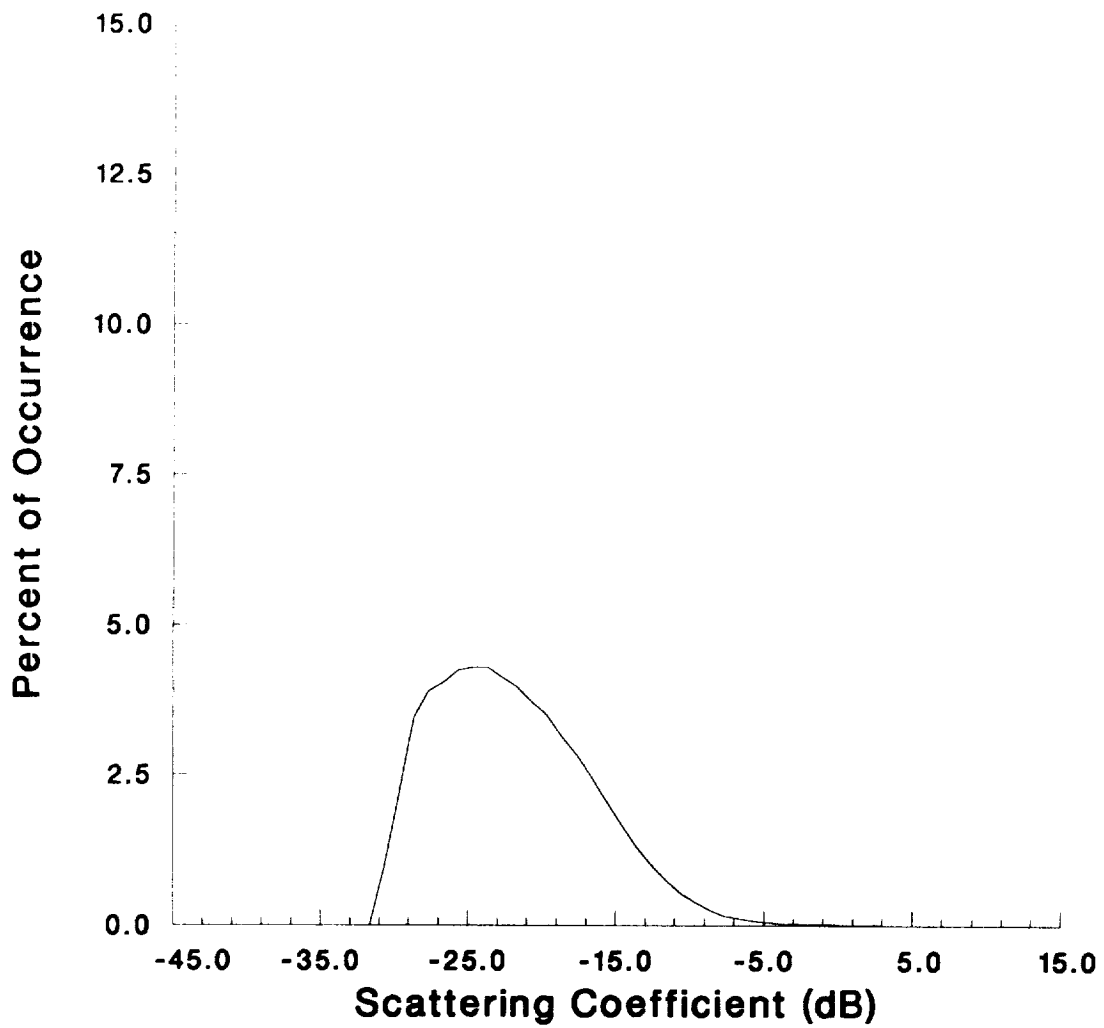


Figure 17.

Minimum: -36.17
Maximum: 13.89
Mean: -19.61
Bin Width: 1.00
Number of Bins: 51

Forest (40 - 49 degrees)

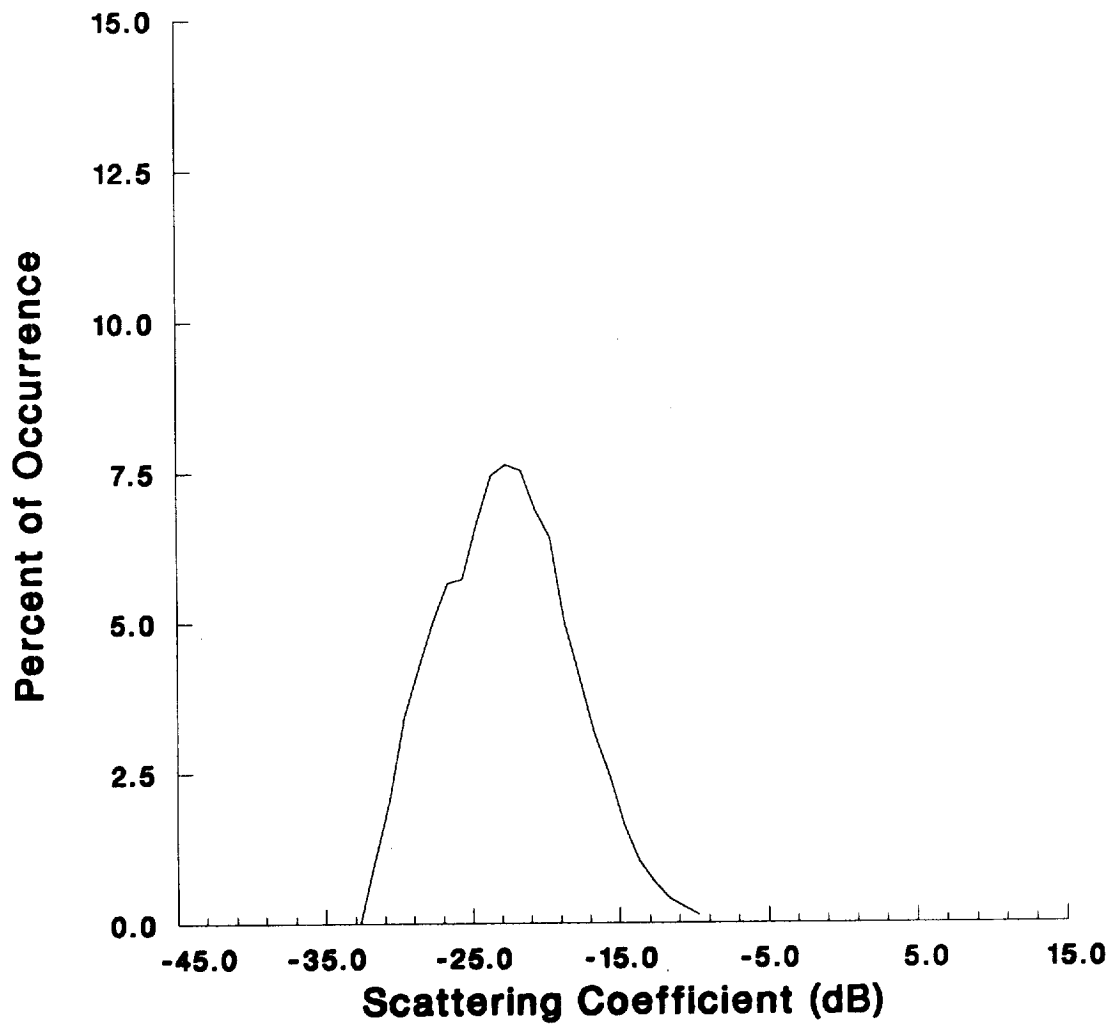


Figure 18.

Minimum: -36.17
Maximum: -9.80
Mean: -21.03
Bin Width: 1.00
Number of Bins: 27

Forest (50 - 59 degrees)

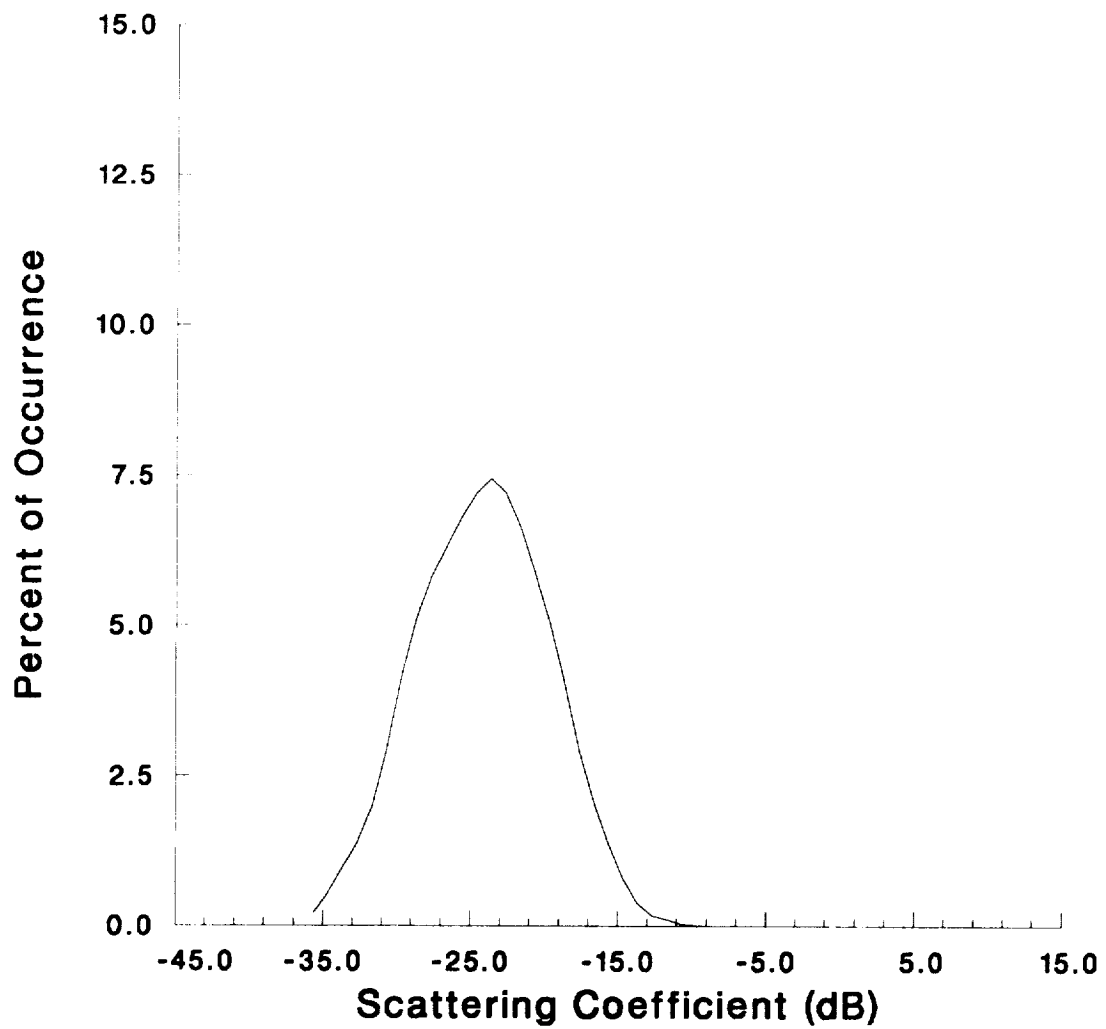


Figure 19.

Minimum: -36.17
Maximum: -8.72
Mean: -22.56
Bin Width: 1.00
Number of Bins: 28

Forest (60 - 64 degrees)

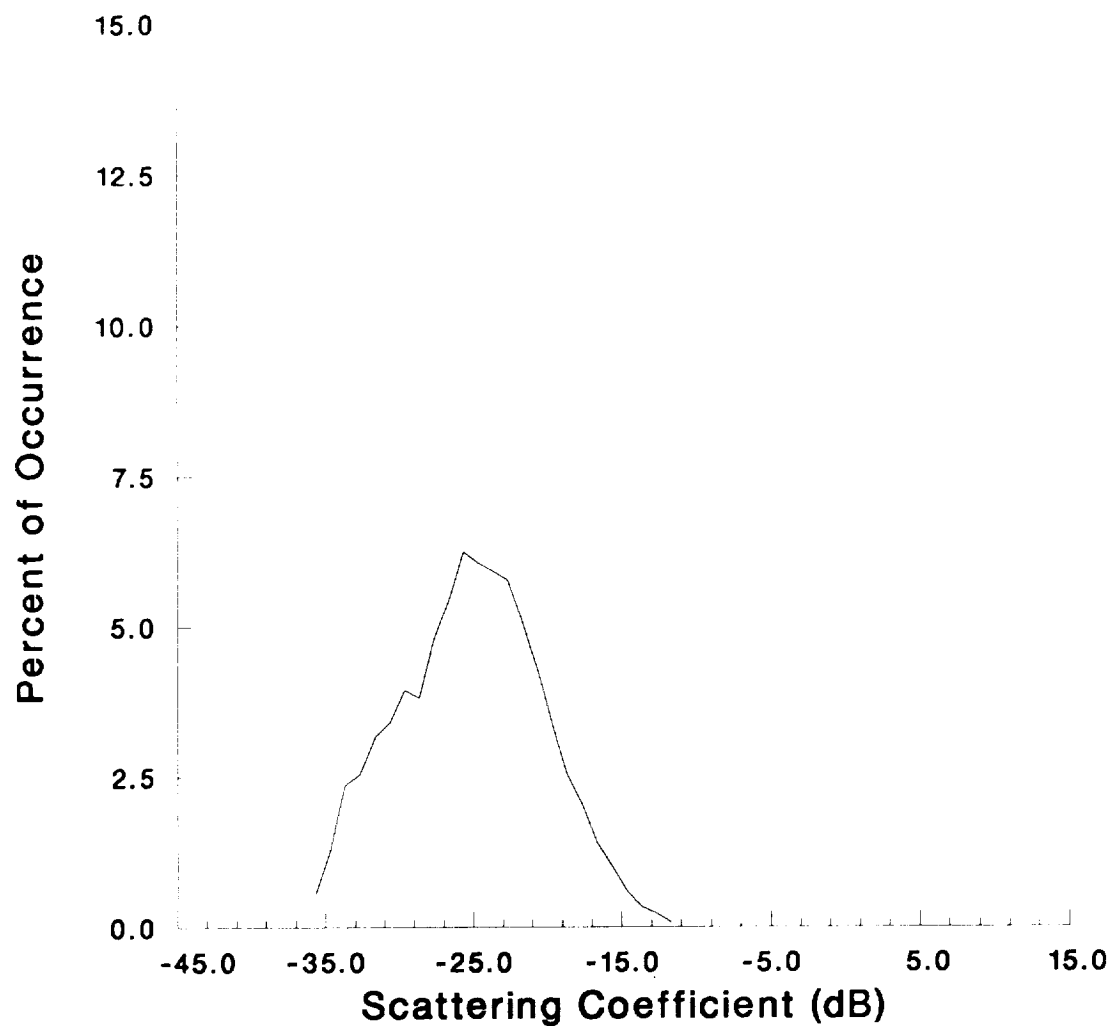


Figure 20.

Minimum: -36.17
Maximum: -12.06
Mean: -23.77
Bin Width: 1.00
Number of Bins: 25

Forest (65 - 69 degrees)

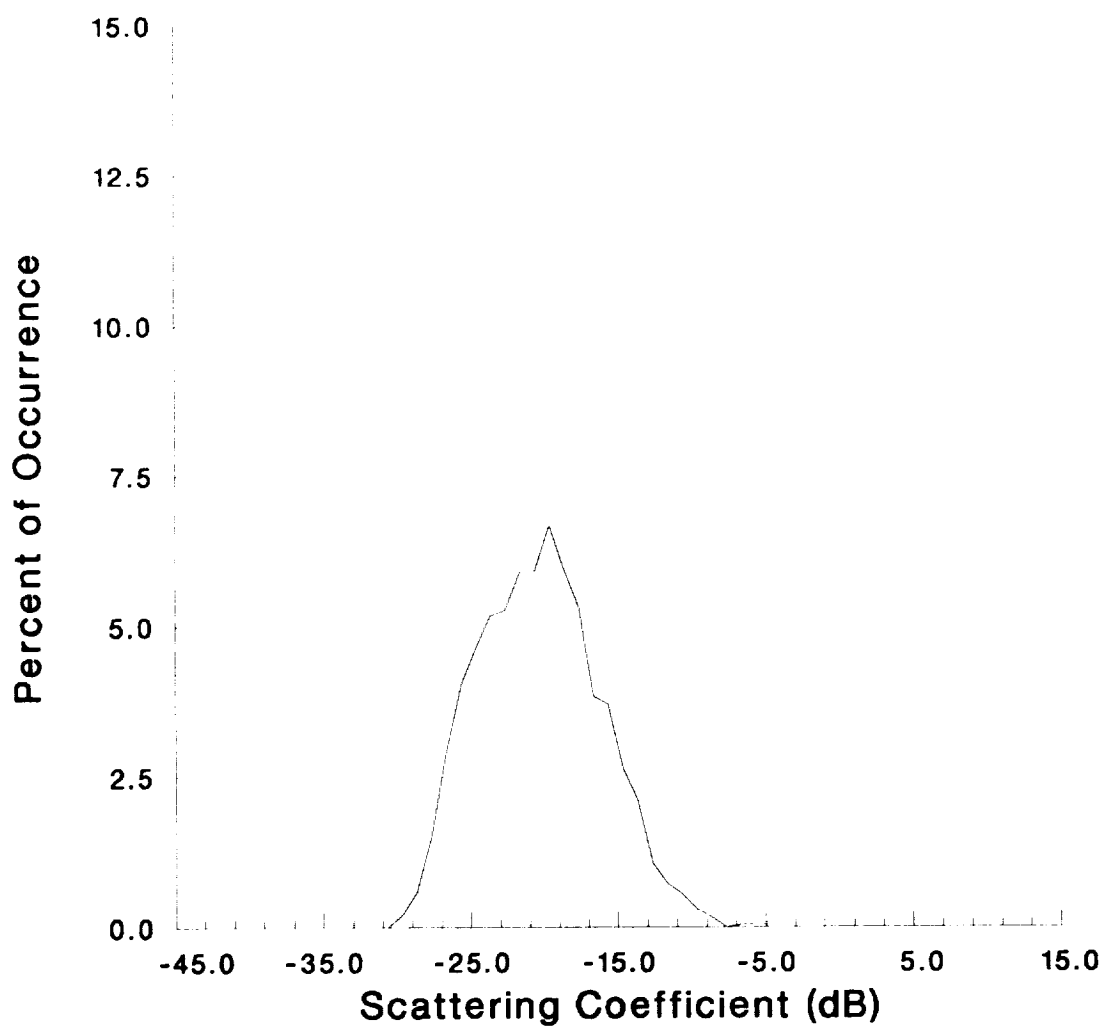


Figure 21.

Minimum: -36.17
Maximum: -5.64
Mean: -19.93
Bin Width: 1.00
Number of Bins: 32

Forest (70 - 74 degrees)

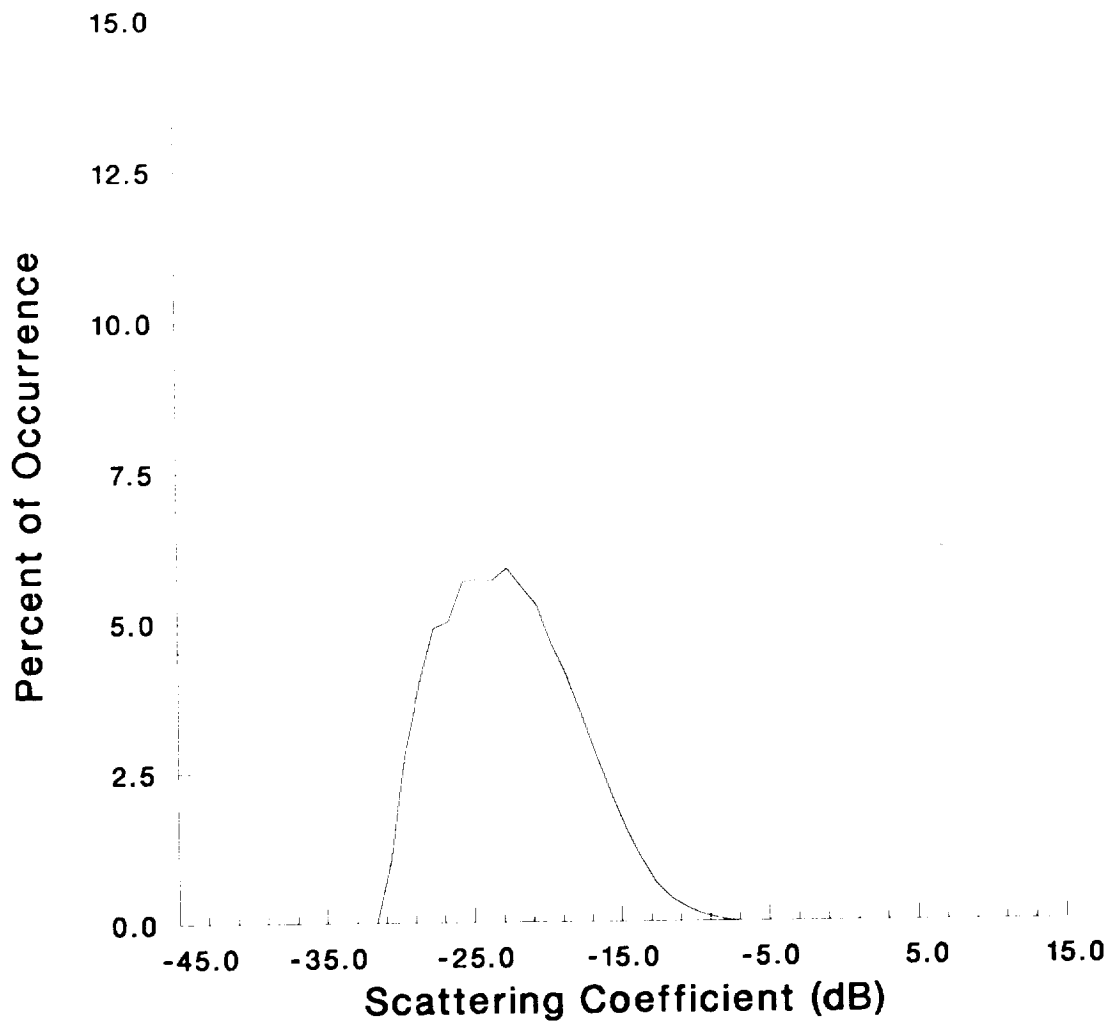


Figure 22.

Minimum: -36.17
Maximum: -6.16
Mean: -21.61
Bin Width: 1.00
Number of Bins: 31

Forest (75 - 79 degrees)

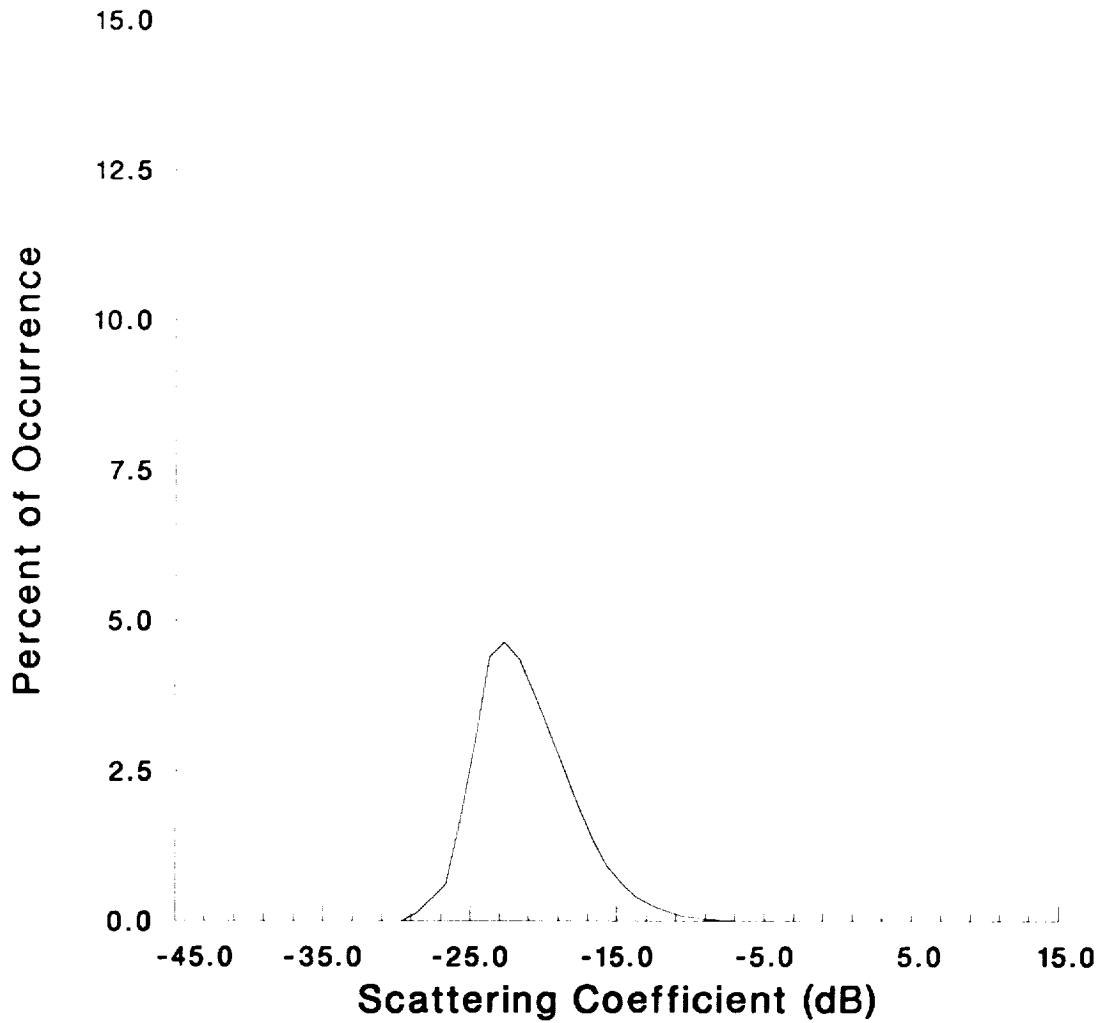


Figure 23.

Minimum: -36.17

Maximum: -4.42

Mean: -24.25

Bin Width: 1.00

Number of Bins: 33

Grass (40 - 49 degrees)

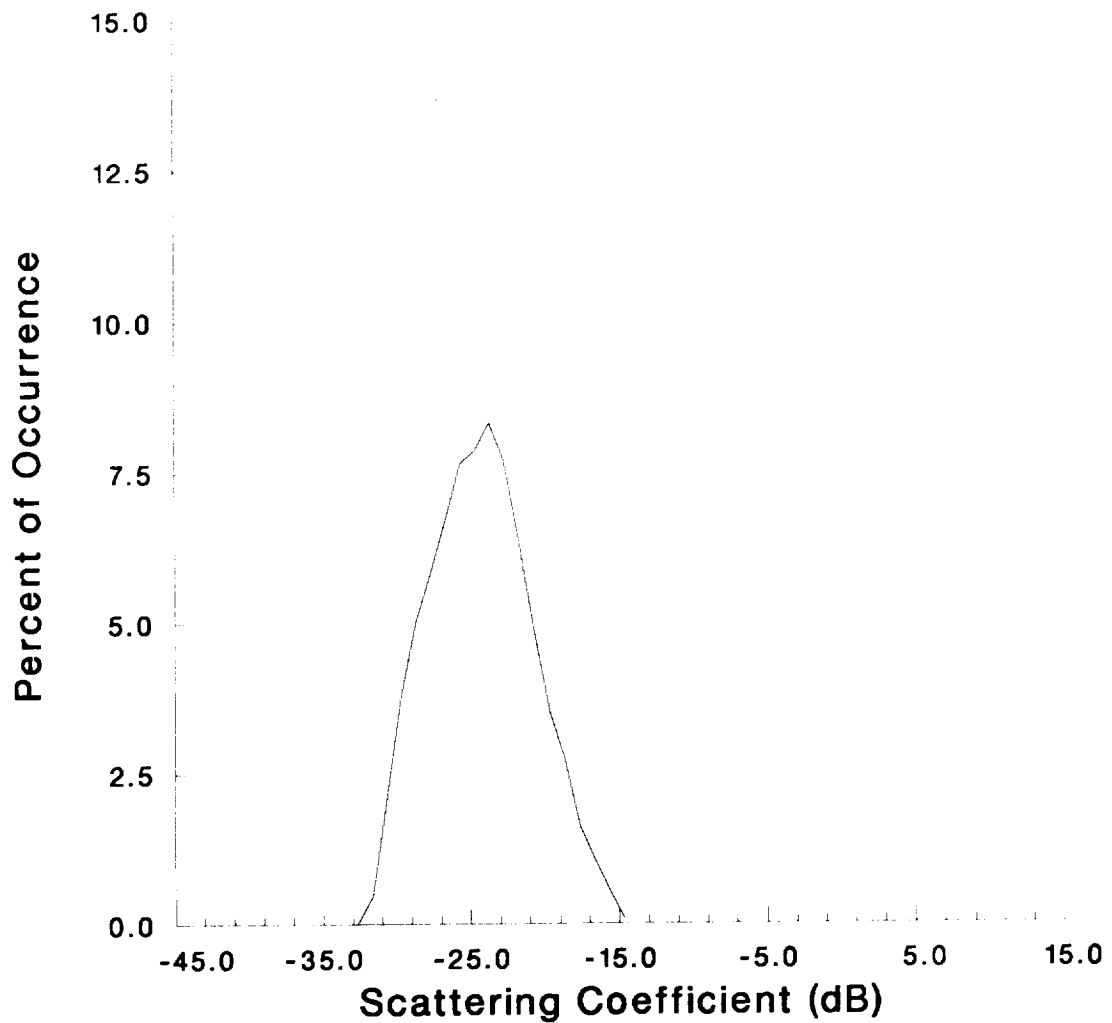


Figure 24.

Minimum: -36.17
Maximum: -15.55
Mean: -24.06
Bin Width: 1.00
Number of Bins: 22

Grass (50 - 59 degrees)

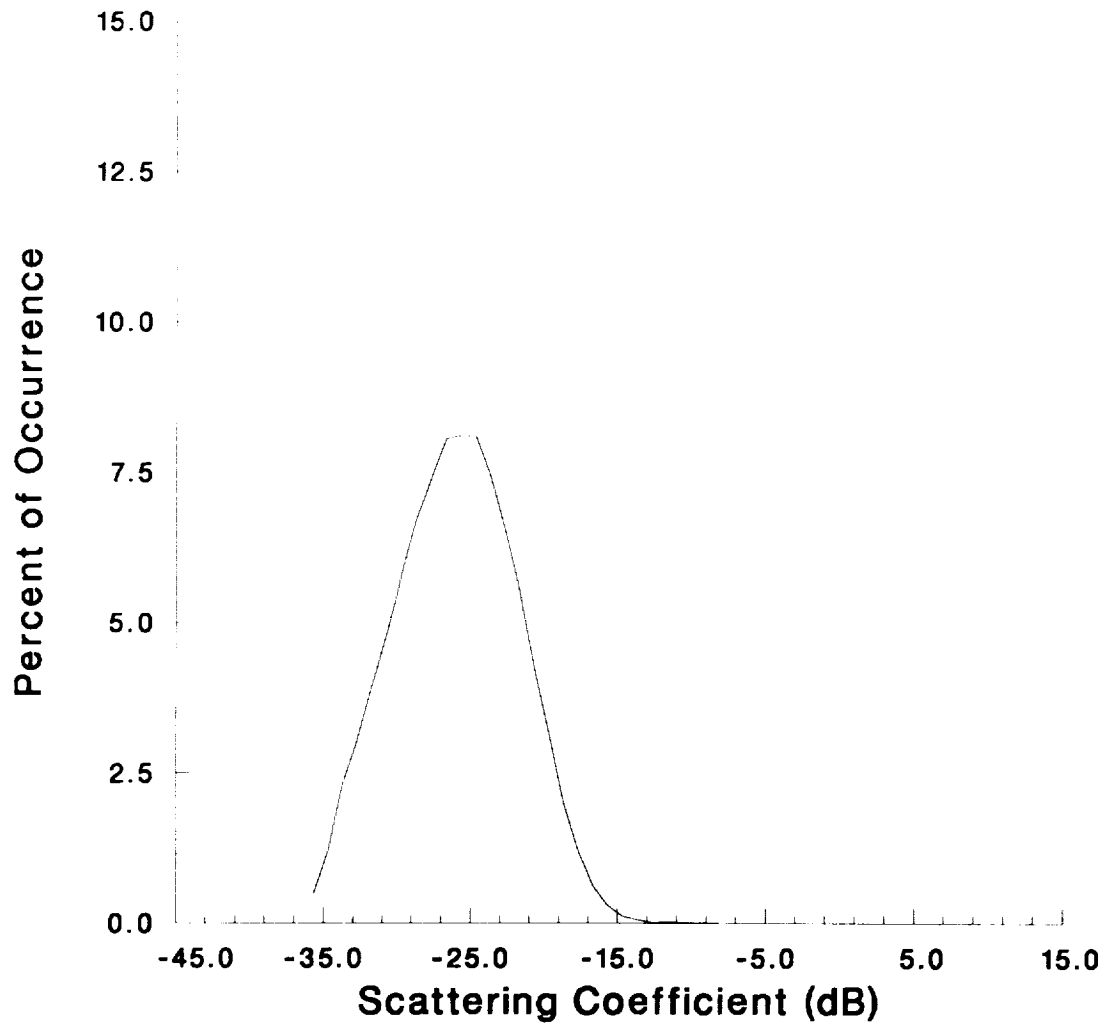


Figure 25.

Minimum: -36.17
Maximum: -6.96
Mean: -24.40
Bin Width: 1.00
Number of Bins: 30

ORIGINAL PAGE IS
OF POOR QUALITY

Grass (60 - 64 degrees)

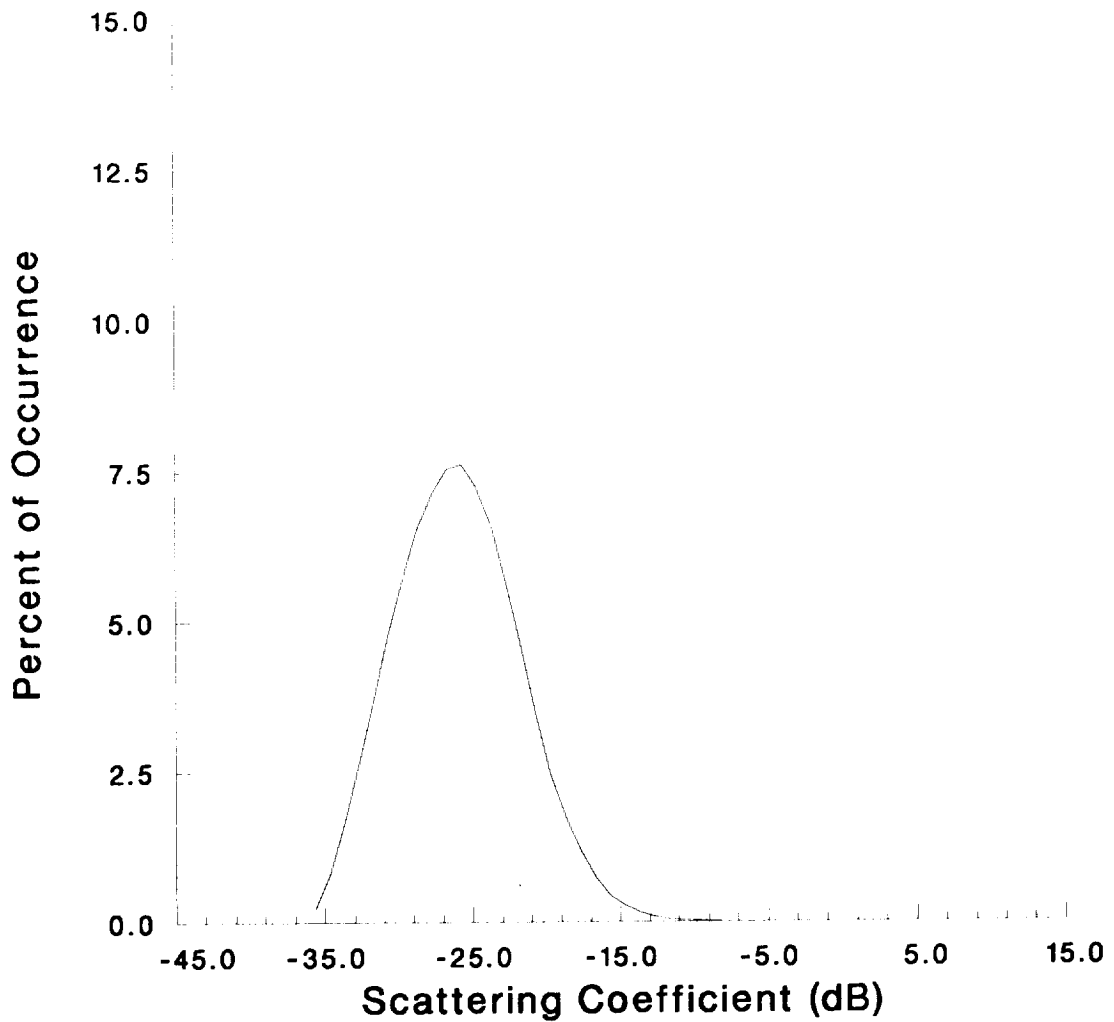


Figure 26.

Minimum: -36.17
Maximum: -5.30
Mean: -24.57
Bin Width: 1.00
Number of Bins: 32

Grass (65 - 69 degrees)

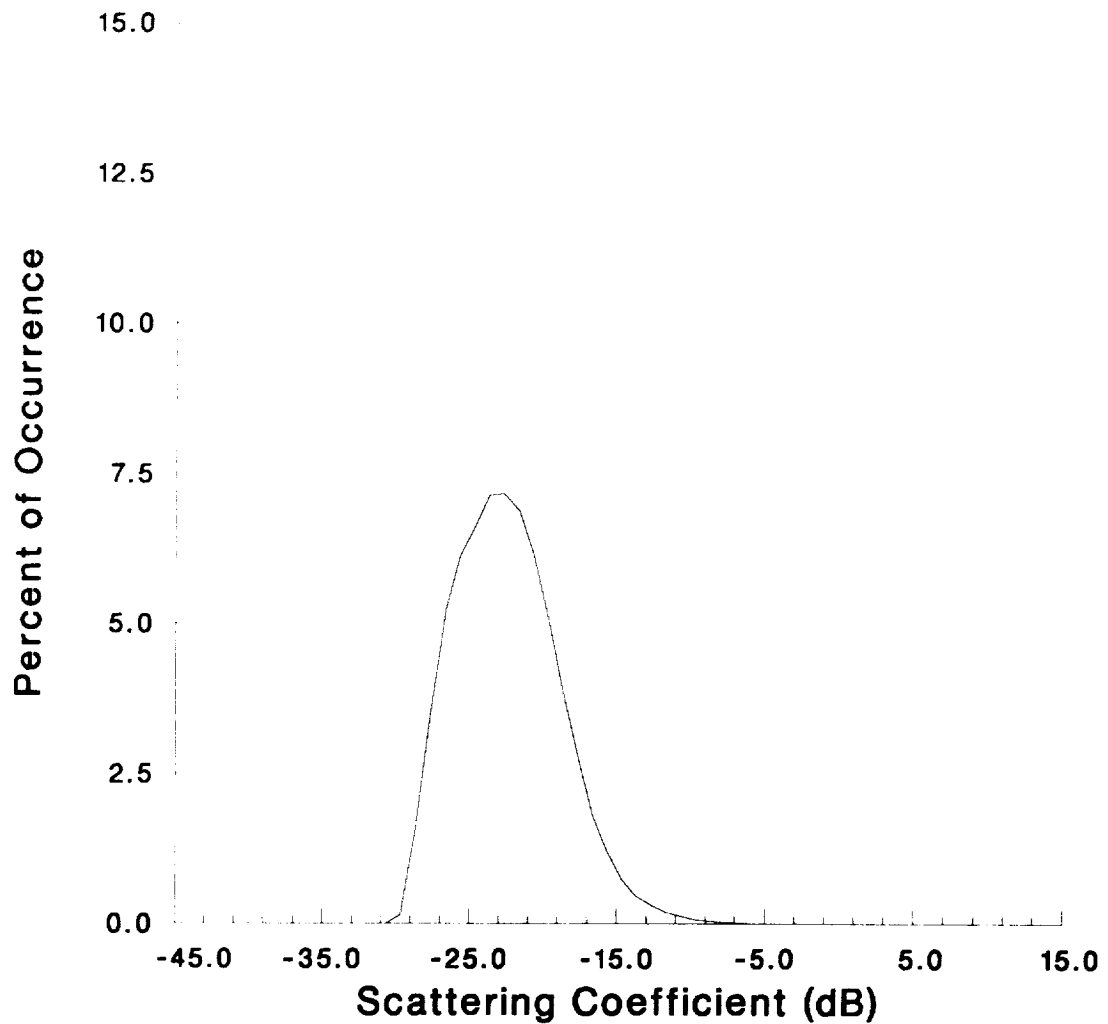


Figure 27.

Minimum: -36.17
Maximum: -0.96
Mean: -22.38
Bin Width: 1.00
Number of Bins: 36

Grass (70 - 74 degrees)

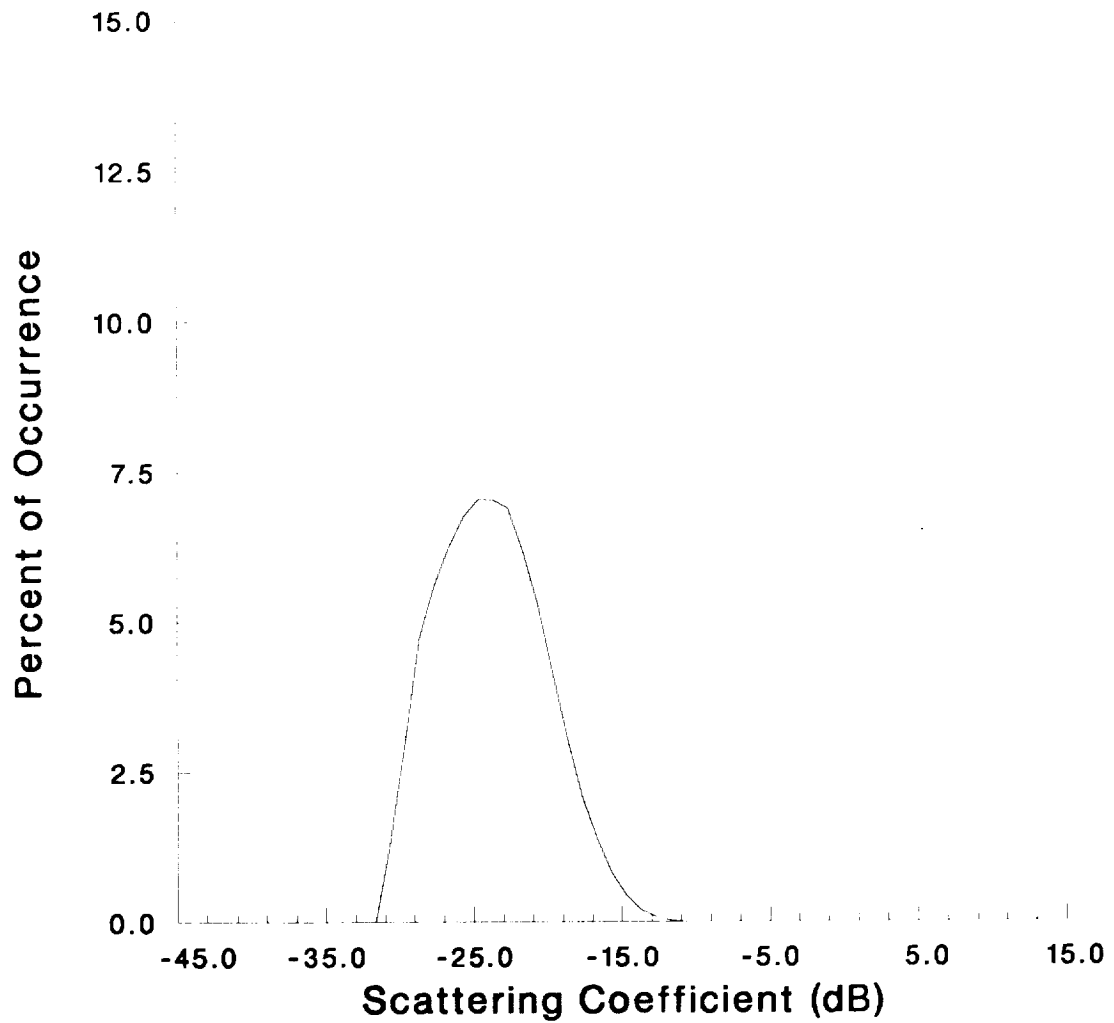


Figure 28.

Minimum: -36.17
Maximum: -10.60
Mean: -23.64
Bin Width: 1.00
Number of Bins: 27

21.00000000
0.00000000

Grass (75 - 79 degrees)

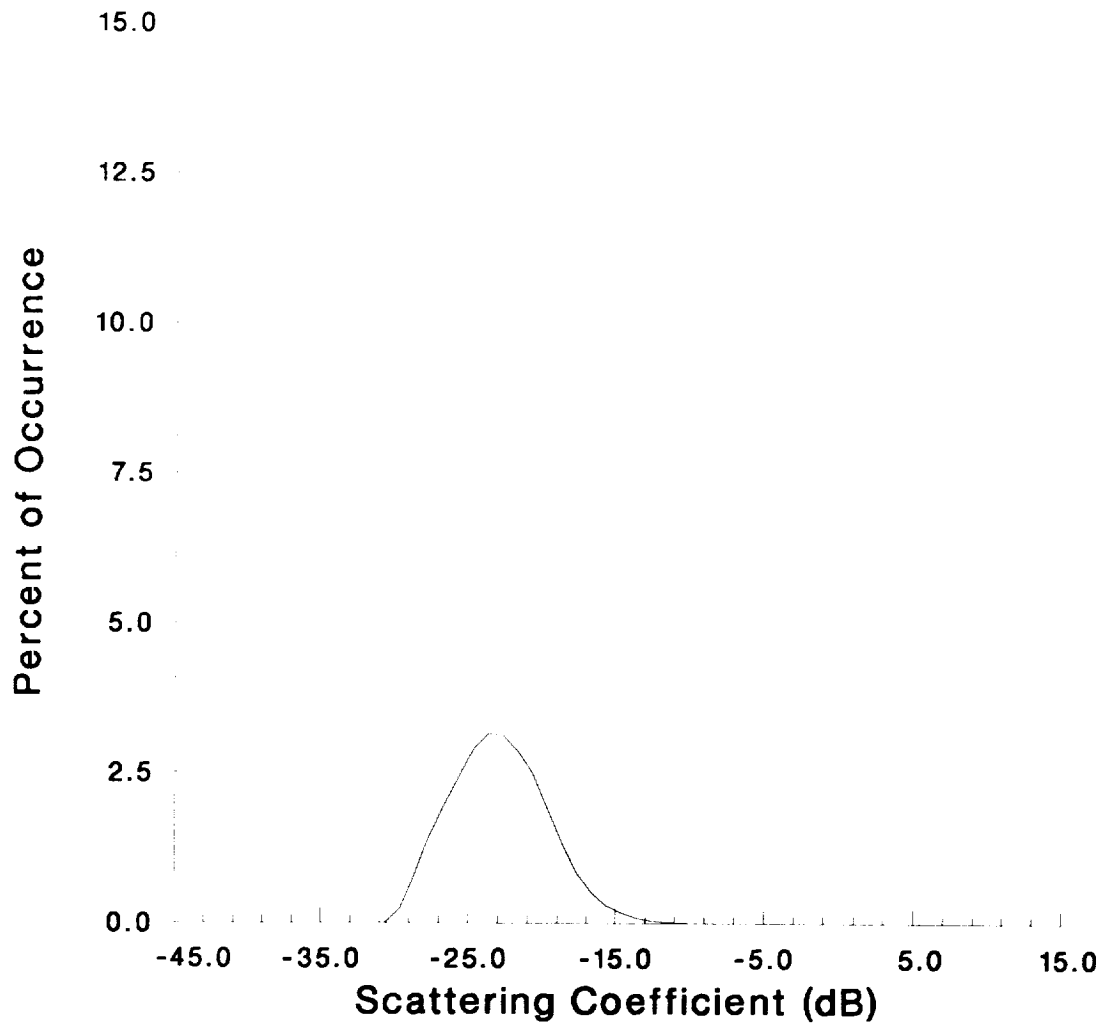


Figure 29.

Minimum: -36.17

Maximum: -7.24

Mean: -27.00

Bin Width: 1.00

Number of Bins: 30

Grass (80 - 84 degrees)

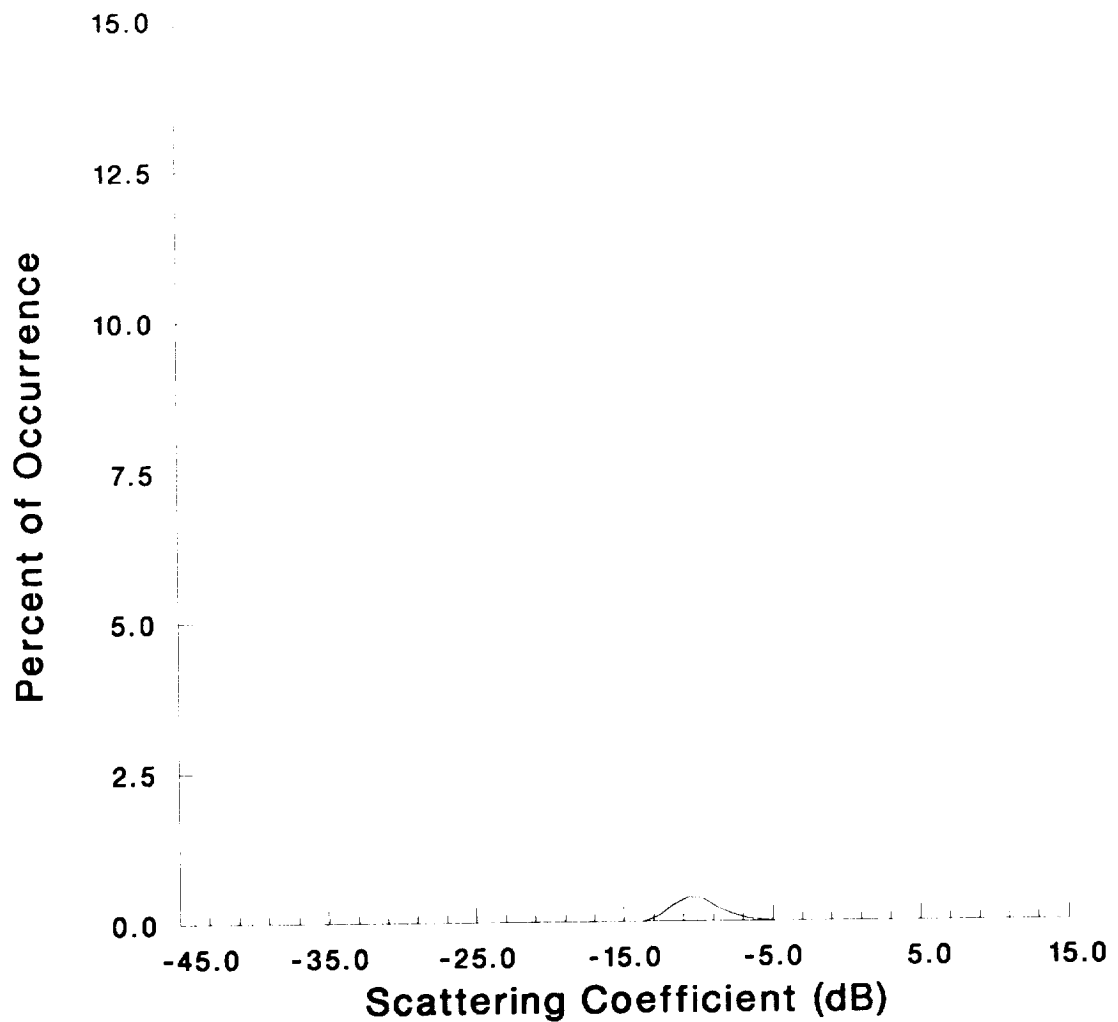


Figure 30.

Minimum: -36.17

Maximum: -5.43

Mean: -27.18

Bin Width: 1.00

Number of Bins: 32

Grass (75 - 79 degrees)

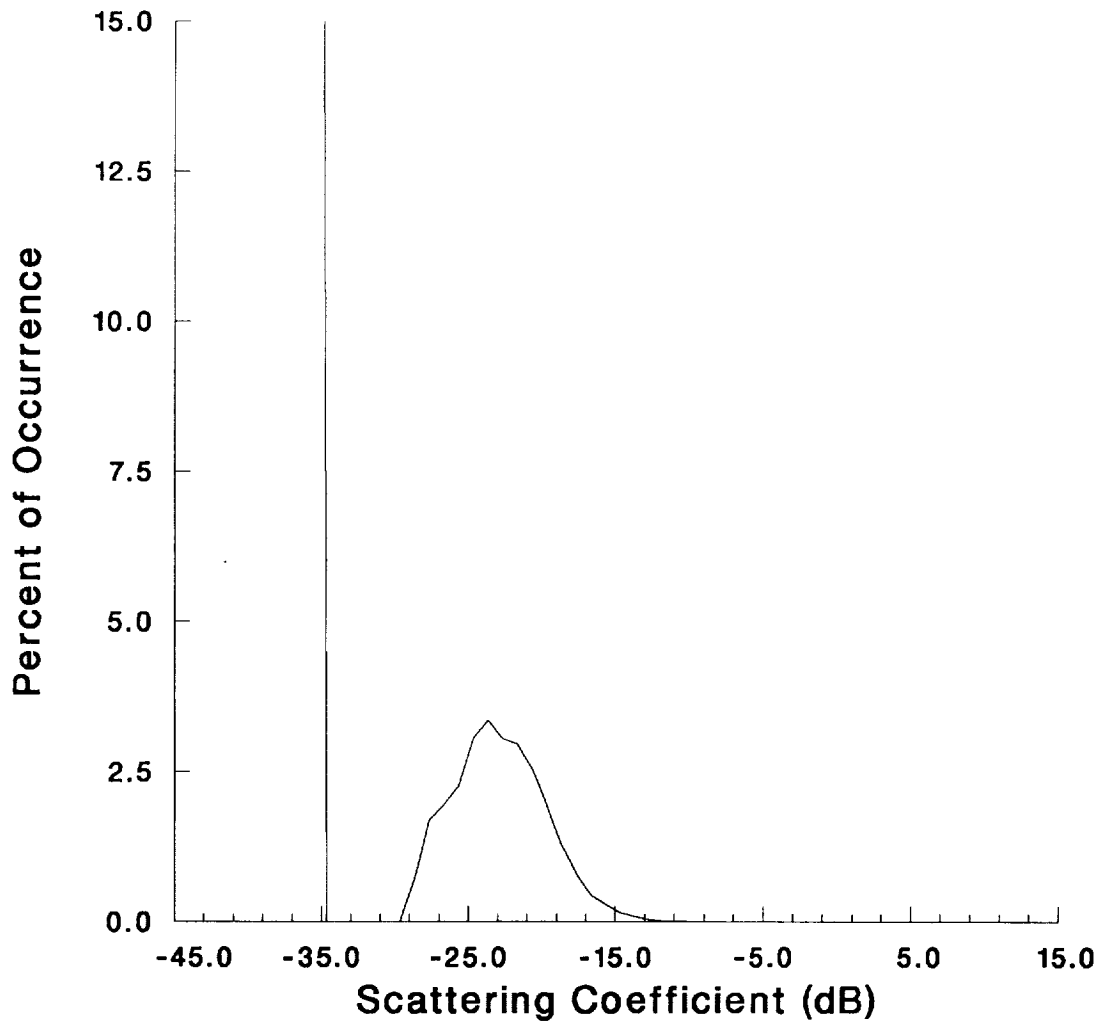


Figure 31.

Minimum: -36.17

Maximum: -7.24

Mean: -27.00

Bin Width: 1.00

Number of Bins: 30

Grass (80 - 84 degrees)

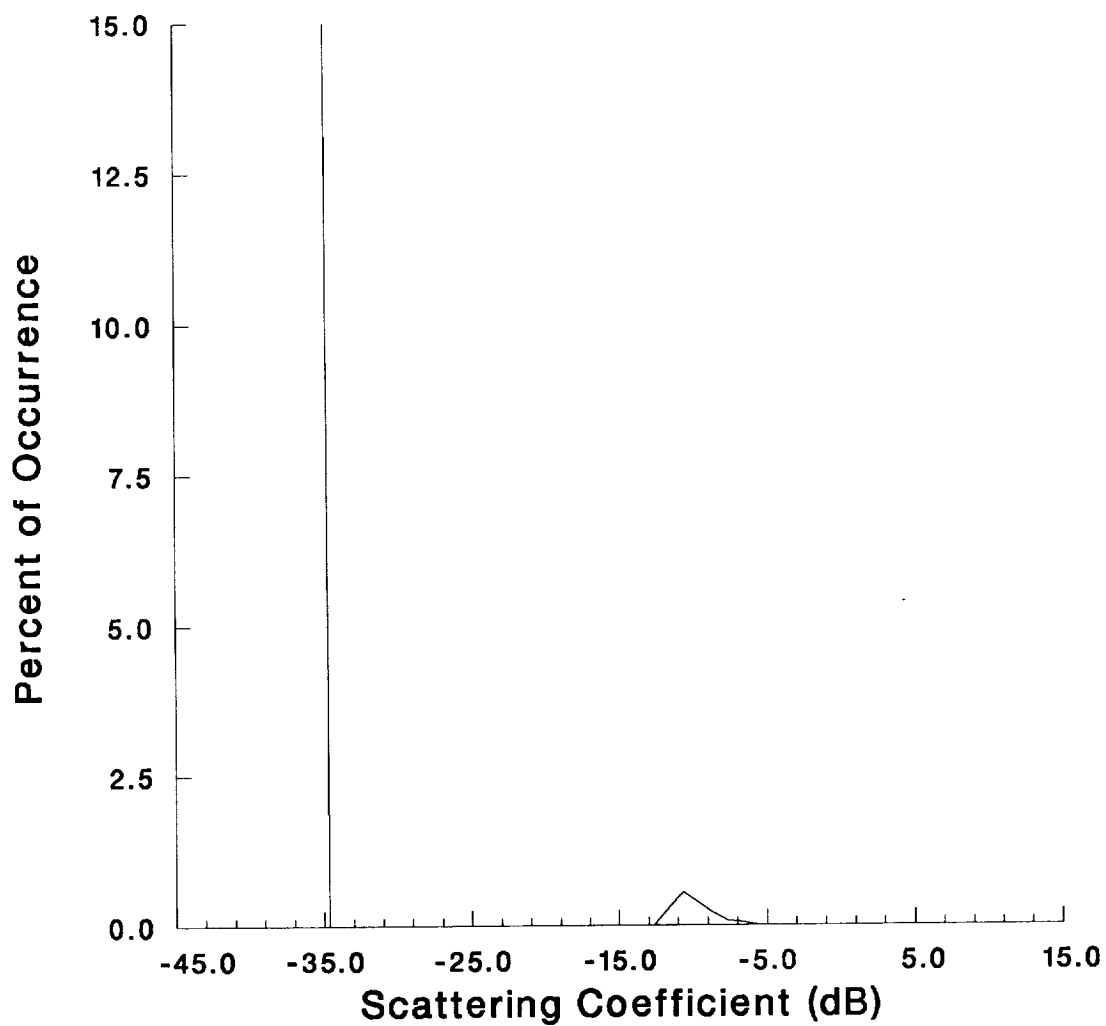


Figure 32.

Minimum: -36.17
Maximum: -5.43
Mean: -27.18
Bin Width: 1.00
Number of Bins: 32

Water (40 - 49 degrees)

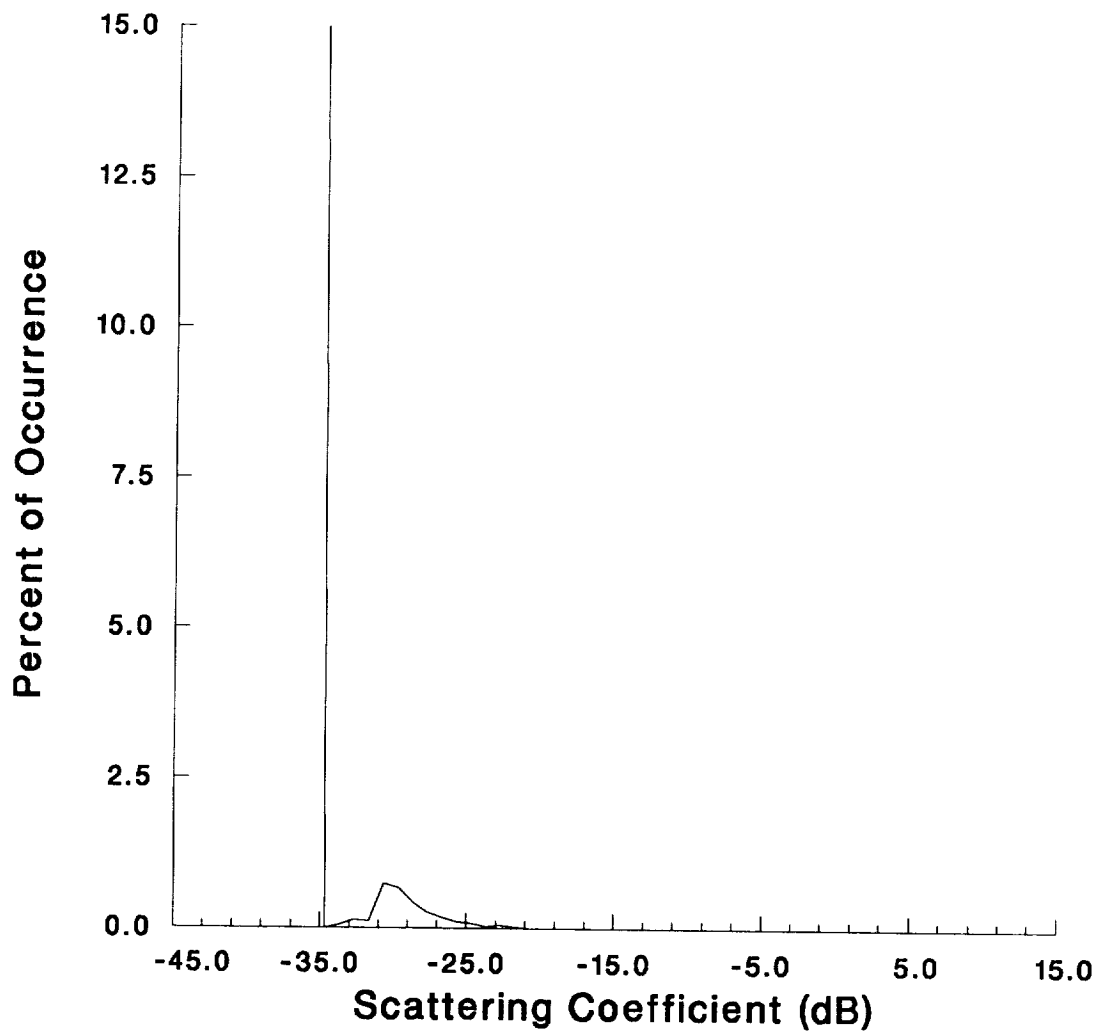


Figure 33.

Minimum: -36.17

Maximum: -12.92

Mean: -35.41

Bin Width: 1.00

Number of Bins: 24

ORIGINAL PAGE IS
OF POOR QUALITY

Water (50 - 59 degrees)

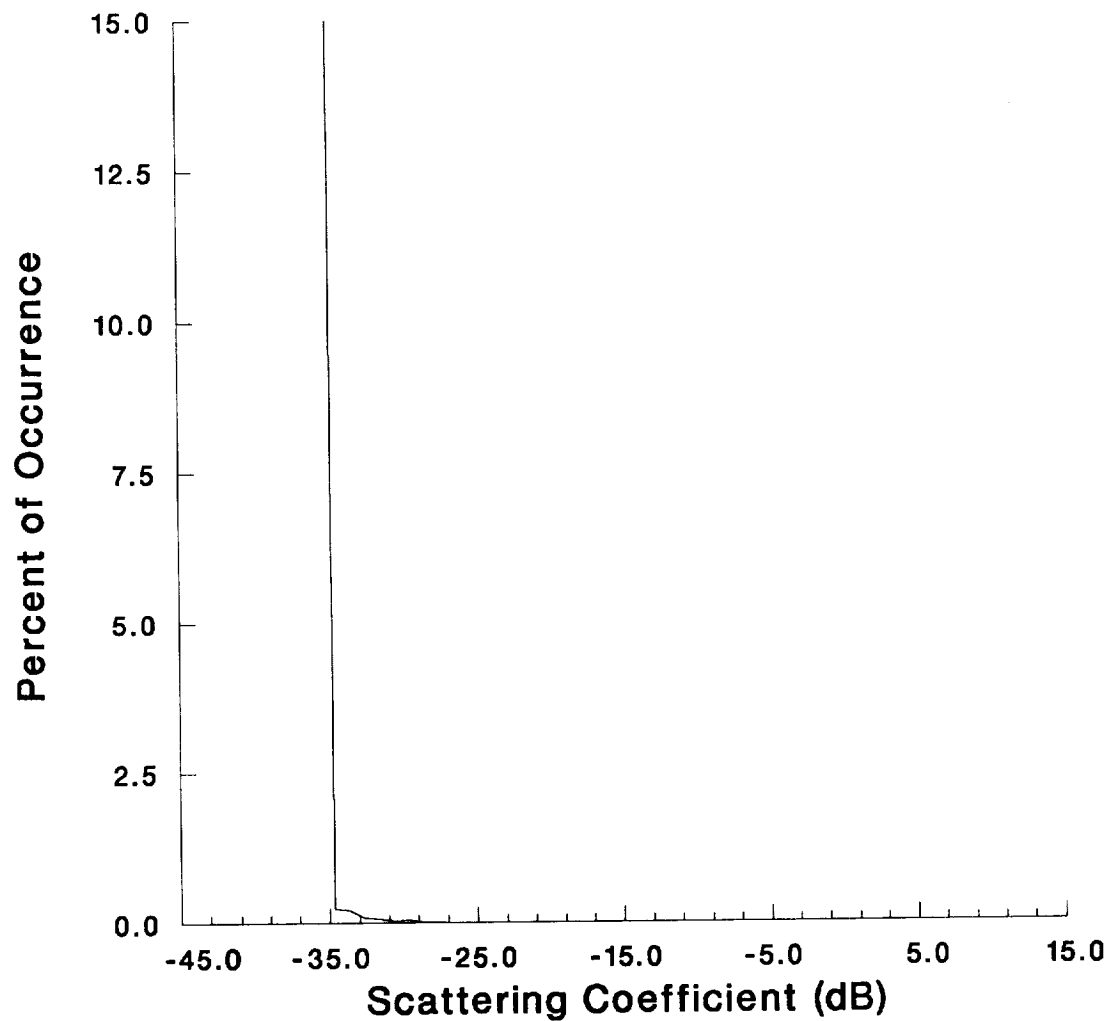


Figure 34.

Minimum: -36.17
Maximum: -26.94
Mean: -36.12
Bin Width: 1.00
Number of Bins: 10

Water (65 - 69 degrees)

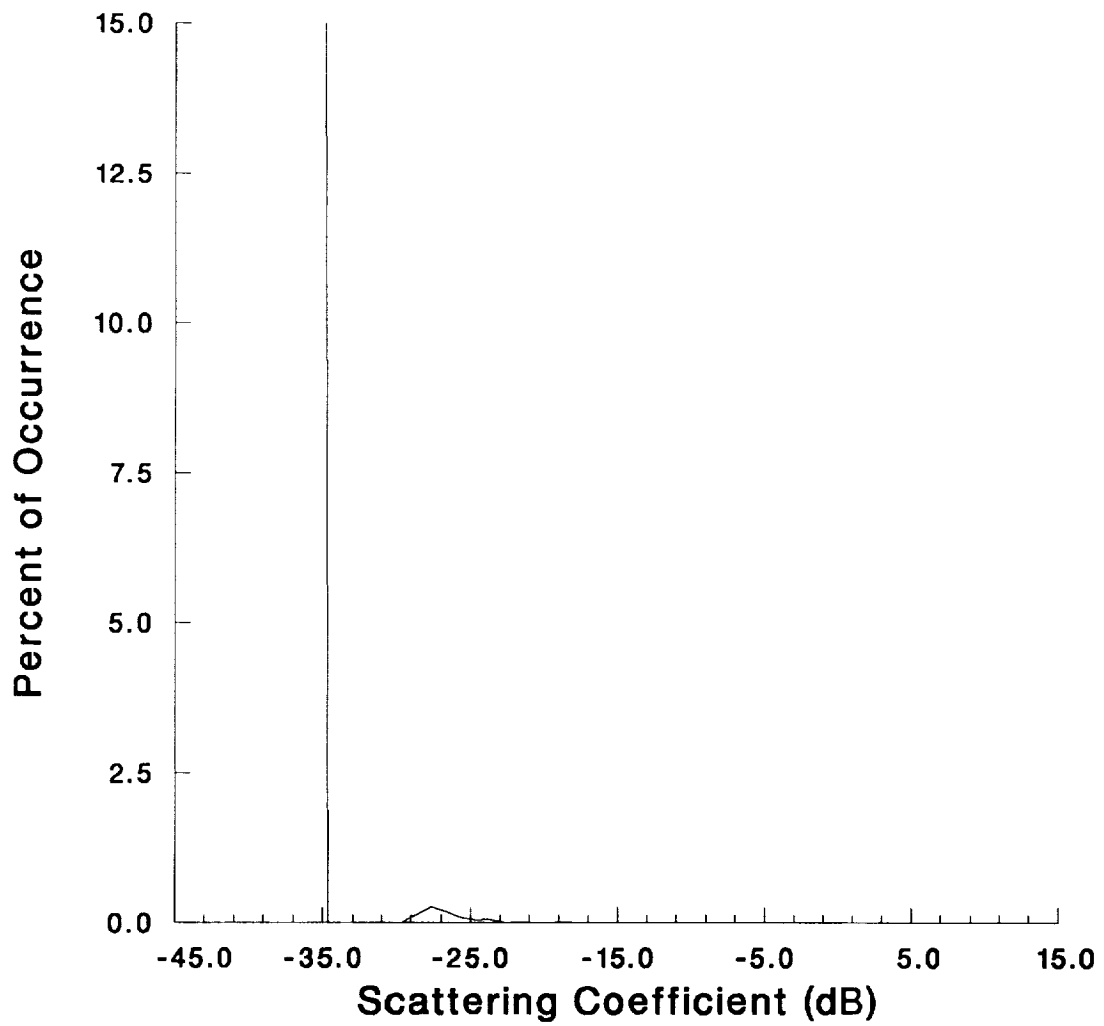


Figure 35.

Minimum: -36.17

Maximum: -16.07

Mean: -35.78

Bin Width: 1.00

Number of Bins: 21

Water (70 - 74 degrees)

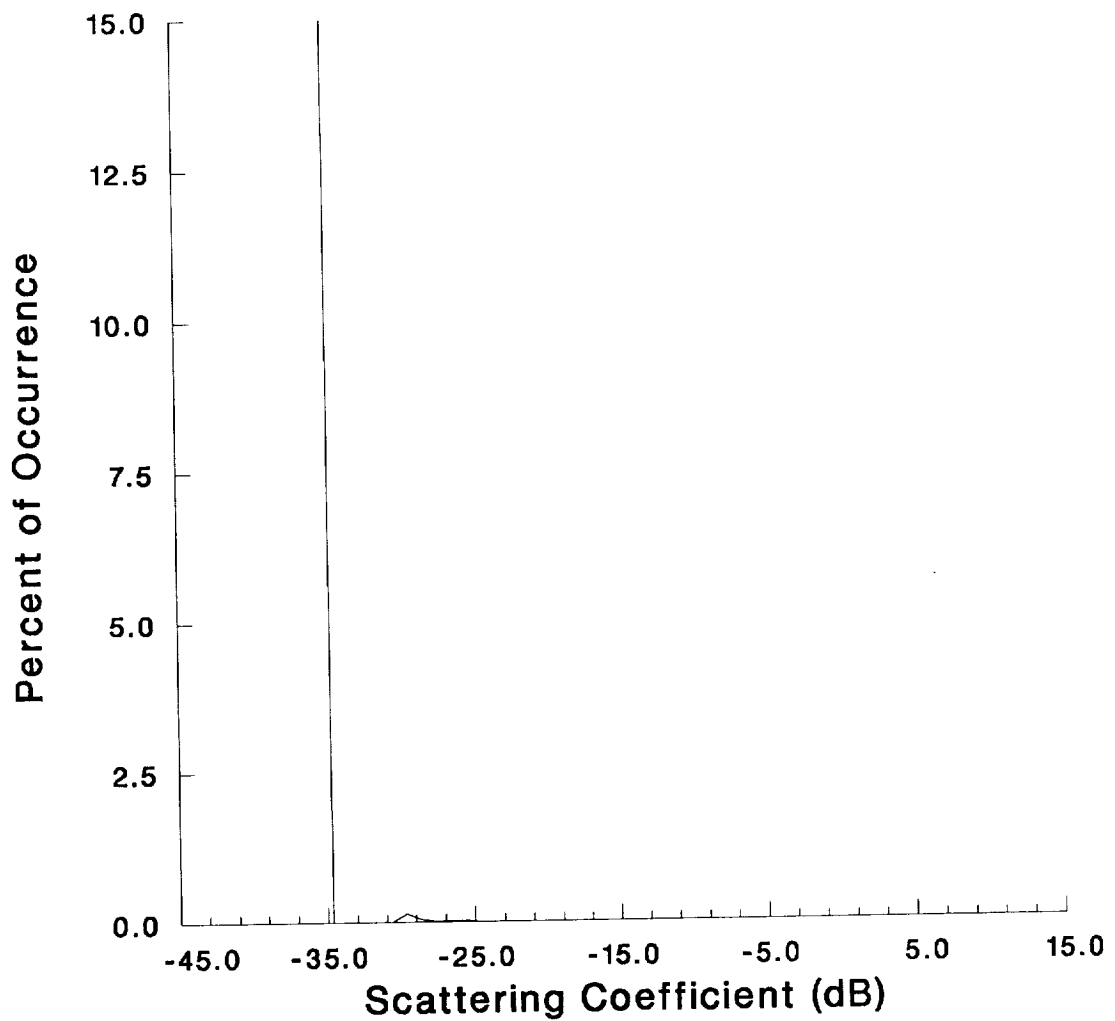


Figure 36.

Minimum: -36.17
Maximum: -25.36
Mean: -36.11
Bin Width: 1.00
Number of Bins: 12

Water (75 - 79 degrees)

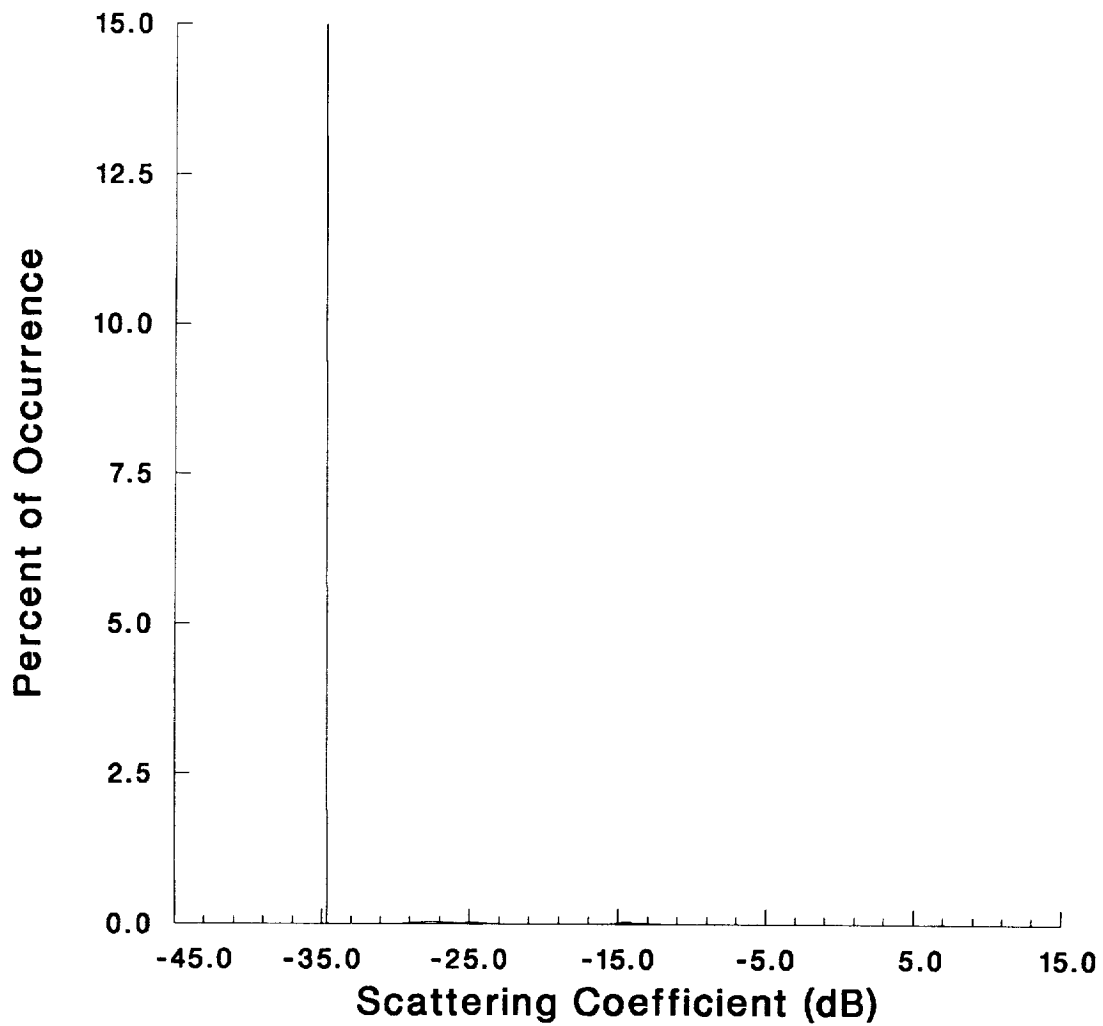


Figure 37.

Minimum: -36.17

Maximum: -11.59

Mean: -35.49

Bin Width: 1.00

Number of Bins: 26

Water (80 - 84 degrees)

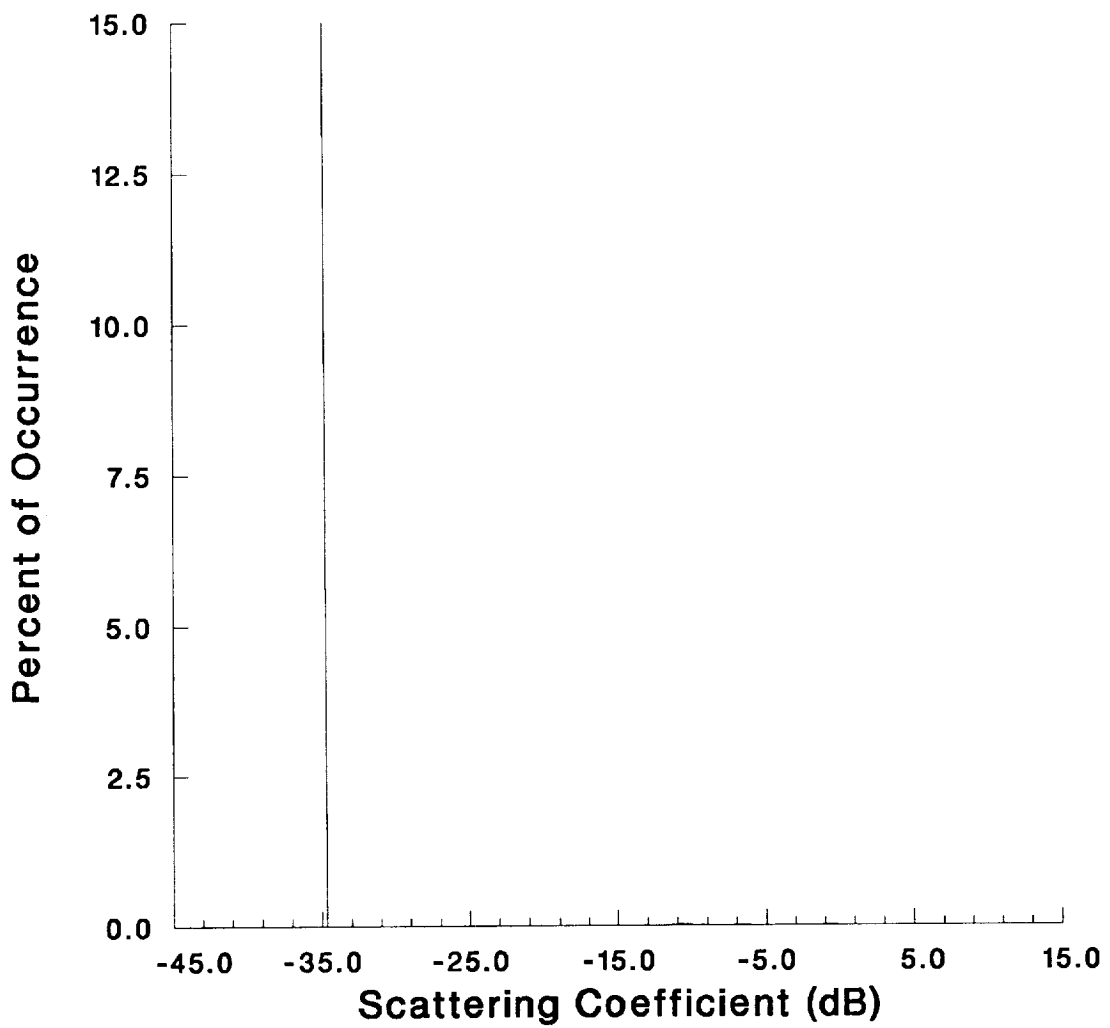


Figure 38.

Minimum: -36.17

Maximum: 0.98

Mean: -32.09

Bin Width: 1.00

Number of Bins: 38

Forest Clutter

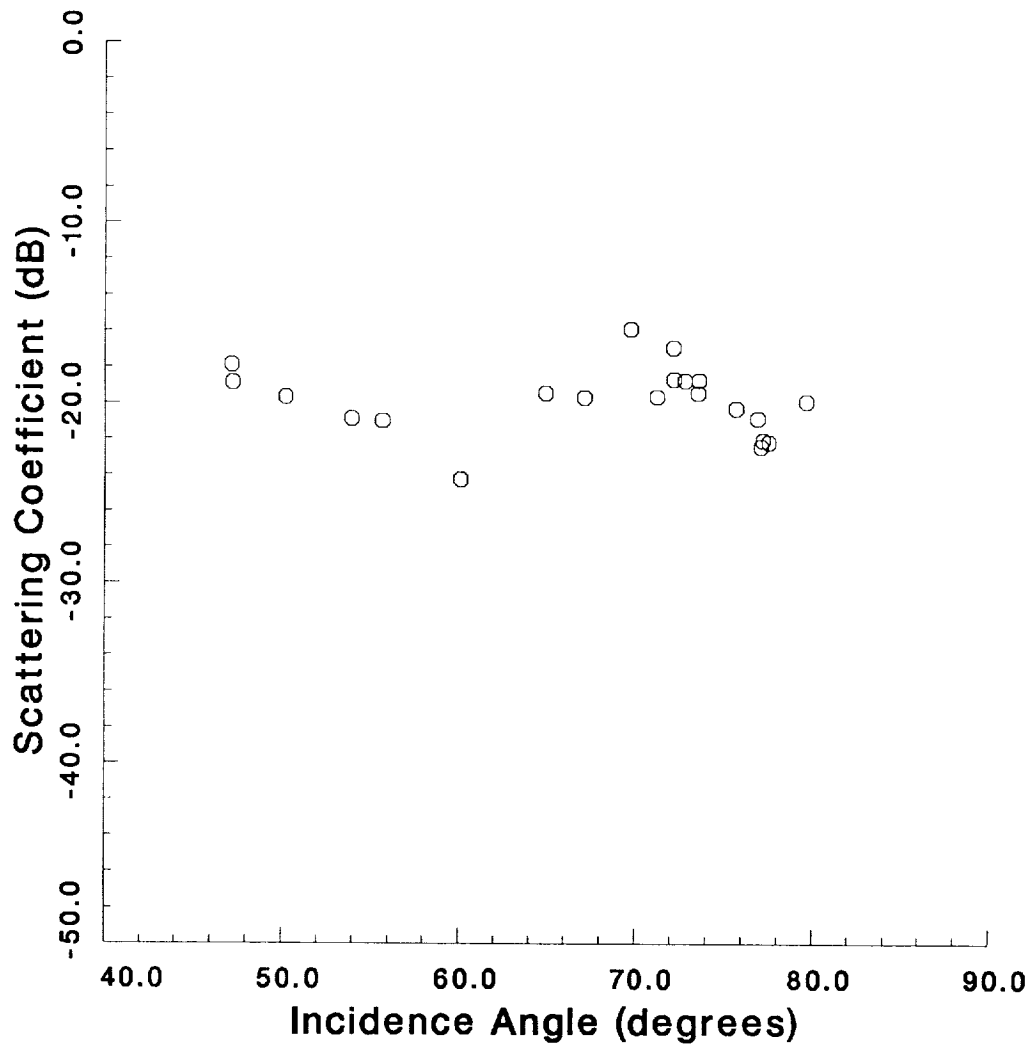


Figure 39. Incidence Angle vs Scattering Coefficient Plot for Forest Clutter

Residential Clutter

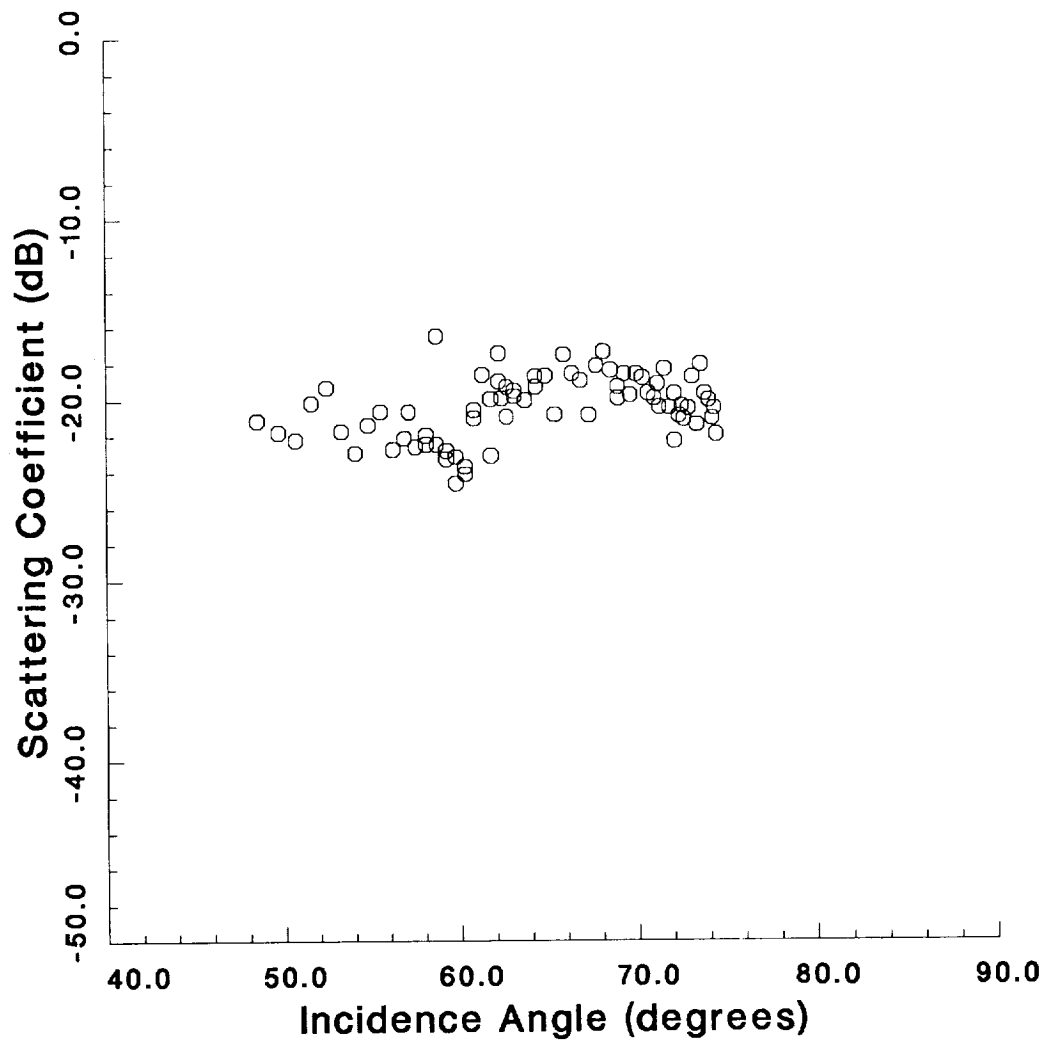


Figure 40. Incidence Angle vs Scattering Coefficient Plot for Residential Clutter

Grass Clutter

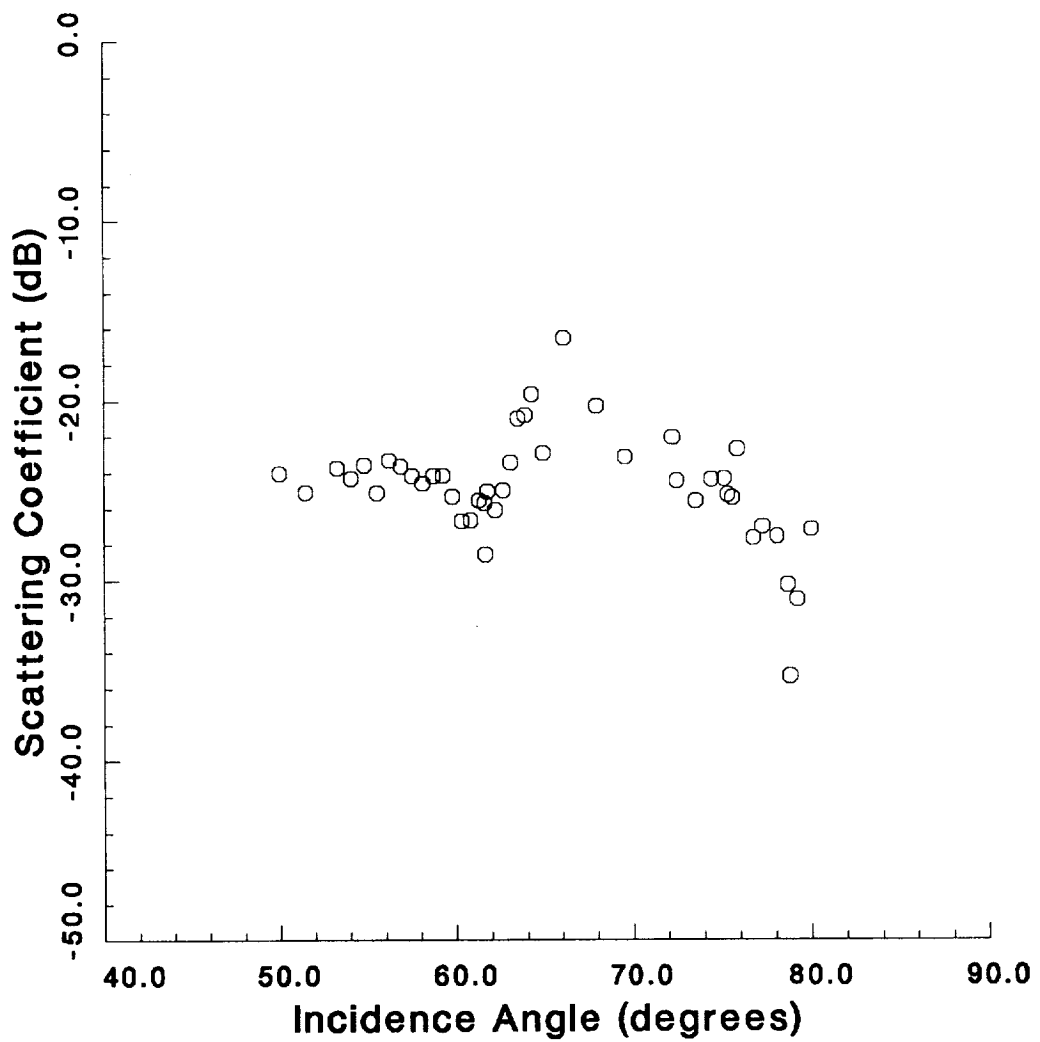


Figure 41. Incidence Angle vs Scattering Coefficient Plot for Grass Clutter

Water Clutter

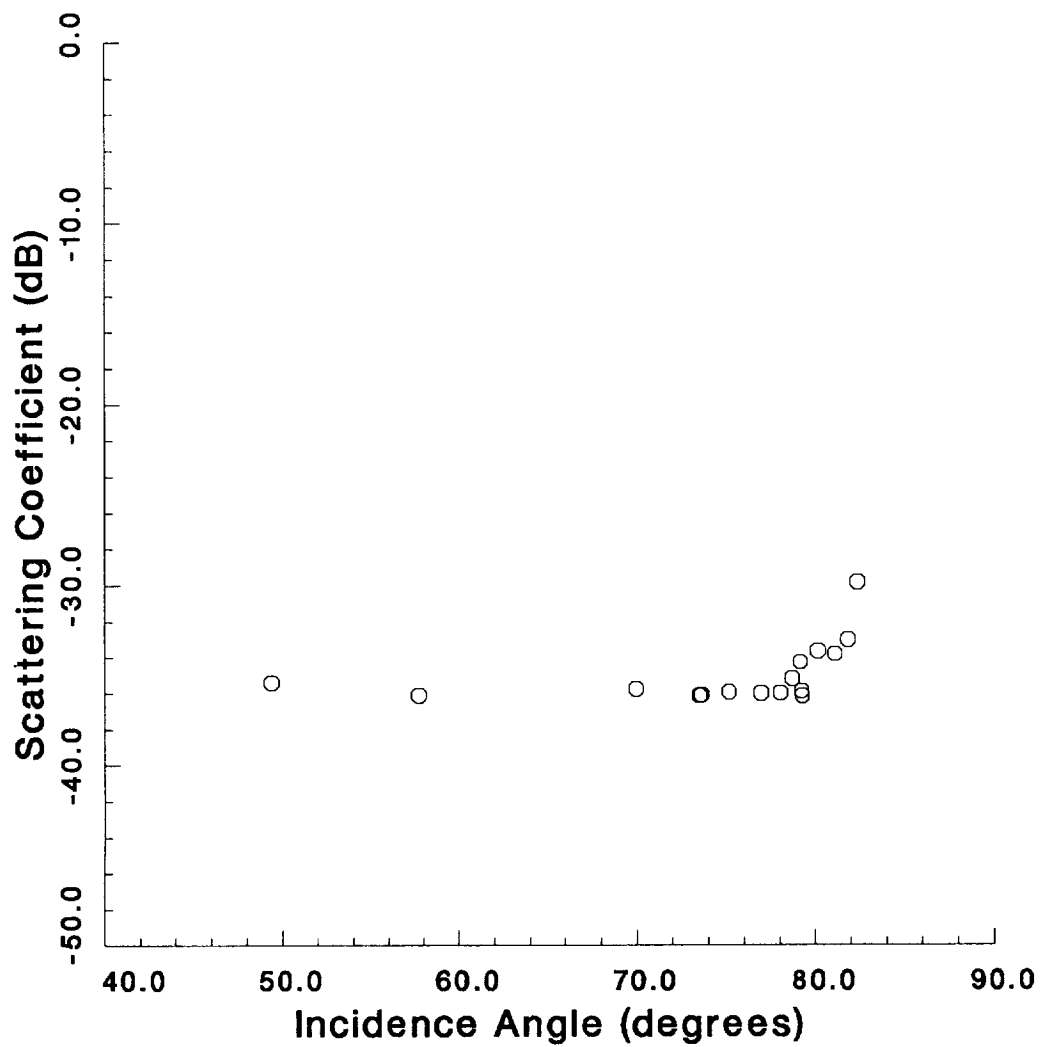


Figure 42. Incidence Angle vs Scattering Coefficient Plot for Water Clutter

Forest Clutter

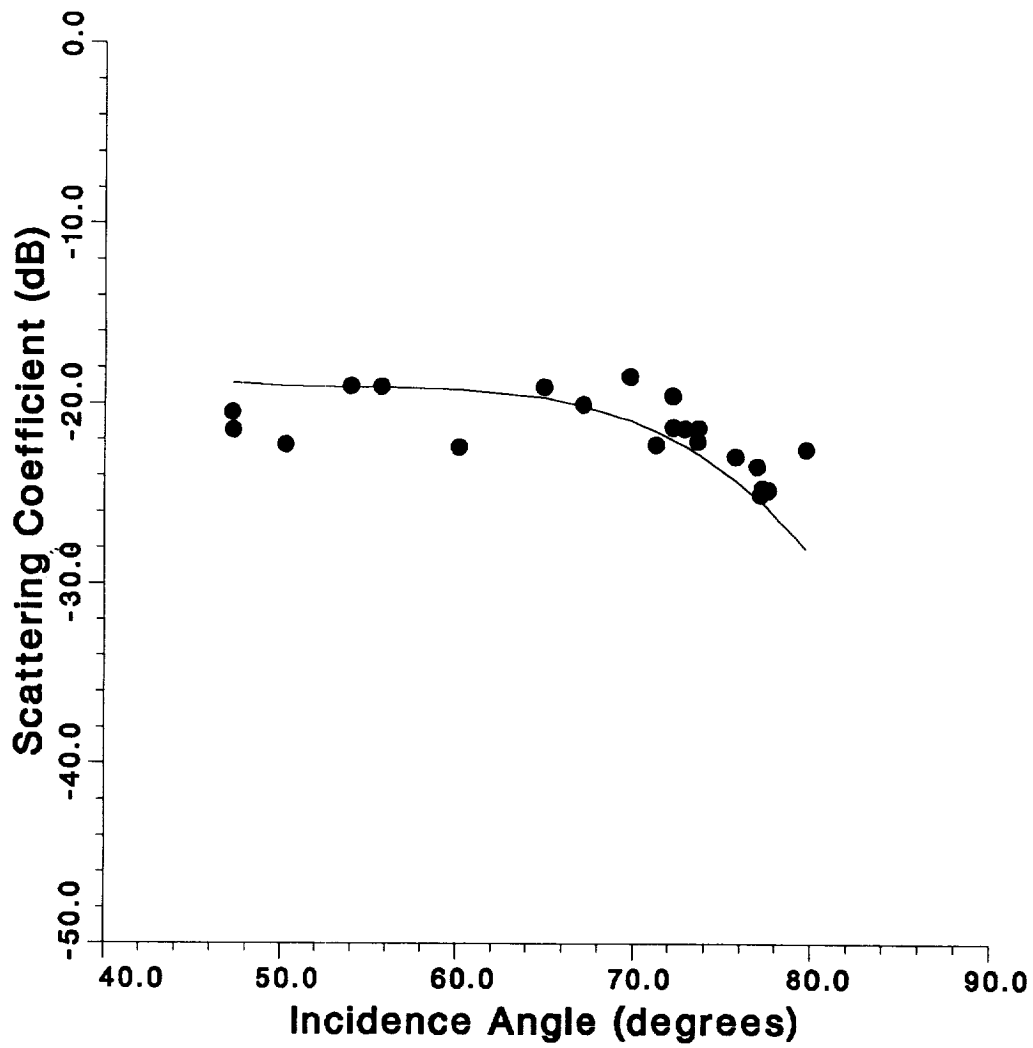


Figure 43. Polynomial Fit to Forest Data

Residential Clutter

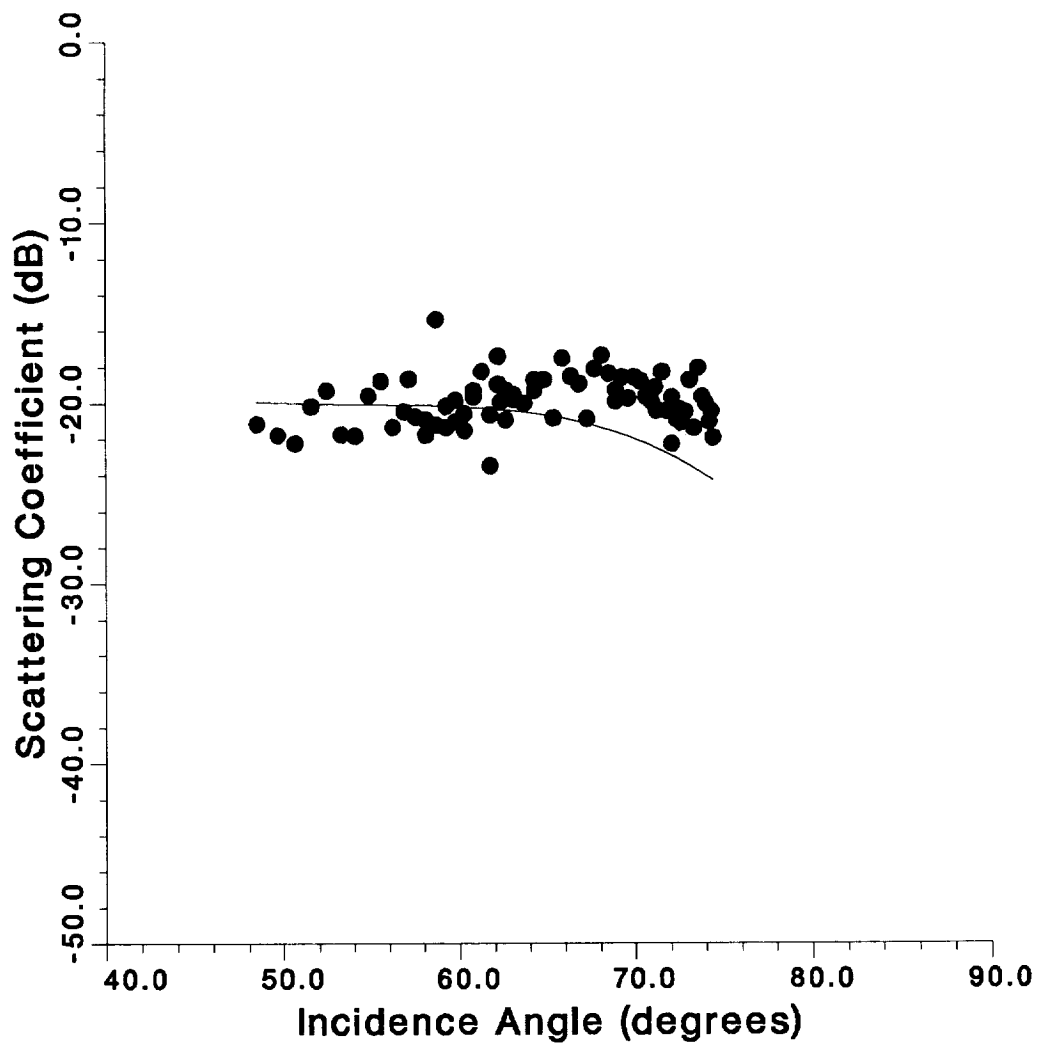


Figure 44. Polynomial Fit to Residential Data

Grass Clutter

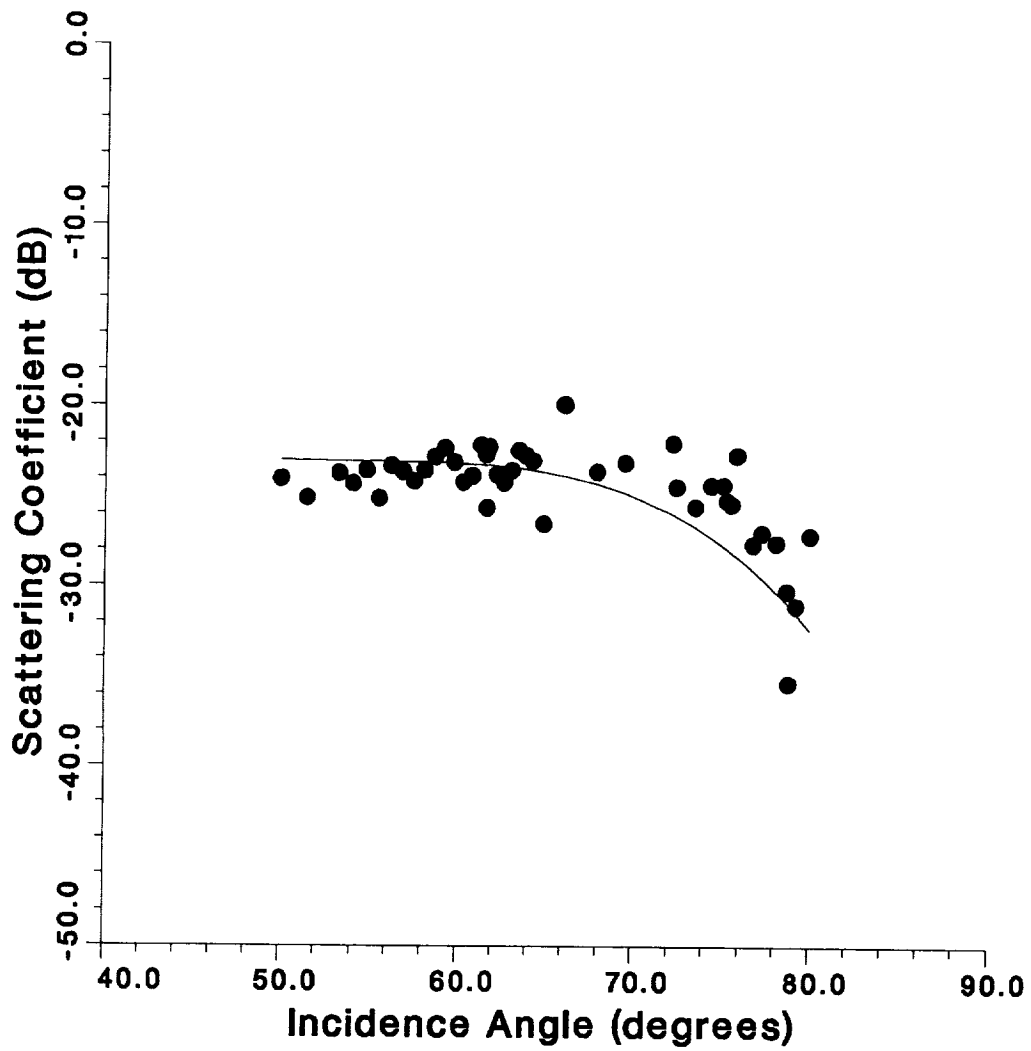


Figure 45. Polynomial Fit to Grass Data

ORIGINAL PAGE IS
OF POOR QUALITY

ORIGINAL PAGE IS
OF POOR QUALITY

Terminal (81 - 82 Degrees)

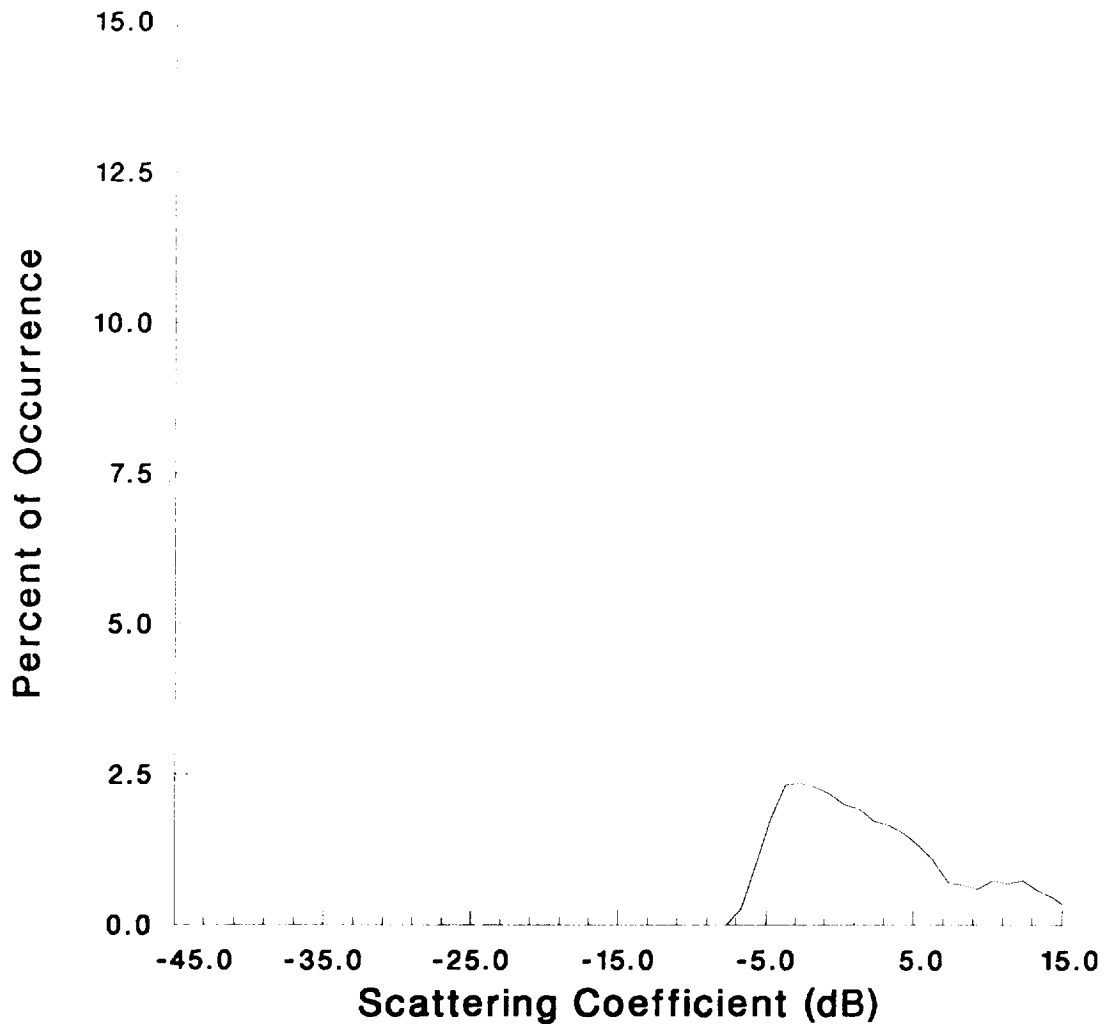


Figure 46.

Minimum: -5.94
Maximum: 27.03
Mean: -9.18
Bin Width: 1.00
Number of Bins: 64

ORIGINAL PAGE IS
OF POOR QUALITY

Building (78 - 82 Degrees)

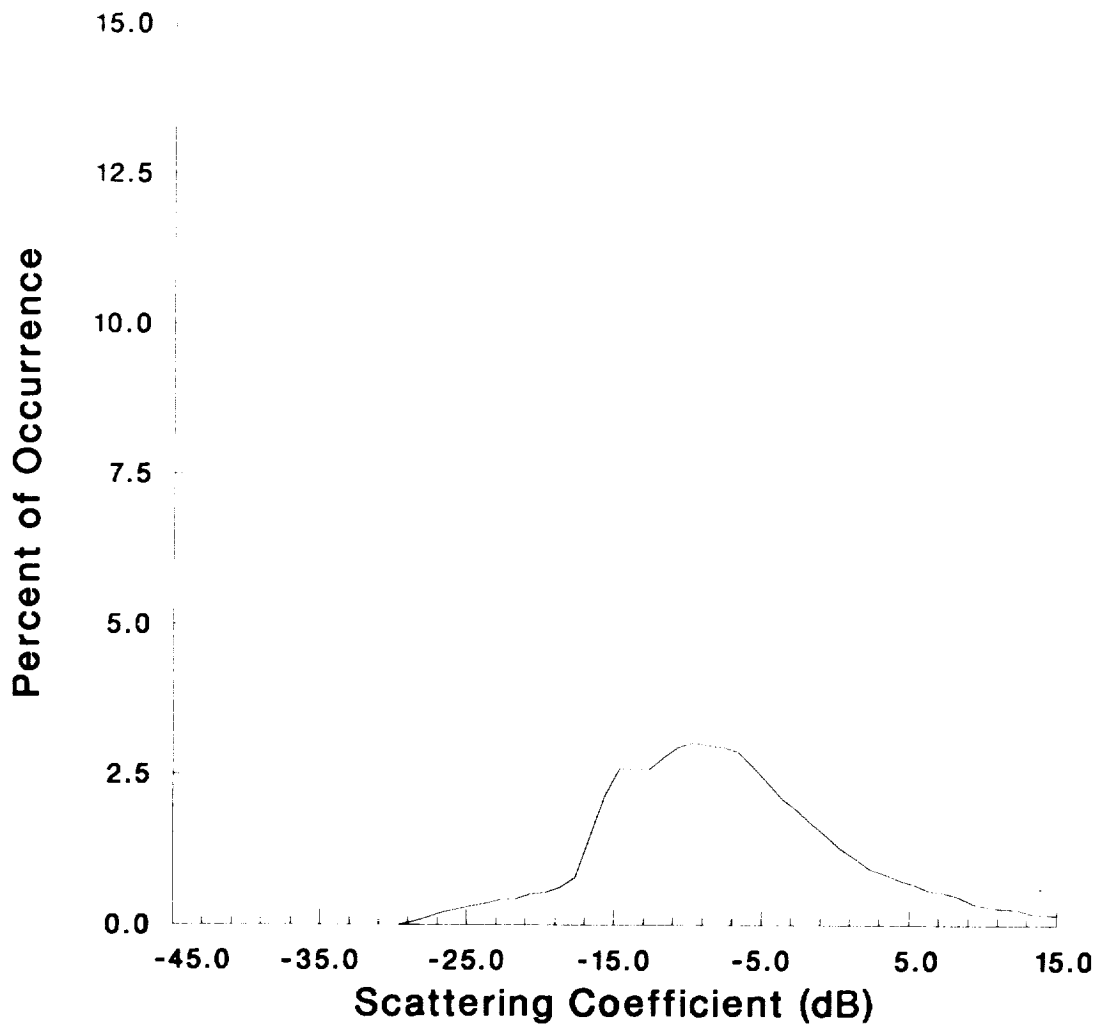


Figure 47.

Minimum: -27.98

Maximum: 27.93

Mean: -3.03

Bin Width: 1.00

Number of Bins: 65

ORIGINAL PAGE IS
OF POOR QUALITY

Refinery Tank

(50 - 59 Degrees)

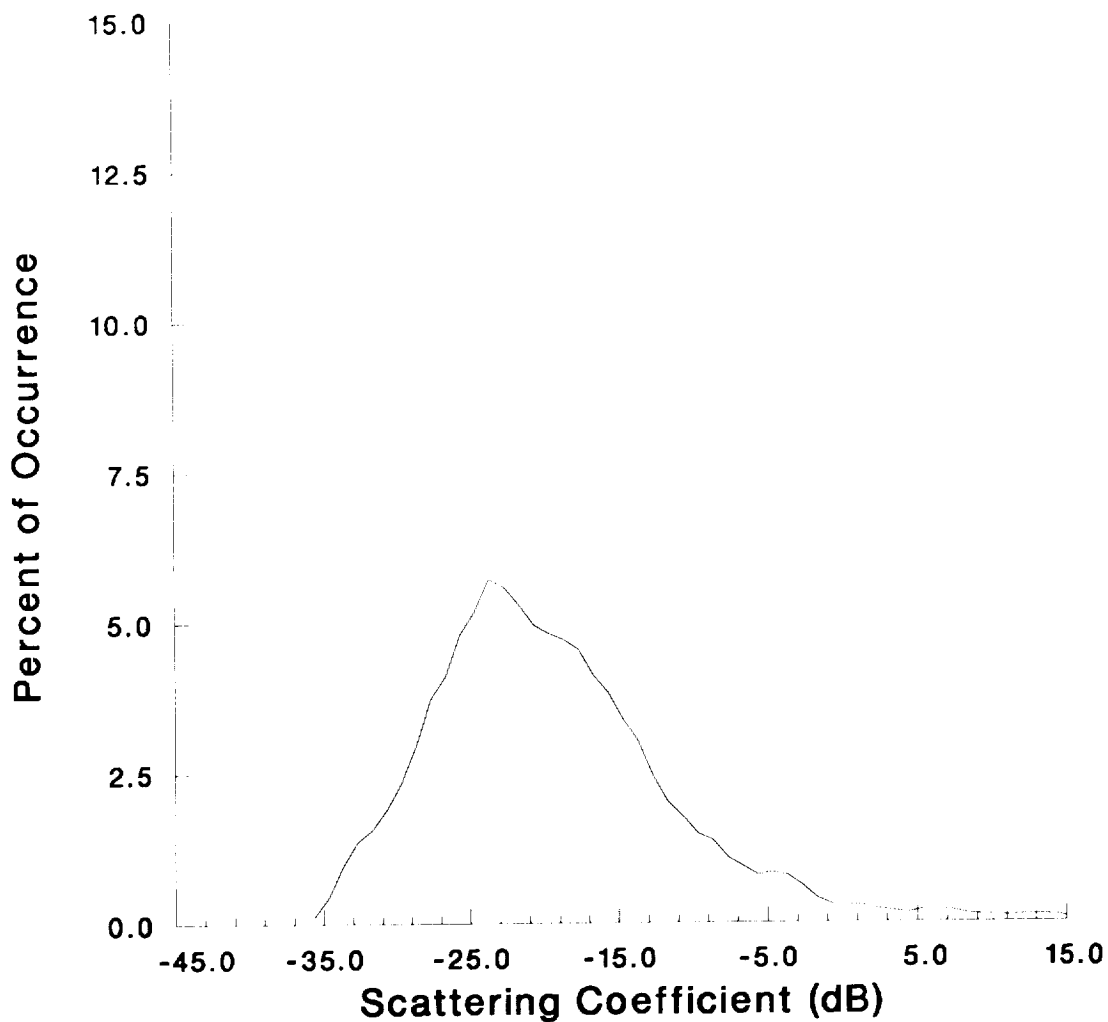


Figure 48.

Minimum: -36.06

Maximum: 18.73

Mean: -4.87

Bin Width: 1.00

Number of Bins: 56

Dock

(60 - 65 Degrees)

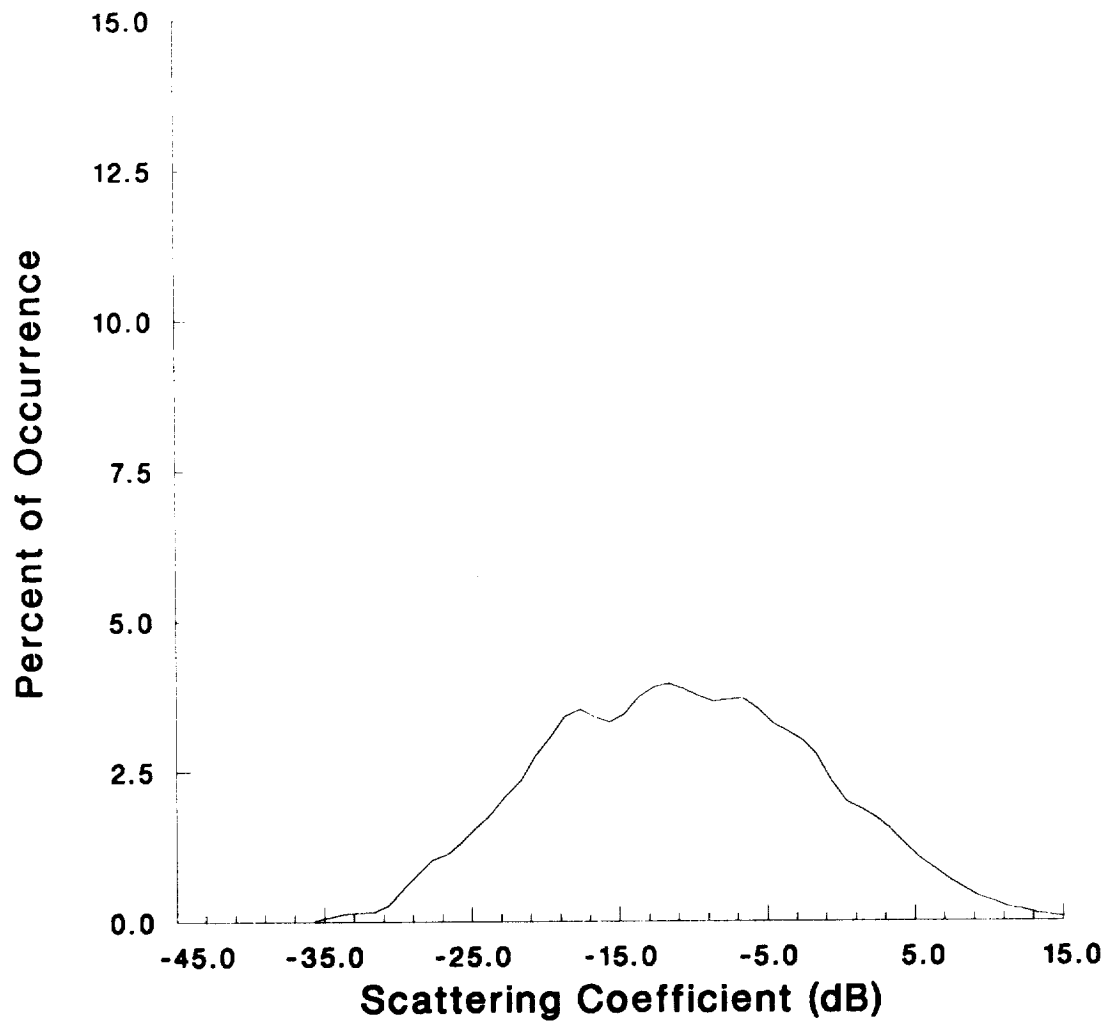


Figure 49.

Minimum: -35.87
Maximum: 23.93
Mean: -1.26
Bin Width: 1.00
Number of Bins: 61

ORIGINAL PAGE IS
OF POOR QUALITY

Bridge

(75 - 79 Degrees)

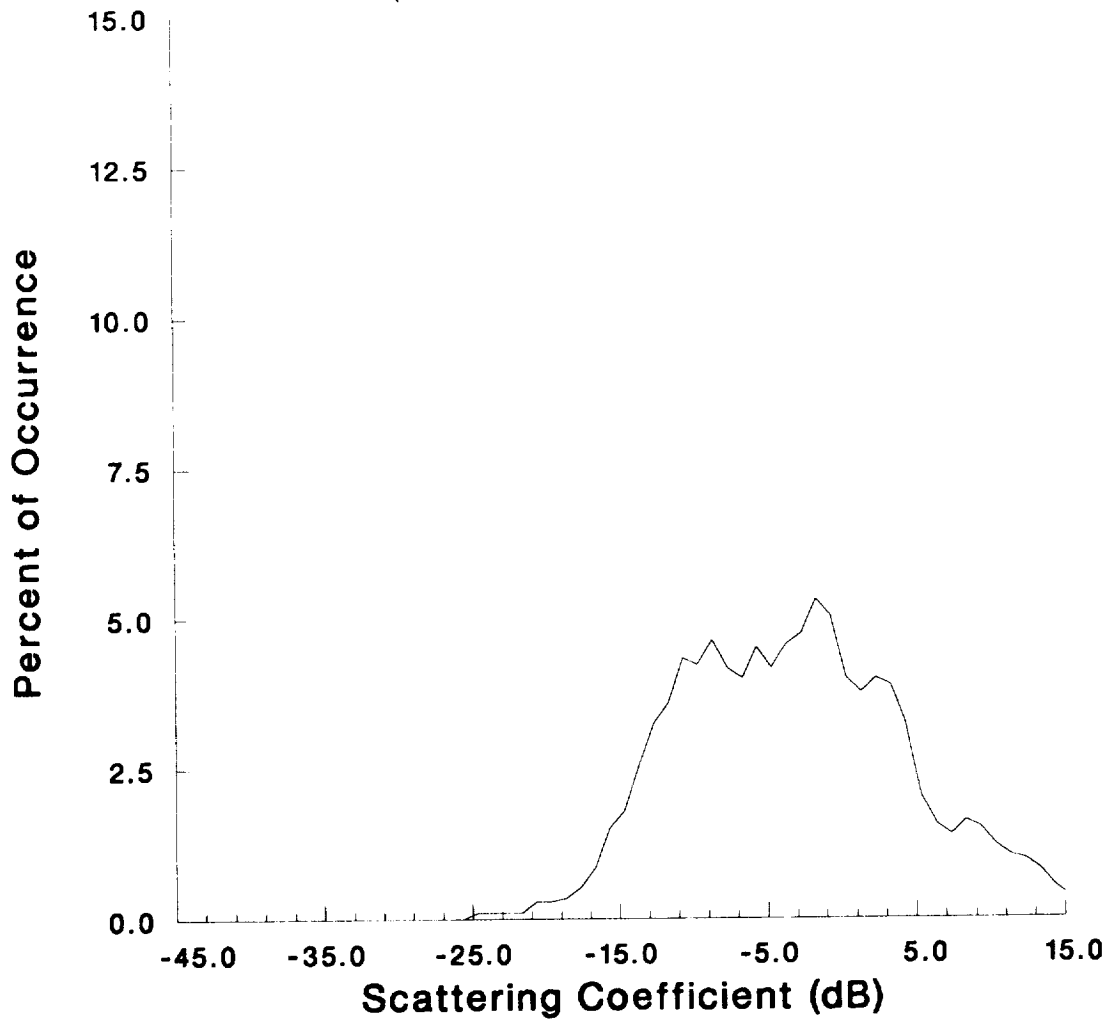


Figure 50.

Minimum: -24.11

Maximum: 19.77

Mean: -4.44

Bin Width: 1.00

Number of Bins: 57

Plane

(81- 82 Degrees)

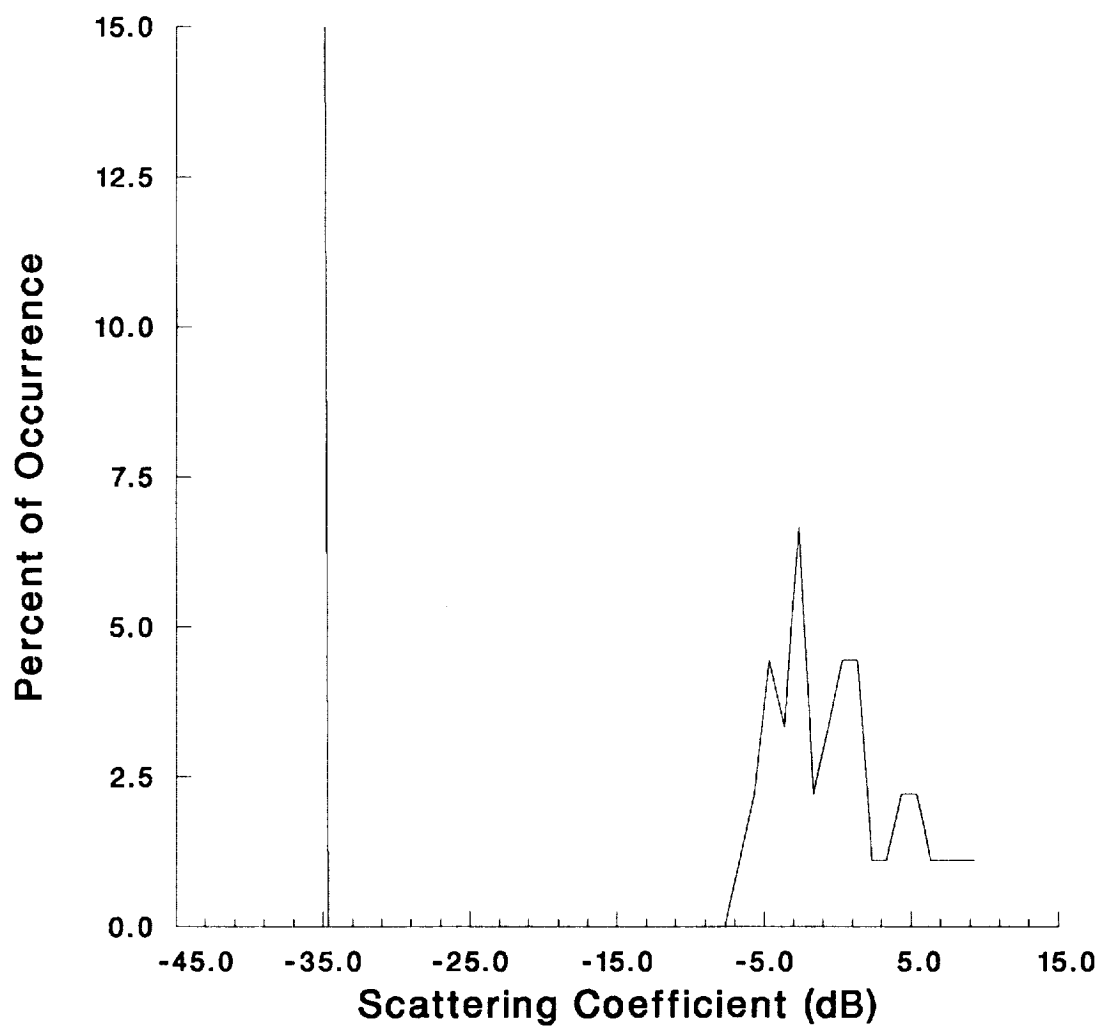


Figure 51.

Minimum: -6.57
Maximum: -9.03
Mean: -1.87
Bin Width: 1.00
Number of Bins: 46

Barge

(78 - 83 Degrees)

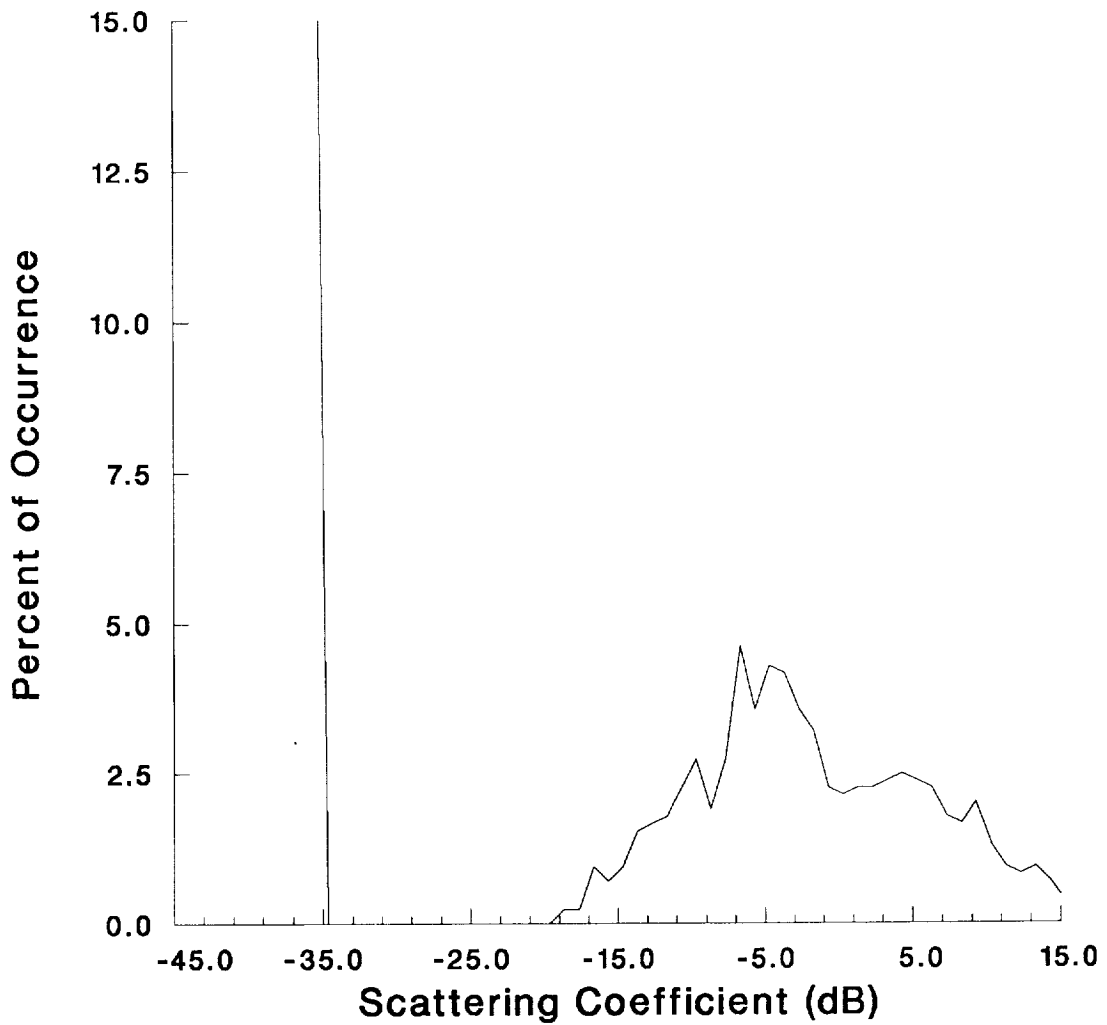


Figure 52.

Minimum: -19.02
Maximum: -17.14
Mean: -4.57
Bin Width: 1.00
Number of Bins: 54

Parking Lot

(65 - 69 Degrees)

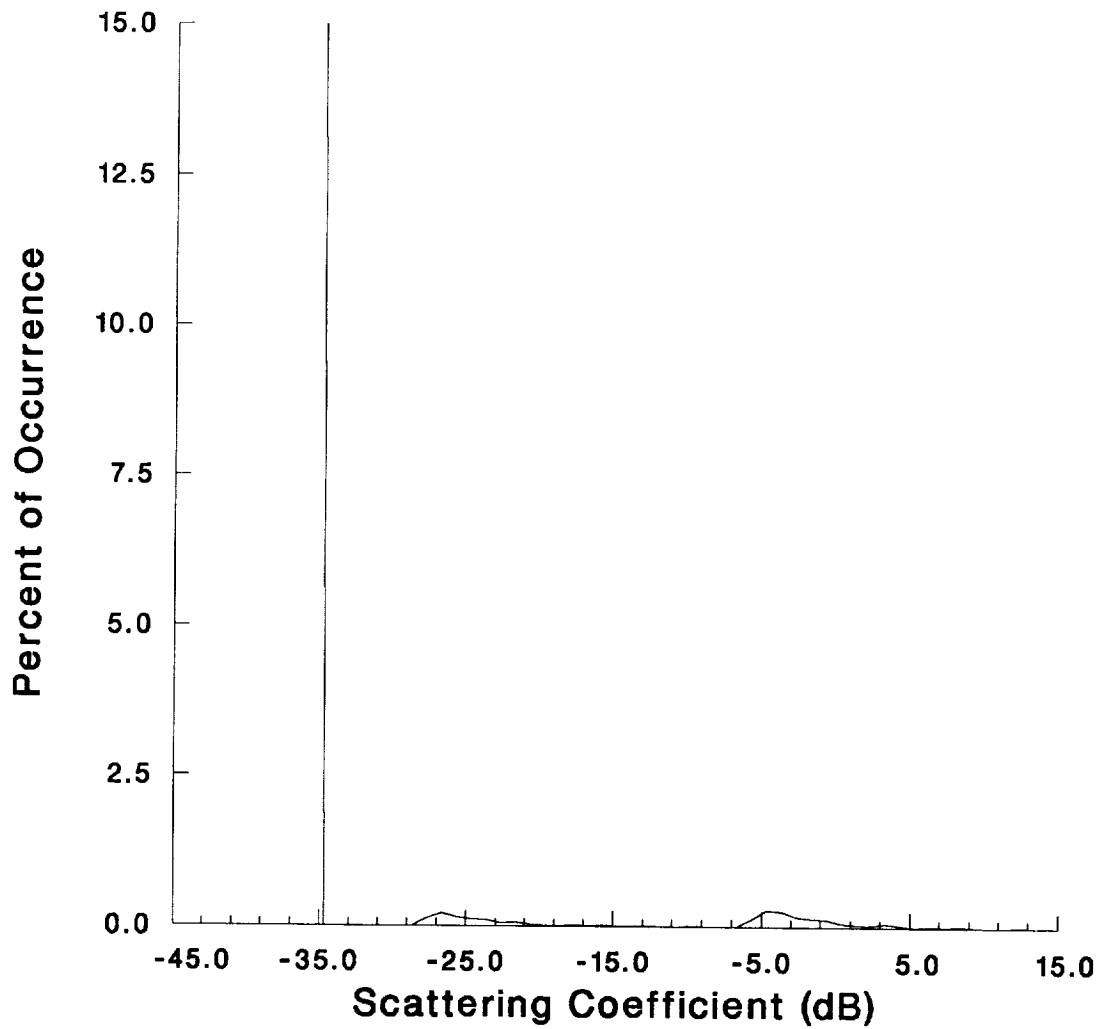


Figure 53.

Minimum: -27.63

Maximum: 20.31

Mean: -1.01

Bin Width: 1.00

Number of Bins: 57

REFERENCES

Ruck, G.T., D.E. Barrick, W.D. Stuart, and C.K. Krichbaum; Radar Cross Section Handbook, Vol. 2, pg. 593, 1970.

Onstott, R.G. and D.J. Gineris; Synthetic Aperture Radar Imagery of Airports and Surrounding Areas, Vol. 1, 1988.



APPENDIX A

POLARIMETRIC X/L/C-BAND SAR

R. Sullivan, A. Nichols, R. Rawson
Environmental Research Institute of Michigan
Ann Arbor, MI

C. Haney, F. Darreff, J. Schame, Jr.
Naval Air Development Center
Warminster, PA

Abstract

A new tri-band polarimetric synthetic aperture radar (SAR) has been developed for remote sensing applications and has been installed in a U.S. Navy P-3 aircraft. Pulses are transmitted in either X-, C-, or L-band. They may be transmitted at either horizontal (H) or vertical (V) polarization and received at either horizontal or vertical polarization. Transmit and receive polarization, as well as frequency band, may be switched pulse-to-pulse. Up to four different waveforms may be interleaved, e.g., X_{HH} L_{VV} X_{VV} C_{VH} or X_{HH} X_{HV} X_{VH} X_{VV} (full-polarimetric mode). A digital synthesizer produces the FM-chirp pulse. The pulse is emitted from a new tri-band antenna that is kept perpendicular to the aircraft ground track by means of a three-axis, servo-driven positioner which compensates for aircraft pitch, roll and yaw. Received pulses are digitized, preprocessed and recorded to high-density digital tape. Test flights began in late October, 1987 and preliminary imagery has been obtained.

Introduction

A SAR system, called the P-3/SAR, has been installed in a U.S. Navy P-3 aircraft and operates at X-, C- and L-bands with the capability of recording HH, HV, VH and VV polarizations. An earlier description was provided [1]. The system is a fully focused side-looking SAR capable of looking out either side of the aircraft. Operating center frequencies are 9.35 GHz, 5.30 GHz and 1.25 GHz. The system data are recorded in several forms. High-density digital tape (HDDI) is the primary recording medium. The data are also recorded on photographic film for subsequent optical processing. A real-time image formation processor records image data on heat-developed film or paper.

Figure 1 is a photograph of the P-3 aircraft. The radome aft of the wing contains the antenna and pedestal.

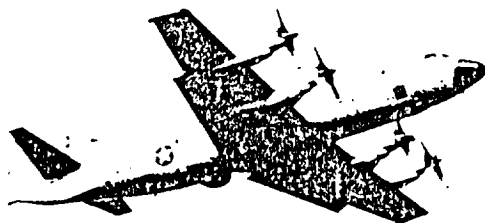


FIGURE 1. P-3 AIRCRAFT

Operating Modes

The P-3/SAR has five operating modes, summarized in Figure 2. For each mode, the figure illustrates the number of frequency/polarization combinations, the pulse repetition frequency (PRF) per combination, the number of range bins per pulse, the presum factor (data are presumed via a presum filter before being written to tape) and the corresponding data recording rate, tape speed and time to record a full tape. The rate of recording data to tape is

$$r = 2nfrNb/P$$

where

- n = number of frequency/polarization combinations
- f_R = PRF
- N = range bins per pulse
- b = bits in the A/D converter = 6
- P = presum factor.

The factor of 2 is to account for both I and Q.

The Single-Swath Multiplex Mode employs any four frequency/polarization combinations, except that (1) at least two different frequency bands must be used because of the transmitter duty-cycle limitation, and (2) each band must have a uniform PRF within the overall waveform. The PRF per combination is 2 kHz at a ground speed of 350 knots. (PRF is proportional to ground speed producing a constant value of pulses per unit ground distance). Four thousand ninety-six range bins per FM-chirp pulse are processed. These are presumed to a data rate one-sixth that which would result from no presumming. An example for this mode is shown in Figure 3.

The Double-Swath Multiplex Mode is similar except that for each pulse, the number of range bins is doubled to 8192. The number of frequency/polarization combinations is halved, to two, and the presum factor remains the same at six. Thus, the data recording rate is the same. An example is given in Figure 3. The Quadruple-Swath Multiplex Mode is completely analogous with one frequency/polarization combination, 16,384 range bins per pulse, a presum factor of six and the same data recording rate. An example is shown in Figure 4.

The Single-Swath Polarimetric Mode is similar to the Single-Swath Multiplex Mode except that all pulses are from the same frequency band and all four polarization combinations (HH, HV, VH, VV) are employed. This enables the full polarization scattering matrix to be recorded. Because of the transmitter duty-cycle limit of two percent, the PRF per combination is limited to 1 kHz instead of 2 kHz. The presum factor is reduced to three, again resulting in the same data recording rate. An example is given in Figure 4.

MODE	No. Freq/Pol Combinations = n	PRF ^a per Freq/Pol Combination = f_{11} (Hz)	Range Bins/pulse = N	Presum Factor = p	Nominal ^b Recording Rate - r $\frac{2nf_1 N}{p}$ (Mbit/sec)	Nominal ^b Tape Speed $v = \frac{r}{D}$ (in/sec)	Nominal ^b Tape Time $t = l/v$
Single-Swath Multiplex	4	2000	4096	6	65.5 (71)	61.6 (86.2)	35.4 (25.3)
Double-Swath Multiplex	2	2000	8192	6	65.5 (71)	61.6 (86.2)	35.4 (25.3)
Quadruple-Swath Multiplex	1	2000	16384	6	65.5 (71)	61.6 (86.2)	35.4 (25.3)
Single-Swath Polarimetric	4 ^c	1000 ^c	4096	3	65.5 (71)	61.6 (86.2)	35.4 (25.3)
Single-Swath No Presum	1	2000	4096	1	98.3 (106.5)	92.4 (129.3)	23.6 (16.9)

a - PRF is proportional to ground speed. Values given are appropriate for 350 knots.
b - Actual values, given in parentheses, are slightly different due to "second-order" effects such as record format, auxiliary data, etc.
c - Transmitter duty cycle is 4000 pulses/sec x 4 μ sec/pulse = 1.6 percent. Limit is 2 percent, preventing higher PRF.

b = bits in A/D = 6
 n_1 = no. tracks = 28
p = tape density = 38,000 bits/in-track
l = tape length = 10,888 ft = 130,656 in.

88 20020

FIGURE 2. OPERATING MODES

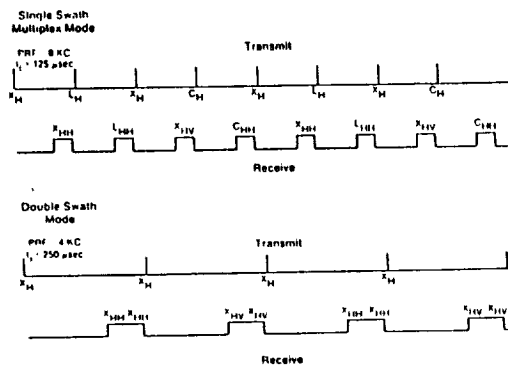


FIGURE 3. MODE TIMING DIAGRAM

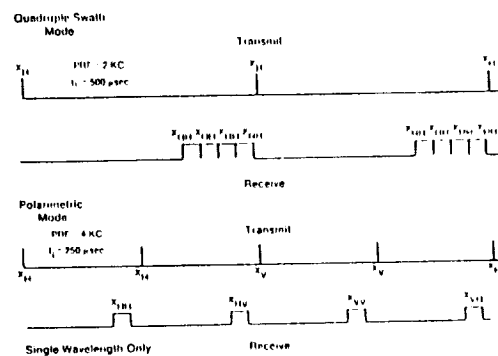


FIGURE 4. MODE TIMING DIAGRAM

The Single-Swath No-Presum Mode provides a capability for recording all of the Doppler data spatially filtered by the antenna beam. No additional azimuth filtering is applied to this data in the preprocessor. In this case, only one frequency/polarization combination can be used and the presum factor is one. The data recording rate is 1.5 times that for the other modes.

Subsystem Configuration

Figure 5 shows a simplified block diagram of the P-3/SAR system.

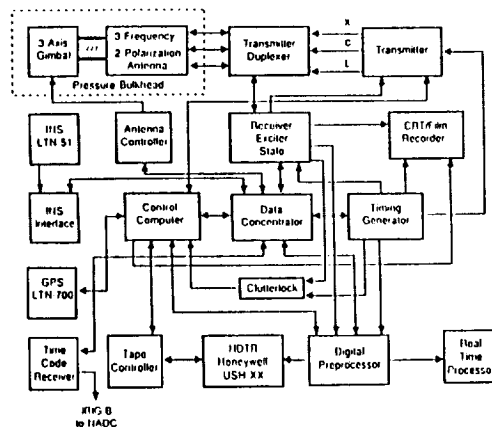


FIGURE 5. SYSTEM BLOCK DIAGRAM

The Inertial Navigation System (INS), a Litton LTN-51, performs several important functions for the radar system. It steers the aircraft via the autopilot during mapping, it points the antenna to 90 degrees from the ground track, it provides aircraft rotation data to the antenna gimbal systems for compensation of pitch and roll, and it provides aircraft lateral translation sensing for motion compensation of the radar data. Integrated INS three-axis accelerations are digitized in the INS interface and are input to the data concentrator. This computer resolves these inputs from the INS coordinate system into the radar coordinate system (along-track, cross-track, vertical) and then computes the velocity component along the radar beam. This beam velocity is scaled to radar wavelength and converted to phase corrections.

The linear FM chirp waveform is generated within the Receiver/Exciter/STALO using a digitally synthesized waveform generation technique described by Gallaway, et al. in another paper in these Proceedings. The chirp data points are stored in a PROM, then loaded into a RAM. The data points are read out of the RAM at the clock rate to produce the digital chirp waveform. This waveform is converted to an analog signal, then filtered and up-converted to the desired RF carrier frequencies for transmission. One feature of this technique is the capability to alter the chirp waveform data points in the PROM to compensate for range dimension hardware phase errors.

The chirp waveform is input to the transmitter where it is amplified by a traveling wave tube (TWT) amplifier. The X-, C- and L-band TWTs are manufactured by Hughes, Litton and Varian, respectively. A four microsecond pulse is transmitted for each band. The pulse repetition frequency (PRF) is proportional to ground speed to provide constant azimuth spatial frequency sampling. PRF is 8 kHz for a ground speed of 350 knots. The maximum transmitter PRF for any band is 4 kHz with the maximum transmit duty cycle equal to 2 percent for each band.

The amplified chirp waveform is passed to the Transmitter/Duplexer where a high-power switch selects the transmit polarization.

A triband (X-, C-, L-bands) dual-polarization antenna, developed by Chu Associates of Littleton, Massachusetts, is used for this system. The X- and C-band capability is provided by a dual, feed-on-focus shaped reflector based on the work of L.J. Chu [2]. The L-band capability is provided by a crossed-element Yagi array mounted on top of the X-C band reflector. This antenna is mounted on a new three-axis gimbal pedestal developed by Kintec Corporation of St. Petersburg, Florida. This gimbal system provides stabilization of the antenna with attitude reference data from the INS.

Backscattered signals are collected by the antenna and passed through the Transmitter/Duplexer where a switch selects the receive polarization. The Transmitter/Duplexer includes a transmitter power monitor capability which continually monitors average transmitter power. In addition, an injection port for amplitude-controlled synthetic targets is provided. This gives an end-to-end test capability for pre-flight and post-flight testing and system calibration.

The signal is then sent to the receiver which provides down-conversion of the X- and C-band RF channels to the L-band IF, band-limits the signals to support the desired range resolution and then amplifies the signals with minimal addition of noise. A digital phase shifter and frequency synthesizer within the receiver provide the motion compensation correction for the received signals based on the inputs from the INS.

The Receiver/Exciter/STALO provides complex I (in-phase) and Q (quadrature) analog video signals to the Digital Preprocessor, and real analog-video signals to the CRT/film recorder and clutterlock units.

The Digital Preprocessor performs A/D conversion of the I and Q analog video signals, buffers these signals to reduce the data rate, performs 6:1, 3:1 or no presampling of the input signals depending on the radar mode, and then formats the data for high-density digital tape recording (HDDIR) on the Honeywell AN/USH-XX 28 track tape recorder. The two-channel A/D converter required to digitize the complex radar video utilizes two 6-bit high-performance A/D converter circuits built at ERIM.

The AN/USH-XX HDDIR 28 tracks are utilized as follows: 24 tracks for four 6-bit complex video words, one track for auxiliary data (128 16-bit words per frame), one track for frame synchronization, and two tracks for error correction. Four thousand ninety-six complex words make up a frame of data.

The Digital Preprocessor also provides presumed I and Q digital video to the Real-Time Processor (RTP). The RTP performs single-channel, image-formation processing in real time. The output is displayed on a

VISOR hardcopy thermal paper recorder. This RTP provides capability for real-time check of the general navigation and also a coarse check on the system operation.

The CRT/Film Recorder provides a capability for recording one channel of video data on silver halide film for subsequent ground processing in an Optical Processor.

The clutterlock unit uses a low-frequency spectrum analyzer to measure the Doppler frequency centroid of the radar returns spatially filtered by the antenna beams. A cross-track velocity analog is developed from this Doppler frequency centroid; it is input to the Data Concentrator velocity filter to remove INS velocity biases.

The system computer consists of two HP 9000 Series 320 computers and peripherals to (1) provide operator control of the radar system signals, (2) perform the motion compensation computations, (3) provide an operator/display interface, and (4) concentrate data for auxiliary data recording and other functions. The Control Computer and associated monitor serve as the operator interface. This computer does all of the slower functions such as mode control, line navigation, system monitoring, etc. The Data Concentrator performs the motion compensation computations, converts the roll, pitch and yaw INS measurements into antenna stabilization and pointing commands, filters and combines the different sources of velocity measurements (INS, GPS and clutterlock), and assembles the auxiliary data for recording on the HDDTR.

The Time Code Receiver uses the GOES satellite data as a time base for comparing radar events with other data collection equipment events. This is distributed to other systems within the P-3.

The Global Positioning System (GPS) receiver provides an independent measure of aircraft position and velocity. The aircraft position (latitude and longitude) is used for manual update of the INS to improve the general navigation capabilities. The GPS velocities are resolved into along-track and cross-track velocities. The along-track velocity is used for setting the system PRF. The cross-track velocity is used as an input to the velocity filter to reduce INS biases. These inputs will be used when GPS data is available.

The system output products are (1) high-density digital tapes from the Honeywell AN/USH-XX HDDTR, (2) signal film cassettes from the CRT/Film Recorders, (3) a Control Computer printout which includes mode parameters, pass parameters, flight geometry and operator comments, and (4) 9-inch paper format real-time imagery from the VISOR recorder. The high-density digital tapes are played back in an ERIM facility where computer compatible tapes are generated for subsequent image-formation processing. The signal film data is chemically processed, then used in the optical processor to expose an image film.

Images are processed in one of three ways:

Optical-Optical: Raw video data from the on-board optical film recorder are processed via Fourier optics to produce imaging. This is the fastest processing method.

Digital-Optical: Data from the high-density data tape (HDDT) are transformed to video data on film, in the same format as that produced by the optical film

record, and then processed via Fourier optics to produce imagery. This can provide a quick look at the contents of an entire HDDT.

Digital-Digital: Data from the HDDT are processed via computer to produce imagery. This is the most precise method for analyzing a specific frame but is not generally suited to an overview of an entire flight.

Results

The first test flight of the P-3/SAR flight, designated as an engineering flight, occurred on 28 October 1987. The aircraft took off from Willow Run Airport near Ann Arbor, Michigan and was flown to the Straits of Mackinac and back twice, at an altitude of 15,000 feet. At the time, permission to transmit at L- and C-bands had not yet been received. Therefore, transmission was planned at X-band only. Data were collected at X_{HH} and X_{HV} .

Figure 6 shows "digital-digital" images of Saginaw, Michigan, taken at X_{HH} and X_{HV} . For each image, the gray scale was chosen to reveal maximum detail; thus, one cannot compare relative brightness between the two images. In general, the X_{HH} image contains many more sharp, specular reflections, for example in the region of the Saginaw Fair Grounds. It is interesting to note the return from the railroad tracks at both X_{HH} and X_{HV} . The long north-south portion of the tracks is essentially parallel to the aircraft flight path; there is also a set of tracks approximately perpendicular to the flight path. At X_{HH} , where the transmitted and received electric vectors are parallel to the flight path, the "parallel" tracks produce a brighter return than the "perpendicular" tracks. At X_{HV} , the perpendicular tracks are brighter than the parallel tracks.

Acknowledgments

The authors acknowledge valuable assistance from many other individuals, including the following: G. Adams, E. Cowen, M. O'Mango, B. Orlullo, A. Brown, J. Gaffield, W. Gallaway, D. Gieris, R. Huxtable, L. Lambert, G. Leiby, S. Smith, J. Steinhacher, C. Stout, J. Toffi and C. Wackerman.

References

- [1] A. Kozma, A. Nichols, R. Rawson, R. Shackman, C. Haney and J. Schame, Jr., "Multifrequency-Polarimetric SAR for Remote Sensing," in Proceedings of the IEEE Geoscience & Remote Sensing Society, 8-11 September 1986, pp. 715-719.
- [2] Silver, J., Microwave Antenna Theory and Design, McGraw-Hill, 1949, pp. 497-500.

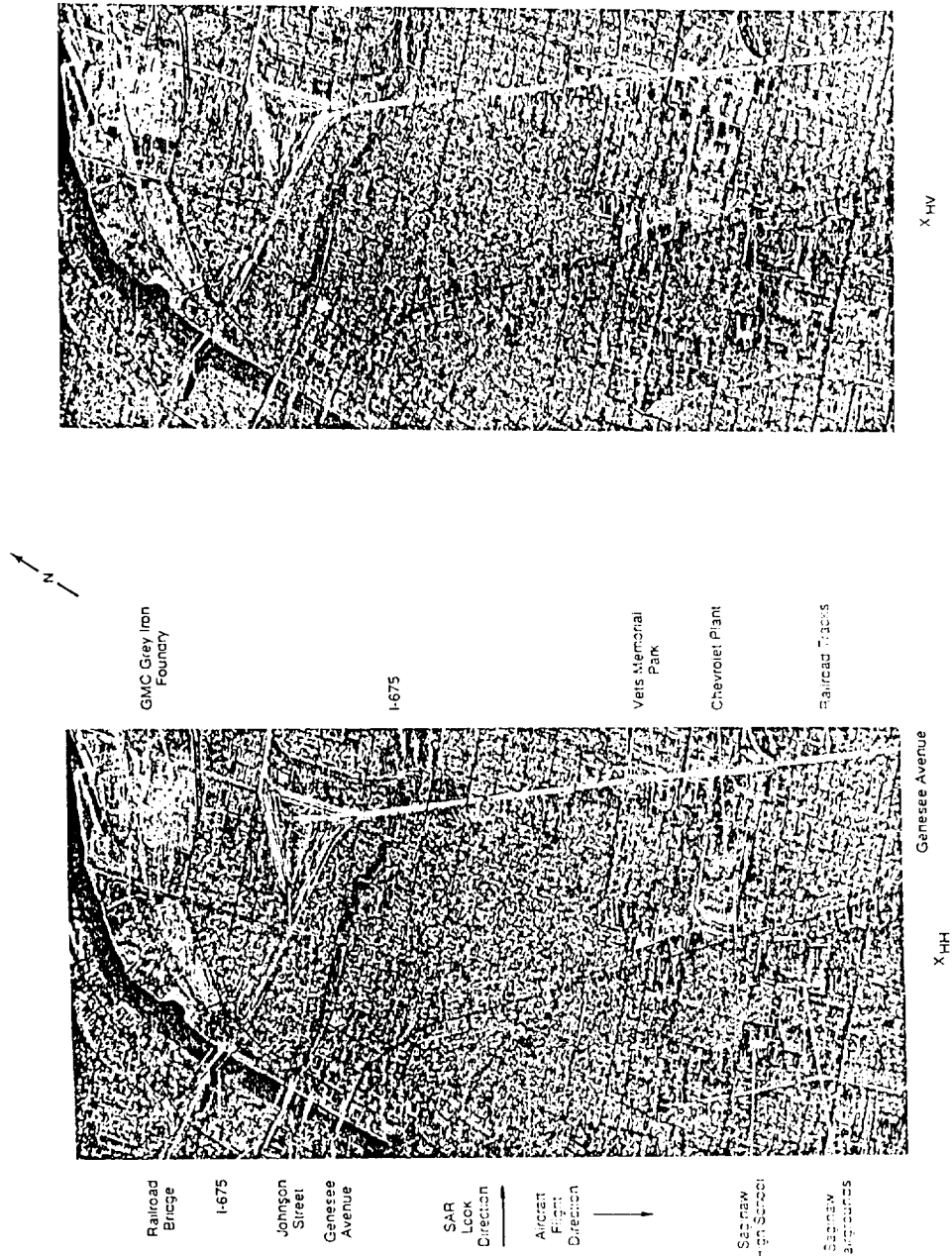


FIGURE 5. P-3 SAR IMAGES OF SAGINAW, MICHIGAN

Biographies



Dr. Roger J. Sullivan received the B.S. and Ph.D. degrees in physics from the Massachusetts Institute of Technology. Prior to joining the Environmental Research Institute of Michigan in 1986, he was at System Planning Corporation 1973-1986 and the Illinois Institute of Technology Research Institute 1969-1973.



Mr. Alan D. Nichols received the B.S. and M.S. in electrical engineering from the University of Iowa and the University of Michigan respectively. Mr. Nichols has been with the Environmental Research Institute of Michigan since 1979. Prior to this period he spent 1972 through 1979 at McDonnell Aircraft Company and 1961 through 1972 at Conduccion Corporation.



Mr. Robert F. Rawson received the B.S. degree in electrical engineering from the University of Michigan. He has been on the staff of the Environmental Research Institute of Michigan since 1961.

Mr. Charles W. Haney received the B.S. in physics at St. Joseph's University and performed graduate studies at Columbia University. He has been at the Naval Air Development Center since 1963.

Mr. Joseph J. Schanne, Jr., received the B.S. degree in electrical engineering from Drexel University in 1985. He has been at the Naval Air Development Center since then.

Mr. Francis P. Darreff received the B.S. and M.S. degrees in electrical engineering from Drexel University in 1962 and 1967 respectively. He has been at the Naval Air Development Center since he was a co-op student.

APPENDIX B SAR CALIBRATION

In this Appendix the calibration of the Philadelphia image is discussed in detail. When a SAR system is operated in the linear region there exists a one-to-one correspondence between the image intensities of targets in a scene and the radar cross-sections of those targets. To account for radar system gain effects and the benefits gained in optimizing the recording process, the data undergoes scaling as it is collected. One purpose of absolute calibration is to determine this constant and to rescale the image intensities values so they now represent absolute scattering cross-sections. If the cross-sections are normalized by the pixel area than they are referred to as normalized radar cross-sections (NRCS) or scattering coefficients.

Since there were no reflector arrays in the Philadelphia image, we used a calibration scene collected at the Patuxent Naval Air Test Center, Maryland, two weeks prior to the Philadelphia image to calibrate the data. This can be done because the P-3 SAR system transfer function is continuously monitored throughout the data collection.

As discussed in the first SAR data report, the linear relationship between σ , the expected radar cross-section of a reference target, and P_I , the measured image intensity from a radiometrically corrected image of this target is given by:

$$\sigma = \frac{P_I - P_N}{K} \quad \text{Eq. (B-1)}$$

where P_N is the system noise and K is the system gain constant. K is determined from the intercept of the calibration function with the P_I axis.

The radar scattering cross-sections for each of the triangular trihedral reflectors used in the calibration array may be accurately calculated using the equation provided in Ruck et. al., (1976)

$$\sigma(\theta, \phi) = \frac{4\pi \alpha^4}{\lambda^2} \frac{\cos\theta + \sin\theta(\cos\phi + \sin\phi)}{[\cos\theta + \sin\theta(\cos\phi + \sin\phi)]^2} \quad \text{Eq. (B-2)}$$

where θ is the angle between the vertical crease of the trihedral and the direction of illumination, ϕ is the offside angle to the trihedral, α is the length of the trihedral along a crease, and λ is the wavelength of the radar. In this calibration array, the trihedrals were placed so that they were flat on the ground and their aperture faced the look direction of the radar. In this case, the angle θ is simply equal to the incidence angle to any reference trihedral is given as:

$$\theta = \cos^{-1} \frac{H}{R_s} \quad \text{Eq. (B-3)}$$

where H is the altitude of the radar and R_s is the slant range to the reflector. The slant range to the reflector is given by:

$$R_s = (T_d * 150.00) + (Pr1 - 1) * R_{ps} \quad \text{Eq. (B-4)}$$

where the quantity T_d is the time delay to ground cells in the near range of the image, $Pr1$ the peak record location, and R_{ps} the pixel spacing. The values of α , crease length, were 0.3 m, 0.45 m, 0.6 m, 0.75 m, 0.9 m, and 1.2, for the reflectors used in the calibration analysis.

The image intensities of each of the calibration reflectors were measured by positioning a 32 x 32 pixel window around the apparent peak of each reflector. Upsampling was performed to improve the accuracy of the estimate of the energy associated with the reflector. The upsampling was accomplished by taking the Fourier transform of the data contained in the 32 * 32 pixel window. In the frequency domain the bandwidth of the data is determined by the sample size of the image data. By 'zero-padding' the data in the Fourier domain the information

content was preserved but pixel spacing in the image domain was reduced. Given the upsampled data, the total reflector energy was calculated. These values were then radiometrically corrected and the effects of local system noise and background clutter were removed. The average intensity of the sum of the clutter and system noise was calculated by finding the mean intensity value of a small area near, but not interfered by, the target of interest. The amount of background energy which contributes to the reflector energy, P_B , is given by:

$$P_B = ((\bar{V}_B)**2)*r_a*r_r$$

where \bar{V}_B is the average background amplitude near the reflector, r_a is the azimuth resolution, and r_r is the range resolution. Subtracting this from the total 3 dB image intensity values removes the background clutter and system noise, P_n .

Next, the effect of antenna gain pattern and range fall-off were removed from each image intensity value. In essence, we performed a radiometric correction to each reflector energy identical to that which is performed on the entire image. The transmit and receive antenna patterns act as weighting factors in the image. Each pixel of the image is multiplied by a scale factor which is the product of the transmit and receive antenna pattern. The pattern used to correct the Philadelphia Airport image is illustrated in Figure B-1. To remove the effects of antenna pattern one needs only to multiply the measured image intensity value by the inverse of the transmit and receive antenna patterns. Range fall-off is removed by multiplying the measured intensity values by the square of the slant range to the point of interest. An R^2 factor is employed instead of an R^4 because the SAR processor removes two orders of the range fall-off effect as the data is convolved with its match filter in azimuth. The data is then normalized to a reference range, which is set to be slant range at the antenna boresight. The corrected reflector energy P_{rc} is then:

$$P_{rc} = \frac{(P_r - P_B) * R_s^{**2}}{(R_{ref}^{**2}) * G_t * G_r}$$

where P_r is the total 3 dB energy, P_B is the total background energy, R_s is the slant range to the reflector, R_{ref} is the reference slant range, G_t is the transmit antenna pattern gain, and G_r is the receive antenna pattern gain.

The normalized reflector image intensity P_{rc} is then plotted against the expected RCS of the reflectors and the system gain constant is determined from the intercept of a least squares fit line through the data with a slope of one. In the case of the Philadelphia Airport image, since the calibration was performed on another image, we also adjusted for differences in transmitted power, stable local oscillator attenuation, processing scale, depression angle, and altitude. The calibration data are plotted in Figure B-2.

X-HH ANTENNA PATTERN

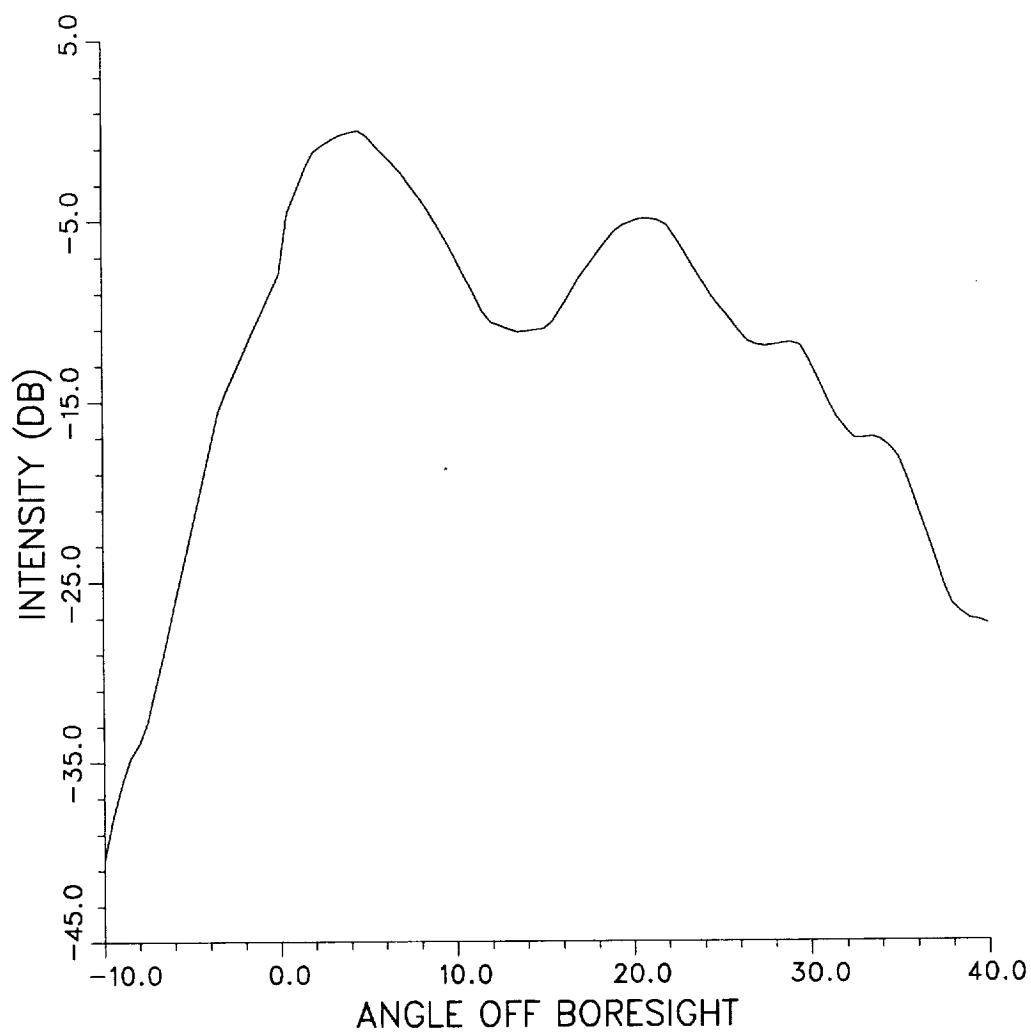


Figure B-1

P3T576/586 Calibration Using P3T548

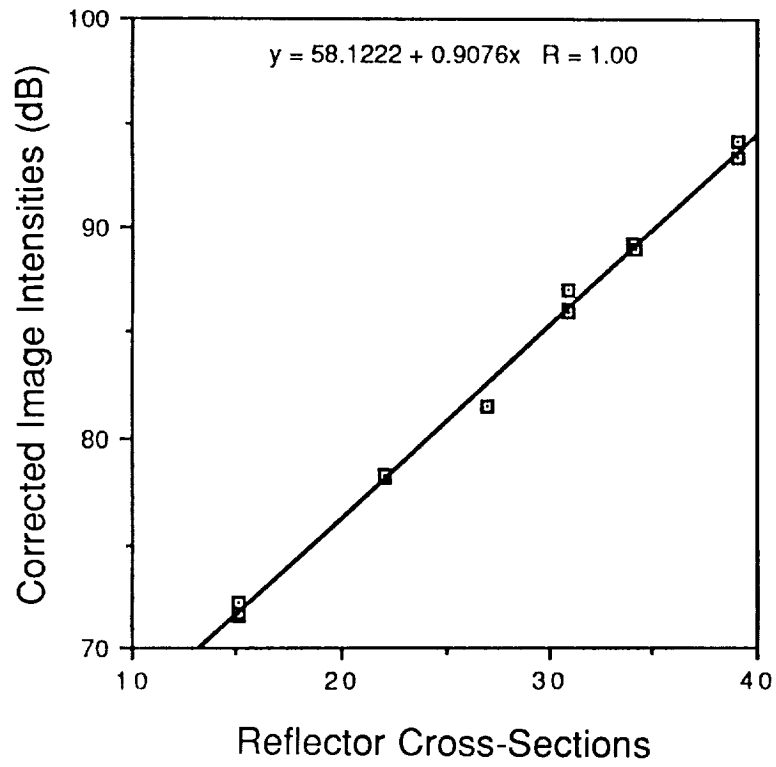


Figure B-2

APPENDIX C
STATISTICAL FORMULATION

In this appendix, we describe the calculation of the statistics used to describe the scattering properties of the various clutter types. The mean μ of a data set is given by:

$$\mu = \frac{1}{N} \sum_{i=1}^N x_i \quad \text{Eq. (C-1)}$$

where N is the total number of data values and x_i , represents an individual data values.

The variance σ^2 is given by:

$$\sigma^2 = \frac{1}{N} \sum_{i=1}^N (x_i - \mu)^2 \quad \text{Eq. (C-2)}$$

The standard deviation is defined as the positive square root of the variance. The coefficient of variation is given by the ratio of the sum of the standard deviation plus the mean to the mean of the data set.

$$C_v = \frac{\sigma + \mu}{\mu} \quad \text{Eq. (C-3)}$$



Figure D-1. Locations Where Clutter Analysis Surveys of the Philadelphia Airport SAR Scene Conducted

Table D-1. Statistical Analysis Results for Individual Clutter Groups

Id	Region Type	# Pts	Incidence Angle	Min (dB)	Max(dB)	Mean (dB)	Variance	SDEV	Variation
I1	Industrial	11250	56.78	-36.17	14.87	-14.42	0.19943E+00	0.44658E+00	0.23267E+02
I1	Water	15000	49.39	-36.17	12.92	-35.42	0.47384E+06	0.68836E+00	0.12395E+01
W2	Water	15000	36.17	-36.17	-16.94	-36.12	0.17130E-08	0.41389E-04	0.16940E+00
W3	Water	15000	69.98	-36.17	-16.07	-35.78	0.15572E-06	0.39461E-03	0.14943E+01
H1	Refinery Dock	1000	60.37	-36.17	14.18	-5.06	0.15563E+01	0.12475E+01	0.40029E+01
H2	Refinery Dock	1000	63.49	-36.17	12.56	-3.77	0.18774E+01	0.13702E+01	0.32607E+01
H3	Refinery Dock	1000	65.20	-36.17	11.53	-2.76	0.14345E+01	0.11977E+01	0.22596E+01
H3	Road	100	66.60	-36.17	-18.36	-30.97	0.34762E-05	0.18645E-02	0.23329E+01
Y2	Industrial	60000	70.94	-36.17	26.50	-7.42	0.95747E+01	0.30943E+01	0.17089E+02
I2	Industrial	25000	73.73	-36.17	24.31	-6.88	0.73734E+01	0.27154E+01	0.13237E+02
I4	Industrial	30000	75.23	-36.17	23.93	-6.52	0.33902E+01	0.18413E+01	0.82549E+01
H4	Dock	1000	72.26	-36.17	16.15	-0.17	0.94435E+02	0.97178E+01	0.10106E+02
H5	Dock	1000	72.88	-36.17	16.15	-0.52	0.67843E+01	0.26047E+01	0.29332E+01
H6	Dock	1000	73.53	-36.17	14.93	-4.56	0.21330E+01	0.14804E+01	0.41737E+01
H7	Dock	1000	74.25	-36.17	17.84	-2.17	0.23678E+02	0.48660E+01	0.28518E+01
H8	Bridge	100	76.42	-23.98	10.44	-1.63	0.20118E+01	0.71184E+01	0.20839E+01
H9	Bridge	100	76.72	-24.11	17.80	4.59	0.56407E+02	0.73104E+01	0.27353E+01
H10	Bridge	100	76.87	-15.88	19.77	8.22	0.23279E+03	0.15258E+02	0.23000E+01
H11	Bridge	100	77.10	-16.63	16.63	3.86	0.38550E+02	0.62089E+01	0.35484E+01
G1	Grass	10000	61.61	-36.17	-10.07	-25.72	0.99857E-05	0.31600E-02	0.11795E+01
M2	Ftbl Field	600	70.75	-36.17	19.17	-19.17	0.35657E-05	0.18883E-02	0.12903E+01
M3	Ftbl Stadium	600	70.75	-36.17	4.19	-10.50	0.37311E-01	0.19316E+00	0.21675E+01
H12	Arena	11000	70.75	-36.17	7.57	-15.36	0.31436E-01	0.17730E+00	0.60978E+01
H13	Parking Lot	7650	70.19	-36.17	19.24	-8.85	0.24563E+01	0.15672E+01	0.12032E+02
M4	Parking Lot	800	68.98	-36.17	-0.02	-27.13	0.13098E-02	0.36191E-01	0.29398E+01
M5	Parking Lot	800	69.06	-36.17	-0.29	-34.51	0.10814E-05	0.10399E-02	0.18684E+02
M6	Parking Lot	5000	69.14	-36.17	-0.29	-27.75	0.47690E-03	0.21838E-01	0.12997E+02
I5	Industrial	45000	63.43	-36.17	16.55	-13.45	0.18244E+00	0.90745E+01	0.34499E+01
H14	Bridge	100	75.73	-17.02	18.92	4.80	0.82346E+02	0.27710E-04	0.11416E+00
W4	Water	2450	73.52	-36.17	-29.80	-36.15	0.67686E-09	0.29191E-02	0.10603E+01
G2	Grass	2450	73.52	-36.17	-15.65	-25.60	0.85210E-05	0.22202E+01	0.12395E+01
G3	Grass	6400	75.12	-36.17	-12.11	-24.38	0.20446E-04	0.45217E-02	0.14263E+02
I6	Industrial	60000	78.51	-36.17	23.94	-8.08	0.49295E+01	0.22202E+01	0.14263E+02
H15	Bridge	50	78.79	-36.17	8.74	-5.83	0.85537E-01	0.29247E+00	0.11207E+01
W5	Water	50	78.92	-36.17	36.17	-36.17	0.20129E+01	0.14188E+01	0.78437E-04
H16	Water	3000	77.51	-36.17	26.55	-6.12	0.35951E-15	0.18961E-07	0.19155E+01
I7	Industrial	15000	77.22	-36.17	8.58	-24.68	0.21931E+02	0.46831E+01	0.19155E+01
F1	Forest	1000	81.40	-36.17	19.94	-2.17	0.33360E-02	0.67365E-02	0.18422E+01
H17	Terminal	500	81.75	-36.17	27.03	7.10	0.87704E+03	0.28615E-02	0.62181E+01
H18	Terminal	500	81.17	-36.17	27.03	7.10	0.87704E+03	0.28615E-02	0.50947E+01
H19	Plane	49	81.17	-36.17	9.03	-0.97	0.26667E-01	0.16310E+01	0.20403E+01
H20	Plane	49	81.84	-36.17	9.03	-0.97	0.26667E-01	0.16310E+01	0.20403E+01
Ru1	Runway	900	81.68	-36.17	7.08	-3.73	0.82626E-00	0.91119E+00	0.21503E+01
Ru2	Runway	900	81.49	-36.17	-36.17	-36.17	0.39315E-15	0.18961E-07	0.78427E-04
Ru3	Runway	1600	81.35	-36.17	-36.17	-36.17	0.39315E-15	0.18961E-07	0.78427E-04
M7	Parking Lot	1600	81.40	-36.17	15.47	-9.58	0.35951E-15	0.18961E-07	0.78427E-04
M8	Parking Lot	1600	81.49	-36.17	15.47	-9.58	0.17222E-01	0.13123E+01	0.11923E+02
H21	Warehouse	1600	81.49	-36.17	7.95	-13.98	0.85750E-01	0.25283E+00	0.73515E+01
H21	Warehouse	1600	80.04	-36.17	10.95	-13.98	0.85750E-01	0.25283E+00	0.73515E+01
M9	Ball Diamond	100	73.70	-36.17	10.95	-13.98	0.85750E-01	0.25283E+00	0.73515E+01
U1	Urban	5000	74.40	-36.17	-2.54	-17.10	0.47012E-02	0.68565E-01	0.35444E+01
W6	Water	15000	73.64	-36.17	-6.43	-22.34	0.26127E-03	0.16179E-01	0.27744E+01
W7	Water	15000	73.64	-36.17	-25.36	-36.11	0.48740E-08	0.69814E-04	0.28488E+00
W8	Water	62500	75.19	-36.17	-14.11	-33.96	0.78555E-07	0.28028E-02	0.11045E+01
W8	Water	62500	76.99	-36.17	-20.18	-36.02	0.31815E-07	0.17837E-03	0.71285E+00
H22	Barge	50	78.17	-36.17	9.57	-0.57	0.32532E+01	0.18037E+01	0.20581E+01
H22	Barge	400	78.74	-36.17	8.74	-3.78	0.97835E-00	0.98912E+00	0.23629E+01
H23	Barge	4000	78.74	-36.17	-11.59	-35.20	0.19550E-05	0.13620E-02	0.45112E+01
W9	Water	40000	79.19	-36.17	-11.71	-34.27	0.56422E-05	0.23763E-02	0.63531E+01
W10	Water	40000	80.19	-36.17	-8.86	-33.65	0.19513E-04	0.43027E-02	0.99813E+01
W11	Water	40000	81.13	-36.17	-5.05	-33.82	0.40770E-04	0.63851E-02	0.15400E+02



Report Documentation Page

1. Report No. NASA CR- 4280 DOT/FAA/DS-89/15		2. Government Accession No.		3. Recipient's Catalog No.	
4. Title and Subtitle Synthetic Aperture Radar Imagery of Airports and Surrounding Areas - Philadelphia Airport				5. Report Date March 1990	
				6. Performing Organization Code	
7. Author(s) Robert G. Onstott Denise J. Gineris				8. Performing Organization Report No.	
				10. Work Unit No. 505-67-41-57	
9. Performing Organization Name and Address Environmental Research Institute of Michigan (ERIM) 1975 Green Rd. Ann Arbor, MI 48105				11. Contract or Grant No. NAS1-18465	
				13. Type of Report and Period Covered Contractor Report 31 Aug. 87 - 30 Nov. 89	
12. Sponsoring Agency Name and Address National Aeronautics and Space Administration Langley Research Center Hampton, VA 23665-5225				14. Sponsoring Agency Code	
				15. Supplementary Notes Langley Technical Monitor: E. M. Bracalente	
16. Abstract This report is the second in a series of three which address the statistical description of ground clutter at an airport and in the surrounding area. These data are being utilized in a program to detect microbursts. Synthetic Aperture Radar (SAR) data were collected at the Philadelphia Airport. This report describes these data and the results of the clutter study. This 13 km x 10 km scene was imaged at 9.38 GHz and HH-polarization and contained airport grounds and facilities (6%), industrial (14%), residential (14%), fields (10%), forest (8%), and water (33%). Incidence angles ranged from 40° to 84°. Even at the smallest incidence angles, the distributed targets such as forest, fields, water, and residential rarely had mean scattering coefficients greater than -10 dB. Eighty-seven percent of the image had scattering coefficients less than -17.5 dB. About 1 percent of the scattering coefficients exceeded 0 dB, with about 0.1 percent above 10 dB. Sources which produced the largest cross sections were largely confined to the airport grounds and areas highly industrialized. The largest cross sections were produced by observing broadside large buildings surrounded by smooth surfaces.					
17. Key Words (Suggested by Author(s)) clutter, backscatter, SAR, microburst			18. Distribution Statement unclassified - unlimited subject category 03		
19. Security Classif. (of this report) unclassified		20. Security Classif. (of this page) unclassified		21. No. of pages 116	22. Price A06

